Capillary forces on femtosecond laser micromachined metallic surfaces

Jorge Lehr

Doctoral Thesis

Department of Chemical Engineering
McGill University
Montreal, Quebec

April 2015

Thesis submitted in partial fulfillment of the requirements for the degree of
Doctor of Philosophy

Acknowledgements

First and foremost, I would like to express my deepest gratitude towards my supervisor, Prof. Anne Kietzig, for her invaluable support throughout the course of my PhD program. Her emphasis on integrity and thoroughness will continue to inspire and influence my professional and personal development. I want to thank all current and former members of the Surface Engineering Laboratory and the Plasma Processing Laboratory (PPL) at McGill University, especially Tanvir Ahmmed, Fabrizio De Marchi, Luke Matus, Edwin Ling, Larissa Jorge, Nathan Hordy and Felipe Aristobal for their contributions to this work and numerous delightful discussions.

I want to thank Frank Caporuscio, Lou Cusmich, Jo-Ann Gadsby, Gerald Lepkyj, Ranjan Roy, Andrew Golsztajn, Melanie Gorman and Emily Musgrave, and all other technical and administrative staff of the Chemical Engineering Department, without whom I would not have been able to complete my work. I am also especially grateful towards Beatrice Lego and Mohini Ramkaran from the Center of Self-Assembly Chemical Structures (CSACS) for training me on the AFM and their support during my experiments. Special thanks also to Robert Letiecq who was always available to help us keep our laser alive.

Last but not least, I want to dedicate my most sincere appreciation for the love and support from my family and my beloved fiancée. Without them I would not have been able to maintain the motivation and energy to conduct this work throughout the past four years.

Abstract

In this PhD thesis, femtosecond laser micromachining was applied on titanium surfaces to produce homogeneous arrays of surface structures with the objective of studying their wetting behavior and the magnitude of capillary forces measured in a humid environment.

The relevant machining parameters to control the formation of uniform arrays of surface structures were identified, and two types of surface microstructures covered with nanoscale roughness were produced in air. The two types of structures were found to result from different formation regimes, since only for one type a uniform energy input on the target surface was required to obtain a homogeneous array.

Micromachining in pure oxygen, nitrogen and helium showed that the formation of these microstructures depends also on the environment: The chemical composition and optical properties of the surface and the cloud of ablated nanoparticles was identified to be responsible for the decrease of the effective energy input in a nitrogen environment. It was found that titanium-nitride (TiN) was formed on the surface during machining in nitrogen, while the surface chemistry, and hence the effective energy, were practically unchanged for oxygen and helium environments. Even though, it was possible to produce the two previously found types of microstructures, only oxygen was identified to allow the formation of highly uniform arrays.

Wettability and capillary forces were measured with colloidal atomic force microscopy on the previously produced surfaces as well as on surfaces that carry only roughness on the nanoscale. Microstructured surfaces and these containing TiN were found to be hydrophobic, however exhibiting a high magnitude of capillary forces. The forces were limited on samples with only nanoscale roughness, which were machined in oxygen. At the same time these samples were hydrophobic and the least sensitive to an increase of the relative humidity in the environment.

Abrégé

Dans cette thèse doctorale, le micro-usinage au laser femtoseconde de surfaces de titane a été employé afin de produire des réseaux de structures homogènes. Ces surfaces modifiées ont été étudiées pour leur mouillabilité et l'intensité des forces capillaires mesurées dans un environnement humide.

Les paramètres d'usinage permettant le contrôle de la formation de ces réseaux de surface uniformes ont été identifiés. En particulier, deux types de surfaces microstructurées avec une rugosité à l'échelle nanométrique ont été produites dans l'air. Deux régimes de formation différents sont à l'origine de ces structures étant donné qu'un seul des deux types de surface requiert une quantité uniforme d'énergie incidente sur la cible pour obtenir un réseau de structures homogènes.

Le micro-usinage dans une atmosphère d'oxygène, d'azote ou d'hélium a démontré que la formation de ces structures dépend aussi de l'environnement. La composition chimique et les propriétés optiques de la surface ainsi que le nuage de nanoparticules ablaties sont tous des facteurs responsables de la diminution de l'énergie incidente sur la surface observée dans une atmosphère d'azote. Il a été démontré que du nitrure de titane (TiN) se forme sur la surface pendant l'usinage dans l'azote, alors que la chimie de surface, et par conséquent l'énergie incidente, n'était pas affectée dans un environnement d'oxygène ou d'hélium. De plus, même s'il a été possible de produire les deux microstructures mentionnées ci-haut, uniquement l'atmosphère d'oxygène a permis la formation de réseaux très homogènes.

La mouillabilité et les forces capillaires ont été mesurées par sonde colloïdale au microscope de force atomique sur les surfaces décrites ci-haut ainsi que sur des surfaces ayant uniquement une rugosité nanométrique. Il a été démontré que les surfaces microstructurées et celles recouvertes de

TiN sont hydrophobes, mais présentent des forces capillaires élevées. Les forces mesurées étaient faibles sur les surfaces à rugosité nanométrique, produites dans une atmosphère d'oxygène. Ces échantillons étaient aussi hydrophobes et les moins sensibles à une hausse d'humidité relative dans leur environnement.

Contribution of authors

This thesis is manuscript-based and contains three manuscripts where I, Jorge Lehr, have carried out the majority of the work (Chapter 3, Chapter 4 and Chapter 5).

In all cases, I conducted all the micromachining experiments and statistical analysis. I did all surface characterization measurements (SEM, AFM, contact angle goniometry), except the XPS measurements conducted by Fabrizio Di Marchi at the INRS, Centre Énergie, Materiaux, Telécommunications, 1650 Lionel Boulet Boulevard, J3X 1S2, Varennes, QC, Canada.

In chapter 4 Luke Matus participated in the laser micromachining experiments. Furthermore, he developed the method for laser micromachining in water I applied in chapter 5. The high resolution SEM and EDX measurements in chapter 5 were carried out by Nicolas Brodusch at Prof. Gauvin's laboratory at the Material and Mining Engineering Department at McGill University. The Matlab code that I used throughout my work to calculate accumulated intensities was developed by Edwin Jee Yang Ling.

I wrote all the manuscripts. These were then edited and revised by my supervisor Prof. A.-M. Kietzig before submitting to peer-reviewed journals.

Table of contents

1. Table of Contents

List of Figures

List of Tables

Glossary

Laser material interaction and micromachining

C_e	electron volumetric heat capacities	[J/(m^3 K)]
C_l	lattice volumetric heat capacities	[J/(m^3 K)]
D	topological dimensions	[no unit]
E	energy	[J]
F	laser fluence	[J/cm^2]
f_p	pulse repetition rate or frequency	[1/s]
I_0	peak intensity	[J/(s cm^2)]
I_{abl}	single pulse ablation threshold intensity	[J/(s cm^2)]
$I_{abl}(N)$	multi (N) pulse ablation threshold intensity	[J/(s cm^2)]
I_{eff}	effective laser intensity	[J/(s cm^2)]
I_{pulse}	single pulse intensity	[J/(s cm^2)]
I_{theo}	theoretical laser intensity	[J/(s cm^2)]
k_e	electron thermal conductivity constant	[W/(m K)]
k_G	electron-phonon coupling constant	[W/(m^3 K)]
n_r	refractive index	[no unit]
P	average power	[J/s]
PPS	laser pulses per spot	[no unit]
S_{inc}	laser energy incubation coefficient	[no unit]
T_e	electron temperature	[K]
T_l	lattice temperature	[K]
v_0	scanning velocity	[mm/s]
φ_{pulse}	pulse overlap	[%]
φ_{line}	line overlap	[%]
ω_{theo}	theoretical beam diameter	[µm]
ω_{eff}	effective beam diameter	[µm]
ω_{model}	beam diameter from Liu's model	[µm]

Wettability and surface forces

A	area	[m^2]
c	wettability factor	[no unit]
F_0	surface force at 0 % RH	[N]
F_{cap}	capillary forces	[N]
f_0	resonance frequency of AFM probe	[1/s]
G	Gibbs free energy	[J]
g	gravitational acceleration	[m/s^2]
k_b	Boltzmann constant	[(m^2 kg)/(s^2 K)]
k_s	spring constant	[N/m]
l	distance between interacting surfaces	[m]
l'	height of meniscus on the asperity	[m]
l_{asp}	height of a surface asperity	[m]
l_{cap}	relevant length scale for capillary forces	[m]
l_{acc}	accumulated l_{cap}	[%]
l_{va}	distance between the molecules in the vapor phase	[m]
n_M	molar number	[mol]
Δp	Laplace pressure	[N/m^2]
p_v	water vapor pressure	[N/m^2]
$p_s(T)$	saturation pressure	[N/m^2]
R	gas constant	[J/K]
r_{a_1}, r_{a_2}	radius of surface asperity/feature or AFM probe	[m]
r_f	roughness factor	[no unit]
r_m	radius of the circle of the contact line on the asperity	[m]
r_{RMS}	RMS roughness	[m]
r_{curv}	Kelvin radii of meniscus curvature	[m]
r_1	diameter of meniscus (capillary bridge)	[m]
r_2	radius normal to the diameter of meniscus	[m]
S_x	humidity sensitivity	[no unit]

T	temperature	[K]
V	volume	[m^3]
V_M	molar volume	[m^3/mol]
W	work	[J]
Δz	deflection of AFM cantilever	[m]
α_{tip}	angle at the semi-aperture of an AFM tip	[°]
β	filling angle	[°]
γ	surface tension	[N/m]
γ_{LA}	surface tension at liquid-air interface	[N/m]
γ_{SL}	surface tension at solid-liquid interface	[N/m]
γ_{SA}	surface tension at solid-air interface	[N/m]
ε_i	fraction of the surface area of surface i	[no unit]
θ_E	equilibrium contact angle	[°]
θ_W	Wenzel contact angle	[°]
θ_{CB}	Cassie Baxter contact angle	[°]
λ_K	Kelvin-length	[m]
ρ	density	[kg/m^3]
ψ	geometric force factor	[no unit]

Chapter 1

1. Introduction

Earth's surface is covered with water of oceans, ice and rivers. The force of water shapes shores, mountains and valleys, and has been used as a power source by humanity for centuries. Less known is the role that water plays on the micro- and nanoscale, while being present on every surface at ambient conditions (Israelachvili 2010). Water is able to act as an adhesive, or as a lubricant when forming thin films, droplets or molecular double layers. The interaction between a liquid and a surface is known as wetting. Surfaces that wet easily by water are called *hydrophilic*, while water repellent surfaces are called *hydrophobic*. It depends on the very application of a surface, whether hydrophilic or hydrophobic wetting behavior is desired. Many surfaces, like these of metals, paper, wood and glass, are intrinsically hydrophilic; consequently researchers repeatedly aim for achieving water repellence on these surfaces to expand their use in engineering applications (Bhushan and Jung 2010). Scientific studies on wettability (Bormashenko 2010, Hancock, Sekeroglu et al. 2012) and laser micromachining (Baojia, Ming et al. 2008, Yong, Chen et al. 2013, Kietzig, Lehr et al. 2014) are often carried out in the context of *biomimetics*, which is an engineering approach where models, systems, and elements of Nature are imitated for the purpose of solving human problems (Bhushan 2009).

1.1 Surfaces obtained from femtosecond laser micromachining

The unique property of femtosecond laser pulses is their extremely short duration, which is shorter than most of the relaxation time scales of an ion-lattice and its electrons (Du, Liu et al. 1994, Liu, Du et al. 1997). Consequently, heat related phenomena like melt are limited and precise geometric features on the microscale with tolerances of a few hundred nanometers can be machined with femtosecond lasers on different materials like metals (Nolte, Momma et al. 1997), polymers (Mendonca, Cerami et al. 2008) and ceramics (Liang, Wang et al. 2008). Thereby, the bulk material's properties like its mechanical strength or its thermal conductivity can be combined with the surface properties obtained from the laser machining process. Laser micromachining with a longer wavelength cannot compete with femtosecond laser micromachining regarding its geometric precision. However, the production of structured surfaces with femtosecond lasers does compete with methods like ion-etching (Wu, Cho et al. 2010), photo-lithography (Park, Jeong et al. 2009) and other mechanical or chemical surface modification techniques, which have been shown to deliver well defined and highly ordered arrays of micro- and nanostructures.

The advantages of femtosecond laser micromachining and laser-based systems in general are their low operational costs, the absence of toxic waste after processing, and the relatively easy scale up from laboratory to industrial scale (Booth 2004). Furthermore, laser micromachining can be carried out on targets of different geometries (2D and 3D) by combining the laser source with scanners and robotics. Beside these advantages, metallic surfaces obtained by femtosecond laser micromachining are the focus of this work because of the possibility of changing their surface topology and chemistry in a single step to obtain different wetting behavior. Previously, metallic surfaces could only be rendered hydrophobic by applying coating and painting techniques. Femtosecond laser micromachining produces a dual scale roughness with subsequent change of the wetting behavior (Kietzig, Hatzikiriakos et al. 2009, Kietzig, Mirvakili et al. 2012): The micromachined surfaces, initially hydrophilic, became hydrophobic after several days when they were exposed to air or CO_2 without any further treatment. This phenomenon is known as *contact* *angle evolution.* Furthermore, it has been observed that the exposure to water or humid air hinders contact angle evolution on femtosecond laser micromachined surfaces (Kietzig, Lehr et al. 2014).

Hence, femtosecond laser irradiated surfaces are possible candidates for engineering applications where a certain level of wettability is required like in the case of water based coatings (Schmidt, Coburn et al. 1994), water absorbing materials (Vogt, Soles et al. 2005), drag-reduction in micro-fluidic devices (Daniello, Waterhouse et al. 2009) or fog harvesting (Andrews, Eccles et al. 2011). However, they are also ideal objects to study wetting phenomena, and in particular capillary forces.

1.2 Wetting and capillary forces

Scientific research on wetting has a long history (Langmuir 1918, Wenzel 1936, Cassie and Baxter 1944, Cassie 1948). Hence, the main concepts (chapter 2.2) of wettings states, the influence of the surface topology and environmental conditions are well understood (de Gennes 1985, Shanahan 1987, Marmur 1992, Shanahan 1995, de Gennes, Brochard-Wyard et al. 2003, Extrand 2003, Tadmor 2004, McHale 2007, Whyman, Bormashenko et al. 2008, Bormashenko 2009, Marmur 2009, Mittal and Hummer 2010, Bormashenko 2011, Tadmor 2011). Four different scientific disciplines have to be considered in the context of wetting (de Gennes 1985): physical chemistry to describe wettability, statistical physics to explain the interface between the three phases at the contact-line, the physics of surface forces, and fluid dynamics of capillary and droplet formation. Of these, surface forces and capillary formation are classic phenomena in the context of surface science. However, they are less accessible than wettability, since in contrast to macroscopic contact angle measurements, surface forces require more sophisticated measuring devices. The arrival of atomic force microscopy (AFM) in particular has allowed more fundamental research in this field (Butt 1991). Weak surface forces like van-der-Waals forces (vdW) as well as the force originating from single capillary bridges are measurable by AFM at nanoscale resolution (Gould, Drake et al. 1990, Hoh, Cleveland et al. 1992). Compared to other force measurement techniques like these that apply a Surface Force Apparatus (Charlaix and Crassous 2005), AFM does not require any particular treatment of the sample. Hence, AFM can be used on almost any solid or soft sample in gaseous or liquid environments. AFM has been used extensively in studying ways to improve the performance of applications like micro-electrical-mechanical devices (MEMS) (Tien, Jeong et al. 1996, Jung and Bhushan 2008, Crassous, Ciccotti et al. 2011, Yamazaki, Yakushiji et al. 2012) or to investigate friction phenomena (Meyer, Luthi et al. 1996, Szoszkiewicz, Bhushan et al. 2005, Lee and Bhushan 2011).

1.3 Objectives

The primary goal of this doctoral thesis is to expand the knowledge about wetting and capillary forces on micromachined surfaces. Therefore, uniform arrays of surface structures are produced, and their topological and chemical properties are linked to wettability and capillary forces. The following specific objectives were derived for this dissertation:

1. Identification of relevant parameters to produce uniform (homogeneous) micro- and nanostructures on metallic (titanium) surfaces
    a. To consolidate the parameters and to associate these with the machining output
    b. To simulate and visualize the accumulated energy input on the target surface
    c. To investigate the mechanism for microstructure formation
2. Evaluation of the role of the gas environment during femtosecond laser micromachining
    a. To explore the relationship between gas environment and energy input on the target surface
    b. To determine the alteration of the surface topology and surface chemistry
    c. To compensate for the altered energy input to obtain uniform arrays of surface structures in different gas environment
3. Examination and quantification of capillary forces on femtosecond laser micromachined metallic surfaces
    a. Measuring capillary forces on different types of laser micromachined sample
    b. To quantify the contribution of surface topology and surface chemistry
    c. To link capillary forces to surface wettability

1.4 Organisation of this thesis

Including this introduction, this manuscript-based thesis has a total of 6 chapters. Chapter 2 is a detailed literature review with emphasis on general laser-material interactions, wetting concepts and capillary forces. Chapter 3 to 5 are the manuscripts that present the results from the experimental work in this project:

- Chapter 3: *Production of homogeneous microstructures by femtosecond laser micromachining*
- Chapter 4: *The influence of the gas environment on morphology and chemical composition of surfaces micromachined with a femtosecond laser*
- Chapter 5: *Dependence of capillary forces on relative humidity and the surface properties of femtosecond laser micromachined titanium*

The three manuscripts are written as stand-alone publications, however they premise on the respective previous paper, beginning with the second manuscript. Prefaces introduce each of the manuscripts and put it in context with the other chapters. Chapter 6 contains general conclusions of this thesis, followed by a summary of contributions to the state of the art knowledge in the field and recommendations for future work. The experimental sections are included in the manuscripts. The supporting information for each manuscript can be found in the appendices. The figures, tables and variables are listed together at the beginning of the document. Figures, tables and equations are numbered in a way that indicates their location within a particular chapter. The references for all chapters are listed at the end of this document.

Chapter 2

2. Literature review

2.1 Laser-material interactions

Laser-material interactions depend in general not on the total amount of energy that a surface is exposed to, but rather on the energy per pulse as well as the time scale and the spatial distribution of the exposure (Barthélemy, Margot et al. 2005, Le Harzic, Breitling et al. 2005, Cheng, Perrie et al. 2009). In the case of a pulsed laser, the pulse duration and the spacing between the pulses have to be considered with the time scales of the material response, such as the electron diffusion inside the material or the thermal conductivity, to predict the outcome of the machining process (Gamaly 2011). The spatial control is achieved by adjusting the spot diameter at focus (Gang and Yiliu 2012) and the overlap of the pulses in the directions of machining (Vogel and Backlund 1965, Chengwu, Binshi et al. 2010, Yao, Xu et al. 2010, Guoqiang, Jiawen et al. 2013). Additionally, it has to be understood that under most experimental conditions the theoretical energy exposure (Chapter 2.1.2) of the surface is different from the effective exposure (Chapter 2.1.4) due to interactions of the beam with the environment (Hermann, Boulmer-Leborgne et al. 1993, Chiron, Lamouroux et al. 1999, Sun and Longtin 2001, Zhigilei 2003, Scuderi, Albert et al. 2005, Sheehy, Winston et al. 2005, Wen, Mao et al. 2007, Wen, Mao et al. 2007). The material response, usually quantified by threshold energies, depends on the temporal and spatial distribution and the effective energy reaching the surface (Jee, Becker et al. 1988, Tan, Dalili et al. 2009). Unfortunately, the communication within the scientific community is sometimes confusing due to the fact that reported threshold values cannot be compared unless ultimately all other parameters are reported.

In the following subchapters, the state of the art in femtosecond laser micromachining will be presented.

2.1.1 Laser and machining parameters

The most important parameter for laser micromachining with pulsed lasers is the energy per pulse [J] to which the target surface is exposed, since the extent of surface modification like ablation and growth of microstructures correlate directly with it (Cheng, Perrie et al. 2009). Equally important is the pulse duration [s], which is the dwell time of the laser energy on the target surface. Many studies have shown that precise microstructures can only be produced with pulses of the order of picoseconds or less (Craig 1998, Zhao, Huttner et al. 1999, Le Harzic, Huot et al. 2002, Luo, Li et al. 2002, Chien and Gupta 2005, Geng, Fu et al. 2007, Batani 2010, Delaigue, Honninger et al. 2012, Lopez, Torres et al. 2013). Pulse energy and pulse duration are coupled: Very high peak intensities of the order of several GW/m^2 or TW/m^2 can only be achieved with ultra-short pulses at pulse energies on the order of 1 to 10 uJ (Liu, Du et al. 1997). The energy input has to be quantified with dimensions that include the time of exposure and/or a reference area. These dimensions are: fluence (F) [J/cm^2], power (P) [J/s] and intensity (I) [J/(s cm^2)]. Researchers throughout the field use mostly fluence and intensity to quantify and report the energy input during experiments. However, the units of these three dimensions indicate that they express the energy with either temporal and/or spatial reference so that they actually serve different purposes and have to be chosen carefully, while reporting experimental results. Ultimately, the input energy depends also on the wavelength, which is a hardware parameter and usually fixed for a particular laser source (typically around 800 nm for Ti:Sapphire femtosecond lasers).

The other temporal parameter besides pulse duration is the repetition rate f_p. Often, femtosecond lasers are operated at 1 kHz to 10 kHz (Venkatakrishnan, Stanley et al. 2003, Perrie, Gill et al.

2004, Le Harzic, Breitling et al. 2005, Tsukamoto, Asuka et al. 2006, Vujicic, Skenderovic et al. 2006, Nayak, Gupta et al. 2008, Chen, Fu et al. 2009, Cheng, Perrie et al. 2009, Romer, Huis in't Veld et al. 2009, Kara and Kizil 2012). At larger rates up to several MHz, (Gattass, Cerami et al. 2006, Groenendijk and Meijer 2006) the temporal spacing between the pulses becomes so small that the advantages of femtosecond lasers in micromachining vanish: The relaxation time of the material and the decay time of the plasma are then longer than the temporal spacing between the pulses so that the ablation plasma interacts with the laser beam. Experiments at high repetition rates (> 10 kHz) indicate that these effects reduce the energy reaching the surface, which results in smaller surface features (Tan, Dalili et al. 2009). Researchers operating with pulsed lasers tend to use the repetition rate to calculate the reference time for the energy exposure of the surface (Paschotta 2008, Eichstädt, Römer et al. 2013): In the case of a 1 kHz system, for instance, the intensity exposure is calculated for a time interval of 0.001 s.

A reference area is required for all spatial parameters to be quantified. This area is calculated from the beam diameter at the point of incidence of the laser beam on the target surface. The *theoretical* beam diameter (ω_{theo}) is defined at focus, where the diameter of the beam has its minimum, which is usually called the *beam waist*. When a laser is used to modify surfaces, the effective area is of interest. However, this effective area that a single beam covers on the target surface is always smaller than the theoretical beam diameter. Both types can serve as reference areas for energy per area and overlap calculations (see next paragraph). The resulting implications for the machining of microstructures are extensively discussed in chapter 3 of this thesis. However, the effective beam diameter (ω_{eff}) does not contain all information about the spatial distribution of the laser energy since it does not express the energy distribution across the beam.

The spatial distribution of the laser energy across the beam diameter is of particular relevance for surface micromachining with lasers. Typically, the energy distribution is *Gaussian* (Liu, Du et al. 1997, Nolte, Momma et al. 1997). It is the “natural” case and does not require any particular treatment along the beam path. Other distributions like *top-hat* (flat energy profile) (Tan and Venkatakrishnan 2006, Huot, Sanner et al. 2007) and *Bessel* (one additional local energy maximum away from the center) (Arlt and Dholakia 2000) are only obtained after the laser beam is directed through special optics. A Gaussian beam’s disadvantage for micromachining is the inhomogeneous energy distribution across the beam and by definition, its infinite width. The latter issue has been solved by the convention that the radius is defined as the distance from the center (peak energy) where the energy is lower than 0.135 ($1/e^2$) times the peak energy (ISO 2005). There are several methods to determine the $1/e^2$ value (Vogel and Backlund 1965, Liu 1982, Marshall 2010, González-Cardel, Arguijo et al. 2013), which have to be reported in a publication to allow the reproduction of results.

Laser micromachining with a Gaussian shaped beam demands a deeper understanding of the way two or more pulses overlap. Eq. (2.1) expresses the overlap of the pulses of a pulse-train of a laser beam. The number of pulses per spot (PPS) is calculated from the repetition rate f_p and the scanning velocity v_0. The overlap φ_{pulse} is usually expressed in %.

$$\varphi_{pulse} = \left(1 - \frac{v_0}{f_p \omega_{theo}}\right) \times 100 \tag{2.1}$$

In a typical experimental setup, the pulse-overlap φ_{pulse} and the resulting PPS depend on the movement (velocity) of the translation stage or the scanning beam in *x*-direction. In contrast, the line-overlap φ_{line} depends on the velocity in *y*-direction and the length of a scanned line when two or more lines are raster scanned. Thus, the total number of PPS depends on φ_{pulse} and φ_{line}. The question then arises as to whether the material of the target surface that is affected by laser pulses several times at different time scales returns to the initial state or keeps a pre-modified state. Hence, the selection of the adequate overlap and PPS values requires also understanding how much a delay time between the pulses alters the material response.

2.1.2 Material response mechanism & thresholds

Femtosecond laser irradiation causes non-equilibrium phenomena while interacting with materials. Ablation occurs when an atom is removed from the ion-lattice of a surface after it is exposed to an energy level greater than the binding energy, and consequently plasma is formed. The electrons in the ion-lattice are excited by the monochromatic light of the beam by multi-photon absorption. The minimum energy required for ablation depends on the photon absorption coefficient of the respective material (Gamaly 2011). The absorption of the photons causes superheating of the lattice while the electron gas diffuses within the material of the target. Subsequently, the excited electrons equilibrate with the lattice via electron-phonon interactions. The time scale of this process is of the order of 1-10 ps (Lorazo, Lewis et al. 2006), which is three orders of magnitude longer than a 100 fs laser pulse. Consequently, the electron T_e and lattice T_l temperatures have different temporal and spatial distributions. Thus, the target substrate exists in a highly non-equilibrium state, which allows three possible ablation regimes (Gamaly 2011):

- Non-equilibrium, non-thermal (Coulomb explosion with electrostatic ablation during pulse duration (Stoian, Ashkenasi et al. 2000))
- Non-equilibrium, thermal (Phase explosion and separation after the end of the pulse (Kelly and Miotello 1996, Cheng and Xu 2005))

- Thermal equilibrium ablation (Melting after the end of the pulse (Ivanov and Zhigilei 2003))

The thermal non-equilibrium phenomena are expressed by the two-temperature model (TTM) with two non-linear partial differential equations (Eq. (2.2) and Eq. (2.3)). The TTM explains why femtosecond laser irradiation causes ablation through direct evaporation (Anisimov, Kapeliovich et al. 1974).

$$C_e(T_e)\frac{\partial T_e}{\partial t} = \nabla \cdot (k_e(T_e)\nabla T_e) - k_G(T_e - T_l) + Q(\vec{r}, t) \tag{2.2}$$

$$C_l(T_l)\frac{\partial T_l}{\partial t} = k_G(T_e - T_l) \tag{2.3}$$

C_e and C_l are the electron and lattice volumetric heat capacities [J/(m^{3}K)], $Q(\vec{r},\ t)$ is the volumetric source term [W m^{-3}], k_e is the electron thermal conductivity [W/(m K)] and k_G is the electron-phonon coupling constant [W/(m^{3}K)]. Eq. (2.2) and Eq. (2.3) illustrate that the time required for electron-phonon equilibration is related to the extent of k_G so that electron-phonon coupling determines the energy transfer between electrons and the solid lattice. However, the superheated electrons disperse their energy not only by electron-phonon interaction, but also by electron diffusion through the bulk material (Wellershoff, Hohlfeld et al. 1999). The electron diffusion depth is inversely proportional to k_G (Corkum, Brunel et al. 1988): The electron diffusion depth is smaller since the energy transport to the lattice happens faster at higher k_G.

The TTM also explains why a heat affected zone (HAZ) is hardly observed when femtosecond laser irradiation interacts with metallic surfaces (Sherman, Brunel et al. 1989, Luft, Franz et al. 1996). A limited HAZ has been explained with the smaller magnitude of the electron specific heat compared to the lattice heat, which is driven by the energy deposition into the electron bath on fs time scale, while heat transfer to the lattice takes place on the ns time scale (Anisimov, Kapeliovich et al. 1974). Since electron-phonon coupling is cooling the electron bath, the driving force for diffusion of the heated electrons into the lattice is reduced, resulting in the considerably small HAZ in metals of only a few hundred nanometers (Le Harzic, Huot et al. 2002).

Even though the dependence of micromachining efficiency on k_G and k_e can be explained with the TTM and the electron diffusion model, Ahmmed and Ling have pointed out that there are several aspects of micromachining that are not considered since the models explain only the energy deposition mechanism (Ahmmed, Ling et al. 2015). Other laser-material interaction effects such as these resulting from the expansion of the plasma plume with the resulting shock wave generation, changes of the optical property as well as debris ejection and shielding are not explained (see chapter 2.1.3).

The shortcomings of the TTM and the electron diffusion model become even clearer considering that they are unable to predict ω_{eff}. Even though k_G and k_e are material properties, they do not explain the magnitude of the minimum (threshold) energy input from a laser beam which is required to cause a visible response (ω_{eff}) of the material. This response can be quantified by the ablation threshold intensity I_{abl} (Ngoi, Venkatakrishnan et al. 2001, Mannion, Magee et al. 2003, Nedialkov, Atanasov et al. 2007, Demir 2013). Typically, I_{abl} on metals in air is above 0.1 GW/m^2 (Du, Liu et al. 1994, Perry, Stuart et al. 1999). In contrast to the common perception, I_{abl} is not only dependent on material properties (like k_G and k_e) (Mannion, Magee et al. 2003), but also on experimental parameters like the target substrate's temperature (Yahng, Nam et al. 2009), the pressure of the machining environment (Gamaly, Rode et al. 2001) and the number of pulses per spot (PPS) (Jee, Becker et al. 1988, Venkatakrishnan, Stanley et al. 2003). The influence of the PPS on the ablation threshold is of particular relevance when a pulsed laser with high repetition rate f_p is used. It has been shown that I_{abl} decreases with increasing number of pulses (Jee, Becker et al. 1988). The phenomenon is explained with an *accumulation effect*, where the energy of every single pulse is accumulated until visible ablation on the surface occurs: Every laser pulse causes plastic deformations and the accumulation of heat inside the surface material before any material is ablated (Güdde, Hohlfeld et al. 1998, Mannion, Magee et al. 2004). The relative reduction of I_{abl} is the smallest at low pulse numbers and plateaus at higher levels of several hundred pulses (Ashkenasi, Lorenz et al. 1999). Ablation thresholds reported in literature usually refer to single-pulse ablation. However, Jee *et al.* derived Eq. (2.4) that allows to calculate the multi-pulse threshold $I_{abl}(N)$ from the incubation coefficient S_{inc} (Jee, Becker et al. 1988).

$$I_{abl}(N) = I_{abl}(1)N^{S_{inc}-1} \tag{2.4}$$

The experimentally determined coefficient S_{inc} quantifies incubation of laser energy from each pulse in the target material, while all other experimental conditions, like the pressure in the surrounding gas environment, are considered to be constant in this context.

2.1.3 Structure production on metallic surfaces

Femtosecond laser micromachining of highly ordered arrays of microstructures has been carried out by many researchers on metallic surfaces before (Vorobyev and Guo 2007, Vorobyev and Guo 2007, Baojia, Ming et al. 2008, Nayak, Gupta et al. 2008, Oliveira, Ausset et al. 2009, Yang, Yang et al. 2009). There are two technical solutions for machining of surfaces: raster-scanning with a *x*-*y*-translation stage or with a galvo-scanner (Jiwhan, Jeong et al. 2010). In the first case, the sample is moved in *x*-*y*-direction in front of a static laser beam. In the second case, the sample is static and the beam is scanning, driven by a system of moving mirrors. Raster scanning with a translation stage is more common and has been used throughout this study. Galvo-scanners have the advantage that machining of large areas is possible at a relatively short time. High lateral velocities of up to 2000 mm/s can be achieved (Cheng, Perrie et al. 2009, Romer, Huis in't Veld et al. 2009), while *x*-*y*-translation stages a limited to 5 to 10 mm/s (Perry, Stuart et al. 1999, Nayak, Gupta et al. 2008). However, translation stages allow more precise machining.

Laser patterned surface structures can be obtained by irradiating (Vorobyev and Guo 2007, Nayak, Gupta et al. 2008, Oliveira, Ausset et al. 2009) the target surface or by inscribing the structures into the surface (Baojia, Ming et al. 2008, Vorobyev and Guo 2008). In this thesis, laser induced periodic surface (nano-) structures, so called LIPSS or *ripple* structures, (Figure 2.1a) (Guosheng, Fauchet et al. 1982, Bonse, Baudach et al. 2002, Groenendijk and Meijer 2006, Tan and Venkatakrishnan 2006, Eichstädt, Römer et al. 2013) and columnar (Figure 2.1b) microstructures (Ahmmed, Grambow et al. 2014) have been used. In the case of femtosecond laser micromachining, these columnar structures are usually decorated with LIPSS (Vorobyev and Guo 2008), which assemble of parallel alternating peaks and valleys.

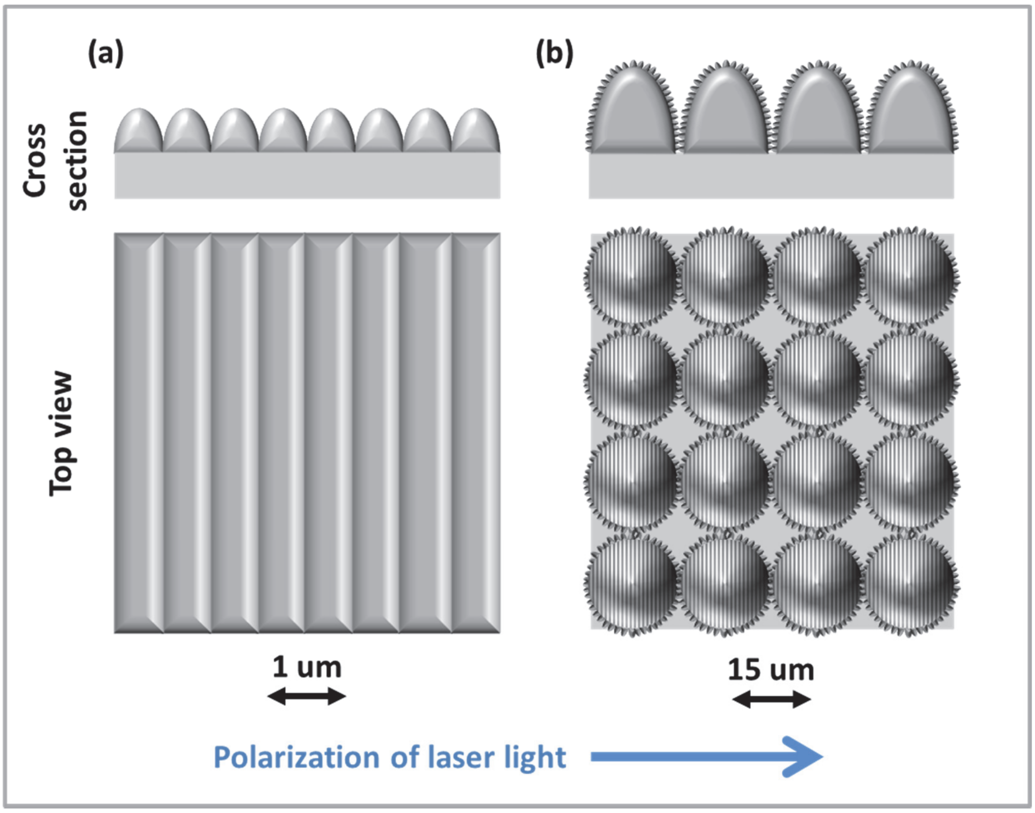

Figure 2.1: Schematic of LIPSS (a) and columnar structures covered with LIPSS (b).

Two types of LIPSS originate from femtosecond laser irradiation: a low-spatial-frequency LSFL type with a periodicity close to the laser wavelength and a high-spatial-frequency HSFL type that has a periodicity much smaller than the laser wavelength (Ahmmed, Grambow et al. 2014). LSFLs are perpendicular to the polarization of the incident laser beam and HSFLs can be parallel or perpendicular to the beam polarization. LSFLs originate from interference between the incident laser beam and a scattered optical wave at the surface causing an altered spatial energy distribution. The periodicity of LSFLs is close to the wavelength of the laser beam. The refractive index (n_r) of the surface material and the incident angle of the laser beam are the relevant variables (Guosheng, Fauchet et al. 1982, Sipe, Young et al. 1983, Young, Preston et al. 1983). HSFLs display a periodicity smaller than the wavelength and are less common than LSFLs on metals (Weck, Crawford et al. 2007). Researcher have attributed HSFLs to second harmonic generation

(Borowiec and Haugen 2003) or the excitation of surface plasmon polaritons (Martsinovskii, Shandybina et al. 2008).

Every type of surface structure occurs in a specific range of experimental settings (Tsukamoto, Asuka et al. 2006). LIPSS occur at relatively low input energy levels closely above the threshold for the first visible modification of the target surface. Hence, LIPSS are relatively easy to be produced and are the most accessible uniform periodic type of micromachinable type of surface structure. Columnar structures require higher energy input than LIPSS to be produced. However, at intermediate energy levels and increasing number of PPS, LIPSS serve as so called precursor sites that promote the formation of columnar features (Zuhlke, Anderson et al. 2013, Demir, Furlan et al. 2014).

Columnar structures grow either above the original surface or are formed below the surface by removing material. Below-surface growth dominates on metallic substrates at low pulse intensities I_{pulse} due to ablation (Zuhlke, Anderson et al. 2013). Firstly, single columnar structures grow from small spherical microdots. With increasing number of pulses, the columns begin to merge and an array is formed (Tsukamoto, Asuka et al. 2006). At higher intensities, columnar features grow above the initial surface level driven by a combination of hydrodynamic and particle redeposition processes, which are different on pure metals and on alloys (Zuhlke, Anderson et al. 2013). The key challenge of microscale columnar feature production is the maximization of the uniformity (homogeneity) of the feature arrays to obtain surfaces with uniform macroscopic and microscopic properties like wettability. Even though this topic has been investigated intensively, there is still no complete single model that incorporates all relevant micromachining parameters. These are in particular the pulse overlap with the resulting spatial energy distribution on the target surface and the number of PPS. The influence of the machining environment on the formation process of

LIPSS and columnar structures as well as on the degree of homogeneity has yet to be fully understood (see chapter 2.1.4).

2.1.4 Influence of the machining environment

Laser micromachining is either conducted in air (Cheng, Perrie et al. 2009, Hayden 2010, Kara and Kizil 2012) or in a specific gas atmosphere (Tan and Venkatakrishnan 2006, Vujicic, Skenderovic et al. 2006); in the latter case with the purpose of limiting undesired chemical reactions on the target surface during the micromachining process (Demir, Previtali et al. 2013). It has been observed that the ablation rate and the ablation threshold were altered in different gas environments (Sun and Longtin 2001, Gamaly 2011), which is explained by the way a laser beam interacts with its environment. In the case that the pulse intensity I_{pulse} is above the ionization threshold of the surrounding gas, the gas is ionized and plasma is formed (Guo, Li et al. 1998). A so called plasma plume is also formed when the first laser pulse above the ablation threshold I_{abl} of the target material hits the surface (Grojo, Hermann et al. 2005, König, Nolte et al. 2005). Consequently, part of the laser energy is absorbed by the electrons in the plasma (Gamaly 2011). However, in the case of femtosecond pulses, the interaction between the laser beam and the plasma plume is limited (Le Drogoff, Vidal et al. 2005): the plasma is only formed after a few nanoseconds so that the laser pulse has vanished already (König, Nolte et al. 2005). Depending on the repetition rate (f_p) of a pulse-train, the plasma density decreases far enough to allow neglecting interactions with the subsequent pulse (Barthélemy, Margot et al. 2005). Even though femtosecond laser pulses are too short to interact with the plasma directly, the state of the ablation plasma plume still depends on the beam intensity. At higher intensity, more material is ablated and the density and the size of the plasma plume increase. The pressure of the surrounding atmosphere then is the size limiting parameter (Drouet and Meunier 1985, Barthelemy, Margot et al. 2005).

It has been observed that the precision of micromachining and the quality in terms of homogeneity of the surface depends on the choice of the background gas: Noble gases like argon and helium were suggested to use due to their high ionisation threshold (Perrie, Gill et al. 2004, Nayak, Gupta et al. 2008).

2.2 Wetting concepts

Wetting can be defined as the change of the free surface energy by work W performed at a surface area A (Adam 1930). In Eq. (2.5) the change of work dW that is necessary to increase the surface area equals the surface tension γ multiplied by the change of surface area dA.

$$dW = \gamma\, dA \tag{2.5}$$

In the case of constant temperature T and pressure p, γ equates the change of the Gibbs free energy dG per increase or decrease of dA. The surface tension γ depends on the volume V and the molar number n_M in Eq. (2.6).

$$\gamma = \left[\frac{dG}{dA}\right]_{V,n_M} \tag{2.6}$$

The Dupré equation (Dupre 1869) expresses the surface's Gibbs free energy ΔG (Eq. (2.7)),

$$\Delta G = W = \gamma_{LA} + \gamma_{SL} + \gamma_{SA} \tag{2.7}$$

where the work W is defined as the sum of the surface tensions of the interfaces in a liquid-solid-air system: γ_{LA} (liquid-air), γ_{SL} (solid-liquid) and γ_{SA} (solid-air) (Dupre 1869). Since wetting depends on the surface tension at the relevant interfaces, γ_{LA}, γ_{SL} and γ_{SA} are part of equations that express wetting phenomena. The contact angle [°] quantifies the wettability of a surface, and it is defined as the angle between the tangent to the liquid-air interface and the droplet's baseline at the contact-line of contact between the three phases, liquid, air and solid. Young's equation (Young 1805) Eq. (2.8) relates the contact angle at thermodynamic equilibrium θ_E to the surface tensions γ_{LA}, γ_{SL} and γ_{SA}.

$$\cos\theta_E = \frac{\gamma_{SA} - \gamma_{SL}}{\gamma_{LA}} \tag{2.8}$$

Commonly, a contact angle of 90° is defined as the threshold between hydrophilic and hydrophobic wetting behavior. However, researchers have derived another threshold at 65° by theoretical considerations and modelling. This threshold is often used in studies on surface forces (Vogler 1998, Yoon, Yang et al. 2003).

The Young contact angle is defined for an ideal surface, which is flat and chemically homogeneous (Marmur 1992). Consequently, Wenzel defined the contact angle θ_W for complete wetting on a chemically homogeneous but rough surface (Wenzel 1936). Wenzel introduced the roughness factor r_f as the ratio of the real surface to the geometric surface area.

$$\cos\theta_W = r_f \cos\theta_E \tag{2.9}$$

Thereby, roughness magnifies the surface’s inherent wetting behavior. However, Eq. (2.9) is no longer defined when the right-hand side reaches values greater than one (Johnson Jr. and Dettre 1964). Wenzel’s approach was later expanded to Eq. (2.10) to take heterogeneous surfaces into account, which consist of more than one chemically different material with respectively different wetting behavior (Bormashenko 2010).

$$\cos\theta_{CB} = \sum_{1}^{i} \varepsilon_i r_f \cos\theta_{E_i} \tag{2.10}$$

Eq. (2.10) quantifies wetting of a heterogeneous solid surface made of *i* sorts of materials with their respective fraction of the surface area ε_i. In the case of a droplet sitting on a rough surface with air trapped in the valleys between the asperities, the surface is considered to be a composite of air together with the solid material(s). For a surface of one single material and air trapped between the asperities, Eq. (2.10) reduces to the original Cassie-Baxter Eq. (2.11) (Cassie and Baxter 1944), where ε is the fraction of the wet solid surface and r_f is the roughness factor of the wet surface fraction. The wetting situation is then denominated as *Cassie state*.

$$\cos\theta_{CB} = \varepsilon\, r\cos\theta_E + \varepsilon - 1 \tag{2.11}$$

Since the contact angle between water and air is 180°, cos $\theta_E = 1$. Accordingly, for $\varepsilon = 1$, the Cassie-Baxter state answers to the Wenzel state.

Researchers further distinguish between the *apparent* contact angle (CA) (Tadmor 2011), which is measured with a goniometer for instance, and the *actual* CA (Tadmor 2004), which is the contact angle on the nanoscale, where the three phase contact-line touches the surface. The *apparent* CA is the average of various *actual* CAs. The above mentioned Young, Wenzel and Cassie-Baxter contact angles are used mainly in theoretical discussion, while the *apparent* CAs are measured and reported in experimental work. Depending on the measurement method, either static *sessile* CAs or *dynamic* CAs are reported as *apparent* CAs (Kietzig 2011). The dynamic contact angle is either the *advancing* or the *receding* CA (ARCA). The former is measured when a droplet is expanding across a surface, while the latter is determined when the droplet is shrinking. Thus, the advancing CA provides information about the wetting behavior on a practically dry surface, and the receding angle delivers the wettability of the wet surface. The difference between the advancing and the receding CA is reported as *hysteresis* and is characteristic for a particular surface of interest. The dynamic CAs are considered to deliver more realistic information about the wettability of a surface, since in real life situations, surfaces are not perfectly flat or chemically homogeneous, and a liquid is most likely not resting in a static state on a surface, but to a certain extent, moving across the surface.

Furthermore, the Wenzel and Cassie-Baxter wetting regimes and the measured apparent CAs mentioned above do not describe wetting for very small droplets or menisci. In the case that the size of the droplet or meniscus becomes similar to the size of surface asperities, the two wetting regimes are no longer valid (Extrand 2003, Extrand 2005). Then, phenomena such as wetting or condensations of thin films of water come into play. On the nanoscale, monolayers of water are always present on surfaces under ambient conditions (Israelachvili 2010). Although this small amount of water does not seem to be relevant for surface to surface interactions, various tribomechanical and tribochemical interactions, like the growth of capillary bridges contributing to friction, take place in and between these water layers (Scherge, Li et al. 1999, Jarn, Brieler et al. 2008).

The phenomena and related interactions described above are driven by long range surface forces like capillary forces and short range molecular van-der-Waals (vdW) forces. Thereby, the environmental conditions determine which force dominates (de Gennes 1985). In the following chapters, it will be explained how the extent of surface forces is related to the topology as well as the chemistry of a surface. Consequently, the wettability expressed by the apparent CAs will be linked with the magnitude of capillary forces.

2.3 Capillary forces

2.3.1 Surface forces and adhesion

Energies describe a state, however, forces are directed. In a system that consists of two solid surfaces and a medium like air or water present in between, all forces contribute to the total surface force (Scherge, Gorb et al. 2001). Surface forces have to be distinguished from body forces (Israelachvili 2010): The latter act among a number of molecules in a body, and the former at an interface of two media. The three main groups of surface forces that contribute to adhesion are electrostatic forces, vdW forces and capillary forces (Ata, Rabinovich et al. 2002, Riedo, Levy et al. 2002, Nosonovsky and Bhushan 2011). Adhesion can be defined as *macroscopic* in the sense that two macroscopic bodies adhere to each other with mechanical force transferred from one body to the other. In contrast, *microscopic* or *nanoscopic* adhesion refers usually to the situation when two phases interact across an interface or through a medium (Good 1976). This dissertation focusses on *nanoscopic* adhesion originating from capillary forces.

Electrostatic forces have to be mainly considered on non-conducting surfaces in a dry environment. On metallic surfaces they can be separated from the other surface forces by grounding (Butt 1991). However, due to their ability to act both as repulsive and adhesive force, they contribute to adhesion in different ways in an uncontrolled environment (Butt, Cappella et al. 2005). However, vdW forces exist always between two interacting surfaces, independently of the type of material or the environment. In a dry atmosphere, and when only a monolayer of water is present on a surface, vdW forces tend to be the dominant force (Stifter, Marti et al. 2000) and can be either attractive or repulsive (Israelachvili 1972). However, it has been shown that electrostatic and vdW forces get *diluted* at a certain level of vapor present between the surfaces due to the rise of capillary forces (Butt and Kappl 2009).

It is impossible to determine the extent of adhesion caused by surface forces between two solid surfaces without considering the action range of the different forces. While vdW forces are effective between two solid surfaces only at a distance of less than 5 nm (Stifter, Marti et al. 2000), the upper limit for capillary forces is the break-off distance of the meniscus, which has been found to be between 5 to 130 nm (Stifter, Marti et al. 2000) and up to 2.7 µm (Uzhegova, Svistkov et al. 2014).

2.3.2 Capillary condensation and formation of capillary bridges

The condensation of capillary bridges and the resulting adhesive force has been described as "water acting like glue" (Jinesh and Frenken 2006). Irving Langmuir explained how water tends to condense from the vapor phase inside small cracks or pores to form menisci and water films on a surface: The limited space in a pore or *capillary* triggers an increasing number of van-der-Waals interactions between water molecules in the vapor phase. These interactions cause the density of the vapor phase and the vapor pressure p_v to increase until the liquid state is reached. Consequently, a meniscus is formed during the phase change. Capillary condensation occurs below the saturation vapor pressure $p_s(T)$ and is linked via p_v to the relative humidity (Eq. (2.12)) in the environment (Langmuir 1918, Stifter, Marti et al. 2000, Szoszkiewicz and Riedo 2005, Israelachvili 2010).

$$relative\ humidity = \frac{p_v}{p_s(T)} \tag{2.12}$$

It has been shown that the formation of capillary menisci between smooth or rough surfaces follows a similar principle (Ata, Rabinovich et al. 2002): When two surfaces are at very close distance of several nanometers, capillary menisci condensate from the water present in the vapor phase. Thereby, menisci grow out of the water layer that is expected to be present on a surface in every non-controlled environment, even in the case of hydrophobic surfaces (Fisher and

Israelachvili 1981, Scherge, Gorb et al. 2001). Once the distance between the two surfaces is increased the stretched menisci are called *capillary bridges*, which can be the origin of strong adhesion (Butt and Kappl 2010). The separation of two surfaces and the simultaneous measurement of the adhesive force are typically realized with AFM (Jang, Schatz et al. 2004, Beach and Drelich 2011, Crassous, Ciccotti et al. 2011, Moore 2011), since AFM operates at the relevant force level and spatial resolution (Chapter 2.4).

Like surface wetting, the growth of capillary bridges is considered to be a thermodynamic process. This aspect has been studied comprehensively by Szoszkiewicz and Riedo *et al.* (Riedo, Levy et al. 2002, Gnecco, Riedo et al. 2003, Riedo and Gnecco 2004, Riedo, Pallaci et al. 2004, Szoszkiewicz and Riedo 2005, Sirghi, Szoszkiewicz et al. 2006). The nucleation time of a meniscus, which is understood as the time of capillary condensation from the vapor phase and the subsequent growth of a meniscus between two solid surfaces, depends on the temperature (Restagno, Bocquet et al. 2000) as well as on the vapor pressure p_v in the environment (Kohonen, Maeda et al. 1999, Sirghi, Szoszkiewicz et al. 2006). Considering only the thermodynamic conditions, the nucleation time is expected to be of the order of hours and days (Feiler, Jenkins et al. 2005, Feiler, Stiernstedt et al. 2007). However, the nucleation time observed by Szoszkiewicz *et al.* has been measured to be 5 ms for a sharp AFM tip and 1 s for a blunt tip. This time is much shorter than the expected time for the establishment of a thermodynamic equilibrium when only Brownian motion contributes to mass transfer and no thermal activation energy is present (Szoszkiewicz and Riedo 2005). Feiler *et al.* confirmed that capillary condensation occurs rapidly (Feiler, Stiernstedt et al. 2007). Later, capillary condensation at 200 s was measured with AFM (Banerjee, Mulder et al. 2012). Even though Kohonen *et al.* predicted this large hysteresis of the observed condensation time (Kohonen, Maeda et al. 1999), the formation of capillary bridges cannot be considered as a solely thermodynamic process (Sirghi, Szoszkiewicz et al. 2006).

As a possible explanation, researchers have postulated that non-thermodynamic driving forces like chemical potential gradients and wetting gradients within one of the interacting surfaces or between them may cause mass transfer between the vapor and the liquid phase (Drechsler 1983, Kohonen, Maeda et al. 1999, Malotky and Chaudhury 2001, Maeda and Israelachvili 2002, Jang, Schatz et al. 2004, Feiler, Jenkins et al. 2005, Laitinen, Bauer et al. 2013). Mechanical instabilities of the interfaces driven by vdW forces could also explain capillary condensation (Maeda and Israelachvili 2002). Furthermore, liquid films present on the two solid surfaces could coalesce to form a meniscus while the surfaces approach (Butt and Kappl 2009). However, even these non-equilibrium processes depend on a critical relative humidity, below which no condensation is possible (Ata, Rabinovich et al. 2002).

The observation made by Szoszkiewicz *et al.* that the nucleation time of capillary bridges depends on the radius of the AFM probe (Szoszkiewicz and Riedo 2005) has furthermore implied that the nanoscale topography of the two interacting surfaces plays a role during capillary condensation. The quantitative influence of the all the above mentioned thermodynamic and non-thermodynamic parameters on the magnitude of capillary forces can be seen from the derivation of the Kelvin-Laplace model in the following chapter.

2.3.3 Derivation of the Kelvin-Laplace model

The Kelvin-Laplace model is the starting point for the quantitative description of capillary forces. It links the thermodynamic conditions in a certain environment like the relative humidity (Eq. (2.12)) to the shape and size of a droplet or a meniscus. The Young-Laplace Eq. (2.13) quantifies the dependence of the radii of curvature r_1 and r_2 of a droplet or meniscus (Figure 2.2) on the pressure difference Δp (*Laplace pressure*) across the phase interface.

$$\Delta p = \gamma_{LA}\left(\frac{1}{r_1} + \frac{1}{r_2}\right) \tag{2.13}$$

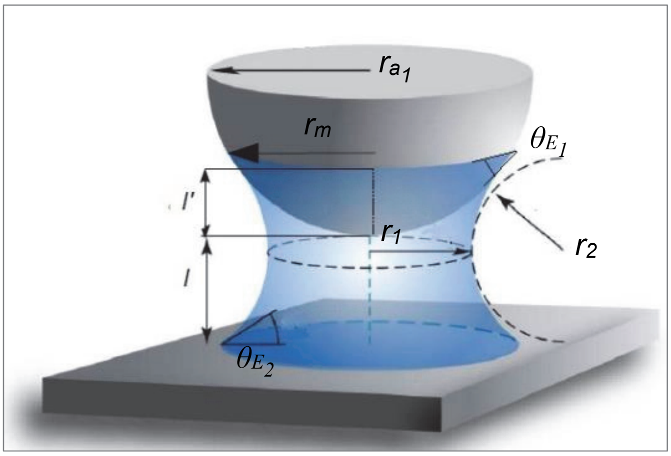

Figure 2.2: Capillary bridge between a curved and a flat surface

Eq. (2.13) has been modified to Eq. (2.14) by de Gennes *et al.* to link the Laplace pressure Δp to the equilibrium contact angle θ_E for an idealized case of a spherical surface of radius r_{a_1} at distance l to a flat surface, while both surfaces have the same θ_E (Figure 2.2) (de Gennes, Brochard-Wyard et al. 2003). Therefore, de Gennes *et al.* linked the wetting behavior of a surface to the shape of the meniscus formed in between two surfaces.

$$\Delta p = \gamma_{LA}\left(\frac{1}{r_1} + \frac{1}{r_2}\right) = \gamma_{LA}\left(\frac{1}{r_{a_1}} - \frac{cos\theta_E}{l/2}\right) \tag{2.14}$$

In other words, the balance between the surface tension of the liquid-air interface (γ_{LA}) and the difference Δp between the vapor pressure p_v and the pressure inside the meniscus determines the shape of the meniscus. In this context, γ_{LA} is interpreted as a force F per unit length normal to the plane and directed to the centre at distance l of the droplet's surface (Eq. (2.15)).

$$\gamma_{LA} = \frac{F}{l} \tag{2.15}$$

The contact angle θ_E in Eq. (2.14) indicates that the formation of a meniscus, and hence capillary bridges, depends on the wetting behavior on the two interacting surfaces (Figure 2.2). The concepts of surface tension and contact angles are valid on the micro- and nanoscale (de Gennes 1985). However, Figure 2.2 shows that the actual contact angles do not depend only on the wettability of the respective surfaces, but also on the distance *l* between the two solid surfaces and the volume of the capillary bridge.

The modified Laplace equation (Eq. (2.14)) does not quantify the mechanical aspects of the Laplace pressure Δp that are given by the liquids physical properties. The *gravitational distribution law* (Eq. (2.16)), which is the hydrostatic formula for the vapor pressure p_v in a liquid-vapor system, provides the mechanical aspects of the vapor-liquid phase interface.

$$p_v = p_s(T)\exp\frac{\rho g l_{va} V_M}{k_b T} \tag{2.16}$$

The vapor pressure's p_v dependence on the gravitational acceleration g, the liquid's density ρ, the average distance between the molecules in the vapor phase and the liquid film l_{va}, the molecular volume of the liquid v_m and the Boltzmann constant k_b is expressed in Eq. (2.16). The repulsive pressure *p(d)* in Eq. (2.17), which is the disjoining pressure of a liquid film of thickness *d* caused by vdW forces, introduces the inner pressure of a droplet or meniscus as a force acting against the vapor pressure (Israelachvili 2010, Nosonovsky and Bhushan 2011).

$$p(d) = \rho g l_{va} \tag{2.17}$$

The substitution of Eq. (2.17) into Eq. (2.16) and the subsequent derivation towards *p(d)* prompt to the general Eq. (2.18), which ultimately links the disjoining pressure *p(d)* of a liquid film to the relative humidity of the surrounding air (Eq. (2.12)).

$$p(d) = \left(\frac{k_b T}{V_M}\right)\ln\left(\frac{p_v}{p_S(T)}\right) \tag{2.18}$$

Connecting Laplace Eq. (2.14) with Eq. (2.18) leads to the Kelvin-Laplace model (Eq. (2.19)), which defines r_{curv} as the meniscus's mean curvature at thermodynamic equilibrium between liquid and air or vapor (Israelachvili 2010). In doing so, the Laplace pressure Δp equals thermodynamically the repulsive pressure $p(d)$.

$$\frac{1}{r_{curv}} = \left(\frac{1}{r_1} + \frac{1}{r_2}\right) = \frac{k_b T}{\gamma_{LA} V_M} ln \frac{p_v}{p_s(T)} = \frac{\Delta p}{\gamma_{LA}} \tag{2.19}$$

The Kelvin-Laplace model expresses the curvature of the meniscus r_{curv} as a function of the temperature T and the relative humidity ($p_v/p_s(T)$). Hence, the Kelvin-Laplace model explains the growth of capillary bridges and their dependence on the relative humidity. When p_v becomes too low, r_{curv} is similar to the size of water molecules and the model does not longer hold true. It has been shown that in this case molecular fluctuations of water influence the shape of menisci on the nanoscale (Jang, Schatz et al. 2004). Eq. (2.19) can be further modified to the Kelvin-length λ_K (Eq. (2.20)), which equates from two times r_{curv} multiplied by $cos\ \theta_E$.

$$\lambda_K = \frac{\gamma_{LA} V_M}{k_b T} = 2 r_{curv} cos\theta_E \tag{2.20}$$

The Kelvin-length is the minimum distance between two surfaces where capillary condensation is possible. It is mainly a material property of the liquid and depends also on the temperature and the contact angle θ_E of the interacting surfaces, here assumed to be equal on both surfaces.

2.3.4 Calculation of capillary forces

There are different ways to calculate the capillary force based on the Kelvin-Laplace model depending on the known variables. The surface geometries, the contact angles and the geometry of the meniscus are all difficult to determine, since measurements on the nanoscale are required (Butt and Kappl 2009). The Kelvin-Laplace model (Eq. (2.19)) can be simplified for the case that the geometry of the meniscus is known and the topology of the surface is not of interest (Eq. (2.21)).

$$\Delta p = \frac{\gamma_{LA}}{r_{curv}} \tag{2.21}$$

The Laplace pressure Δp acts as a force on the area that is given by the radius r_m of the circle of the liquid solid contact line and the height of the meniscus rising on the asperity l' (Figure 2.2). This area equals the liquid-solid interface between the meniscus and the surface of the spherical asperity. Hence, Eq. (2.21) multiplied by the area leads to the capillary force F_{cap} in Eq. (2.22). In the case that $r_{curv} << r_{a_1}$, Israelachvili has suggested to eliminate r_{curv} from Eq. (2.22).

$$F_{cap} = 2\pi r_m l' \left(\frac{\gamma_{LA}}{r_{curv}}\right) \tag{2.22}$$

Since the curvature of the meniscus r_{curv} can be expressed by Eq. (2.23),

$$r_{curv} = \frac{l' + l}{2cos\theta_E} \tag{2.23}$$

Eq. (2.22) becomes Eq. (2.24) (Israelachvili 2010).

$$F_{cap}(l) = \frac{(2\pi r_m \gamma_{LA})(2cos\theta_E)}{1 + \frac{l}{l'}} \tag{2.24}$$

Hence, the equilibrium contact angle θ_E is introduced into the equation. Even though it is impossible to determine θ_E experimentally, Eq. (2.24) allows quantifying the influence of the surface wettability on the magnitude of the capillary force F_{cap}.

Eq. (2.24) becomes Eq. (2.25), which is widely used in literature, in the case that the two surfaces have different equilibrium contact angles (Ando 2000, Ata, Rabinovich et al. 2002, Riedo, Levy et al. 2002, Israelachvili 2010). However, Eq. (2.25) can only be used for atomically flat surfaces since the geometry of the two interacting surfaces on the nanoscale is not considered.

$$F_{cap} = \frac{2\pi R' \gamma_{LA}(cos\theta_{E_1} + cos\theta_{E_2})}{1 + \frac{l}{l'}} \tag{2.25}$$

2.3.5 Influence of surface topology and surface chemistry on capillary forces

The relationship between surface forces and topology has been firstly described by the Derjaguin approximation for surface forces like vdW forces and electrostatic forces (Derjaguin 1934). Since the total surface area determines the amount of the resulting surface force (Israelachvili 2010), and rough surfaces have a larger effective surface area than smooth surfaces, higher contributions from vdW forces and electrostatic forces are expected on rough surfaces (Butt and Kappl 2010).

However, in the case of capillary forces, the magnitude of the force depends only on the surface area, where capillary bridges can be formed, which is not identically with the total surface area. We have seen in the previous chapter 2.3.4 that the radii of the meniscus of a capillary bridge (Figure 2.2) depend on the relative humidity around the contact zone, and the wettability of the interacting substrates. However, the above shown equations do not consider the interaction between two rough surfaces. Ata *et al.* as well as Butt *et al.* have developed Eq. (2.26) and Eq. (2.27) for the case of a rough surface interacting with a flat one, and two rough surfaces interacting respectively (Ata, Rabinovich et al. 2002, Butt and Kappl 2009). The topology of the two surfaces (roughness) is quantified by the radii r_{a_1} and r_{a_2}. In both equations, surface features that compose the roughness are considered to be spherical (curved). The wetting behaviour of the two interacting surfaces is expressed by the wettability factor c with β as a geometrically derived correcting angle (Eq. (2.28)).

$$F_{cap} = 2\pi\gamma_{LV}\left(2c - \frac{l}{r_{curv}}\right) r_{a_1} \tag{2.26}$$

$$F_{cap} = 2\pi\gamma_{LV}\left(2c - \frac{l}{r_{curv}}\right)\left(\frac{r_{a_1} r_{a_2}}{r_{a_1} + r_{a_2}}\right) \tag{2.27}$$

$$c = \frac{cos(\theta_{E_1} + \beta) + cos(\theta_{E_2})}{2} \tag{2.28}$$

Feiler *et al.* and Butt *et al.* have pointed out that r_{a_1} and r_{a_2} do only influence the formation of capillary bridges when their dimensions are of the relevant length scale (Feiler, Jenkins et al. 2005, Butt and Kappl 2009). This length scale is given by the curvature of the meniscus r_{curv} (Eq. (2.19)) and the Kelvin-length λ_K (Eq. (2.20)).

In general, capillary forces depend on the number of capillary bridges that rise between the two interacting surfaces (Ando 2000). However, all equations for F_{cap} that were presented in chapter 2.3.4 and chapter 2.3.5 consider only one single capillary bridge so that they do not serve real life scenarios, where a multitude of capillary bridges are formed. Ando as well as Butt *et al.* have shown in their research on asperity arrays that the magnitude of capillary forces on a rough surface does not depend on the total surface area, like in the case of vdW forces, but on the number of asperities and contact points that are available for capillary growth (Ando 2008, Butt and Kappl 2010). Hence, roughness decreases the capillary force since fewer contact points between the two interacting surfaces are available (Ata, Rabinovich et al. 2002).

However, capillary force does not only depend on the length scale of the roughness but also on the shape of the asperities (Ando 2000, Butt and Kappl 2009). It has been observed that the Laplace pressure Δp increases for a capillary bridge on a sharp thin asperity with decreasing contact area between the condensing water and the solid; this behavior can be derived from the Laplace equation (Eq. (2.13)). Hence, each capillary bridge on a sharp asperity exhibits a larger capillary force than one on a broader asperity (O'Shea, Lantz et al. 1997, Heuberger, Drummond et al. 1998, Scherge, Gorb et al. 2001). It has to be understood that the degree of roughness does not alone indicate, whether capillary forces are promoted or not. Hence, the surface topology has to be determined with AFM or high magnification SEM on the nanoscale previously to any capillary force measurements. However, there is no comprehensive model that describes the growth of multiple capillary bridges and the resulting capillary force on all length scales, roughness levels and surface geometries (Nosonovsky and Bhushan 2011).

The influence of the chemical composition on the formation of capillary bridges is also not represented in a satisfactorily way in the equations above. Even though the contact angles in the respective equations for F_{cap} (Eq. (2.25), Eq. (2.28)) represent the chemical composition of the two interacting surfaces on the nanoscale, they do not permit to explain the role the surface chemistry plays during capillary condensation. Acharya *et al.* for instance has investigated the interaction of water with a hydrophobic surface on the nanoscale. He has shown that density fluctuations in the vapor phase occur due to chemical heterogeneities on hydrophobic surfaces that trigger the formation of thin water films even on hydrophobic surfaces (Acharya, Vembanur et al. 2010). As explained in chapter 2.3.2, the existence of such a thin water film promotes capillary forces.

2.4 Atomic force microscopy

Measuring surface forces is based on one simple principle (Butt 1991): Force acts on a probe with a spring constant k_s resulting in a deflection Δz of the cantilever (Eq. (2.29)).

$$F = k_s \Delta z \qquad (2.29)$$

The force F is plotted against an accurate position axis (z), while Δz is converted via k_s into force values. The measured force is usually in the range of a few nN to several µN. The spring constant k_s has to be obtained before every measurement, since it depends on the probe's mass, which can change during the experiments due to loss or accumulation of material on the probe. *Static* mode direct force AFM was the first AFM force measurement method applied by researchers: The probe is lowered to the surface and withdrawn immediately or after a certain delay time (*dwell*) or trigger values is reached. The deflection Δz of the cantilever then depends on the extent of either attractive ($+\Delta z$ towards the surface) or repulsive ($-\Delta z$ away from the surface) forces (Figure 2.3a). These so called *pull-off-force* measurements in contact mode are very common to characterize surface forces (Nguyen, Nalaskowski et al. 2003, Israelachvili 2010). Besides single force plots, researchers obtain arrays of force plots on a surface, which are typically called *force maps* (Figure 2.3b). Force maps allow locating force gradients across the surface with nanometer resolution.

(a)

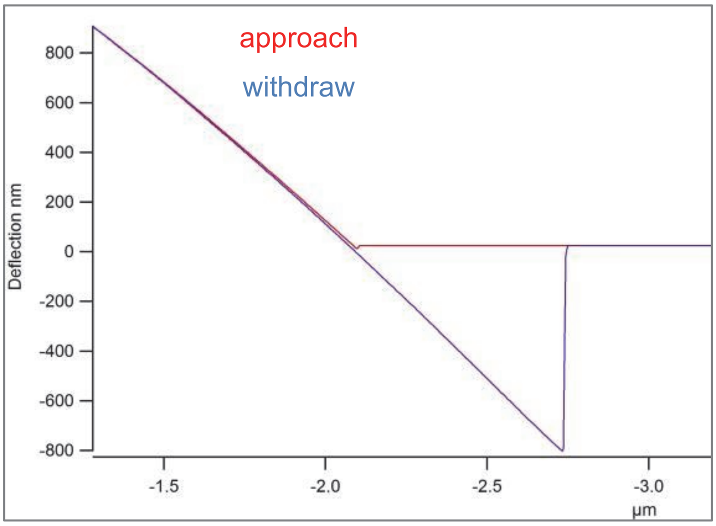

(b)

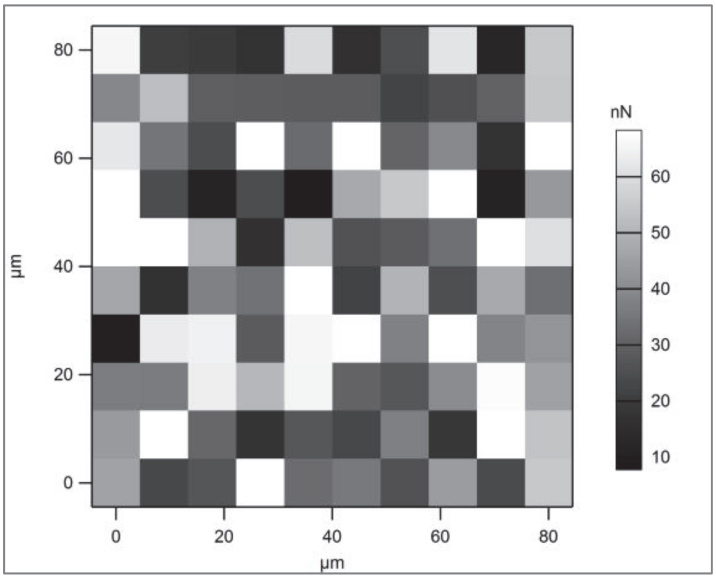

Figure 2.3: Typical force plot (a). 2D force map with 100 force plots (b).

Force mapping further permits obtaining multiple data points for statistical analysis on a single sample. Static AFM modes, however, can suffer from low resolution and can only quantify the total surface force but not the single components. The general challenge in AFM is limiting the noise that is generated by the environment (mechanical vibrations, thermal changes, air flow etc.).

The selection of the probe is crucial for every AFM measurement. In general, researchers can choose between soft and hard probes. Soft probes have a low spring constant ($k_s < 1$ N/m) and hard probes have a high spring constant ($k_s > 1$ N/m). Furthermore, the resonance frequency f_0 determines together with k_s the sensitivity of the measurement regarding the detectable force level. However, force sensitive probes suffer more from noise. The proper choice of the dimensions of the probe's tip is crucial for precise measurements on surfaces, since the size of the tip determines which forces can be measured (Nelson, Dodson et al. 1992).Capillary forces can only be successfully detected by using a *colloidal probe* with a diameter of a few micrometer (Figure 2.4), so that sufficient capillary bridges can rise between the tip and the sample (Ducker, Senden et al. 1991, Scherge, Gorb et al. 2001, Bhushan and Jung 2010).

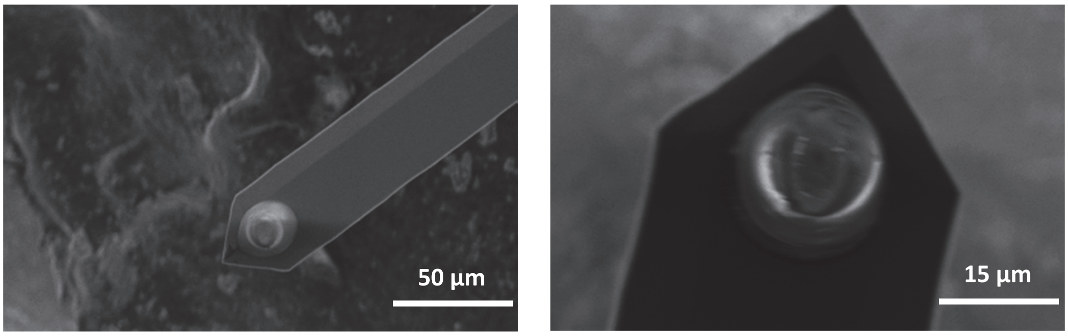

Figure 2.4: Self-made colloidal AFM probes for capillary force measurements.

Research on capillary forces measured with AFM is usually conducted in an environment where the relative humidity is controlled (Beach and Drelich 2011), since the magnitude of capillary forces depend on the vapor pressure in the environment (Eq. (2.19)).

Chapter 3

3. Production of homogeneous microstructures by femtosecond laser micromachining

3.1 Preface

This chapter presents an article that has been published in the journal *Optics and Lasers in Engineering*. The complete citation of the published article is:

Lehr, J. and Kietzig, A.-M., Production of homogeneous microstructures by femtosecond laser micromachining. Optics and Lasers in Engineering, 2014. 57(1): p. 121-129.

Studies on wettability and capillary forces are ideally conducted on surfaces that are covered with arrays of homogeneously distributed and equally sized features to ensure that the sample surface exhibits the same behavior independently of the location. This is of particular importance during the measurement of dynamic contact angles on these surfaces. Feature size, geometry and spacing of the surface features strongly influence the resulting contact angles, since they determine the wetting state. Thus, these surface variables have to be controlled.

The goal of the initial set of experiments was to identify the experimental parameters to obtain homogeneous arrays of microstructures on titanium. In particular, it had to be understood whether a uniform intensity distribution across the micromachined array is required to obtain homogeneous arrays of structures. Furthermore, the calculation of the line overlap φ_{line} and the accumulated input intensity $I_{pulse\text{-}accumulated}$ and $I_{line\text{-}accumulated}$ had to be reviewed regarding the use of the different possible reference areas that are required to quantify the spatial intensity input on the sample (see also chapter 2.1.1).

Production of homogeneous microstructures by femtosecond laser micromachining

Jorge Lehr, Anne-Marie Kietzig

Department of Chemical Engineering, McGill University, 3610 University Street, QC H3A 2B2 Montreal, Canada

Abstract

Two types of homogeneous microstructures have been produced by scanning femtosecond micromachining at a repetition rate of 10 kHz. The contribution of line-intensity and line-overlap on the initial formation, the growth and the final feature dimensions has been investigated. *Pillow-like* structures were obtained at a wide range of line-overlap values and at moderate intensities. *Bumpy* structures were produced at a tighter range of overlap and at higher intensities. The different resulting topologies were explained with the existence of two different thermal ablation regimes. The simulation of the resulting intensity profiles has shown that homogeneous *pillow-like* structures are obtained at a flat intensity profile, while homogeneous *bumpy* structures are produced with a wavy profile. Furthermore, the effective beam diameter has to be determined visually from the width of a single line. Then the line-overlap is calculated based on the effective beam diameter to achieve homogeneous structures.

3.2 Introduction

Femtosecond (fs) laser micromachining is a widely used method to create features on surfaces (Nolte, Momma et al. 1997, Perrie, Gill et al. 2004, Groenendijk and Meijer 2006, Oliveira, Ausset et al. 2009, Jiwhan, Jae-Hoon et al. 2010, Jagdheesh, Pathiraj et al. 2011). After its introduction almost 20 years ago it has become a promising technique to obtain a desired surface topology. Homogeneous surface structures on the microscale are necessary for the application of fs-laser micromachining when aiming for reproducible results in topology-sensitive fields like anti-wetting or microfluidics (Gomez, Goenaga et al. 2005, Baojia, Ming et al. 2008, Tang, Hong et al. 2010, Kietzig, Mirvakili et al. 2012). Thereby, superhydrophobic metallic surfaces obtained from fs-laser micromachining have been shown to be advantageous to control phenomena like ice-friction (Kietzig, Hatzikiriakos et al. 2009).

Fundamental research on fs-laser micromachining has been carried out under static conditions since 1997 (Liu, Du et al. 1997, Tsukamoto, Asuka et al. 2006, Petkov, Dimov et al. 2008), where the target and the laser beam are stationary. In a dynamic situation a scanning laser beam is used to build up a *patch*, instead of drilling holes (Groenendijk and Meijer 2006, Nayak, Gupta et al. 2008, Romer, Huis in't Veld et al. 2009, Jiwhan, Jae-Hoon et al. 2010). Our work focuses on the dynamic situation, where the target's surface is affected by a scanning spatially overlapping Gaussian laser beam. Two situations are relevant to laser micromachining: Firstly, when pulses overlap (φ_{pulse}), while a single line is machined; secondly, when lines overlap (φ_{line}) to produce a patch. A few researchers have previously explored the role of overlap for micromachining with a Gaussian laser beam. Vogel and Backlund were the first to mention the term "overlap" in the context of laser micromachining of a larger area. They pointed out that overlap is an essential parameter for producing a regular surface topology (Vogel and Backlund 1965). A detailed investigation of both types of overlap (φ_{pulse}, φ_{line}) has been published by Venkatakrishan *et al.*. The authors concluded that larger φ_{pulse} results in increasing number of pulses per spot (PPS) (Venkatakrishnan, Stanley et al. 2003). Furthermore, they considered φ_{line} to be irrelevant due to a time delay of several seconds between the scanning of two consecutive lines. Cheng *et al.* found a correlation of φ_{pulse} and φ_{line} with the resulting surface roughness (Cheng, Perrie et al. 2009). The authors linked both φ_{pulse} and φ_{line} to the resulting overall energy distribution of several overlapping Gaussian beams. They stated that a flat energy profile with φ_{pulse} and φ_{line} around the spatial full-width-half-maximum (FWHM) is necessary for the formation of homogeneous surface structures. Jagdheesh *et al.* varied only φ_{pulse} but kept φ_{line} constant at 50 % (Jagdheesh, Pathiraj et al. 2011). Eichstädt *et al.* (Eichstädt, Römer et al. 2013) also used the same φ_{pulse} and φ_{line} in *x*- and *z*-direction, calculated the resulting intensities and discussed wavy and flat energy profiles that result from different overlap values. Recent work by Least and Willis illustrates that surface features with constant dimensions can be obtained by varying φ_{pulse} and φ_{line} systematically (Least and Willis 2013). Like Venkatakrishan *et al.* the authors found a correlation between PPS and the development of microstructures (Venkatakrishnan, Stanley et al. 2003). Furthermore, they have considered the possibility that the delay attributed to φ_{line} is relevant in the case of a phase change from a solid state to a molten state. Thereby, a subsequent pass interacts differently with a previously melted surface as compared to the interaction with the virgin solid surface. Yet, the specific role of line-overlap (φ_{line}) as a parameter for micromachining of homogeneous structures has not been identified.

In this work, we emphasize three aspects of fs-laser micromachining, where the understanding of φ_{line} is crucial for the resulting surface topology. Firstly, the determination of the required φ_{line} is discussed. Secondly, threshold values and combinations of parameters for feature formation are identified for certain microstructures, which then constitute a homogeneous patch. Thirdly, it is shown, how the formation and the dimensions of homogeneous microstructures depend on the local and the total energy exposures of the surface, as determined by the line intensity $I_{pulse\text{-}accumulated}$ and the line overlap φ_{line}.

3.3 Theory

Ablation is the phenomenon of removing material from a surface when it is exposed to an energy level that is greater than the binding energy of the ions in a lattice or in a molecule (Nicholls and Ferguson 1964). The amount of energy that is needed to initiate ablation at a certain threshold depends strongly on the ion- and electron-configuration of the target material (Gamaly 2011). This energy is the most important parameter for laser micromachining, since it is directly correlated to the ablation rate and thus to the formation of microstructures (Cheng, Perrie et al. 2009). Typically, the energy input is described with quantities that include the time of exposure and/or a reference area, such as *intensity* [W/cm^2], *fluence* [J/cm^2] and *power* [W]. Intensity is the most versatile descriptor containing a temporal and a spatial component. In the following, only intensity will be used to quantify the energy a surface is exposed to. Intensity (I_0) is defined as peak power (P) divided by the beam area, which is calculated from the beam diameter (ω) (Eq. (3.1)).

$$I_0 = \frac{P}{\pi\left(\frac{\omega}{2}\right)^2} \tag{3.1}$$

Eq. (3.1) expresses the average intensity and disregards the fact that the intensity varies across a Gaussian beam and a patch that constitutes of overlapping lines. Thus, Eq. (3.2) describes the accumulated intensity ($I_{line\text{-}accumulated}$) at an arbitrary spot on a patch, depending on its position (Figure 3.1) defined by the x, z coordinates (Eichstädt, Römer et al. 2013).

$$I_{line-accumulated}(x, z, i_x, j_z) = I_0 exp\left(-2\left(\frac{\left(x + \frac{v_0}{f_p} i_x\right)^2 + \left(z + \frac{v_0}{f_p} j_z\right)^2}{\left(\frac{\omega}{2}\right)^2}\right)\right) \tag{3.2}$$

The parameters i_x and j_z indicate the respective location on the Gaussian distribution for the coordinates x and z and determine the intensity at that location (Figure 3.1). The repetition rate is considered by f_p and the scanning velocity by υ_0.

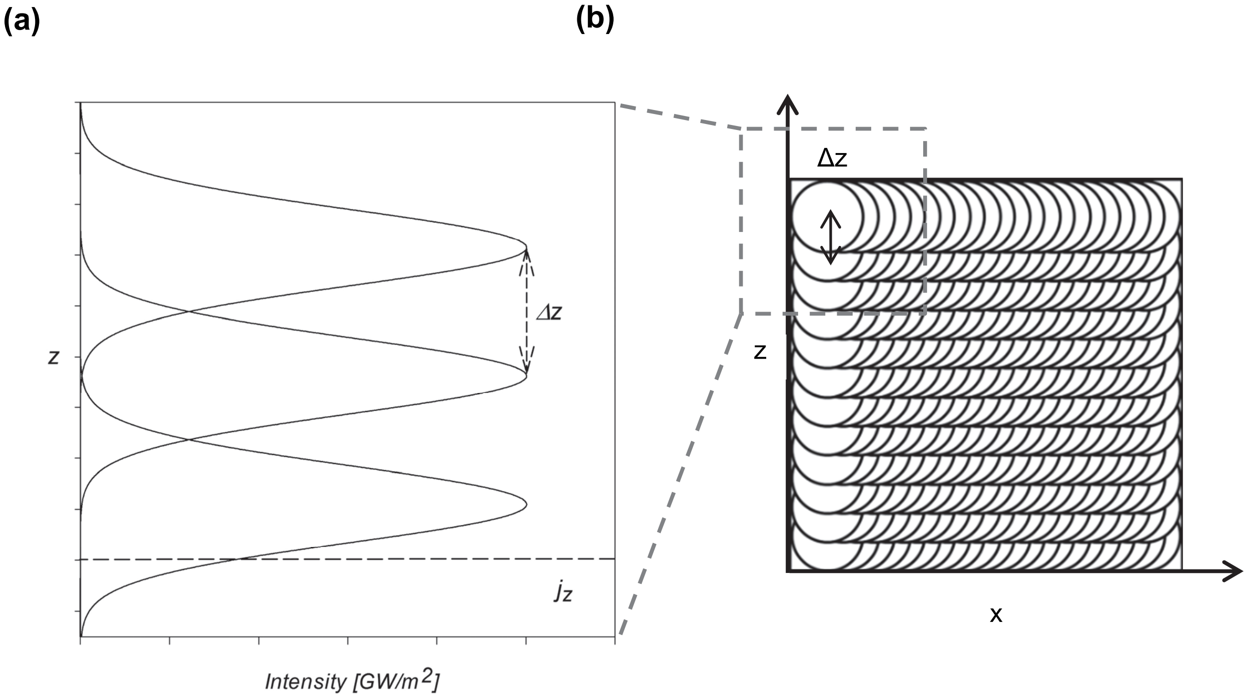

Figure 3.1: Schematic of overlapping (φ_{line} = 50 %) laser beams in *z*-direction forming a patch (b) and the resulting intensity profile (a).

The determination of the spatial limits of a Gaussian beam is challenging. While the purely statistical definition of a Gaussian distribution sets its limits to be infinite, limits have to be defined for practical applications. The widely accepted definition of the limits is set in the standard ISO 11146-2:2005 (ISO 2005). This standard defines the beam diameter ω as two times the distance between the peak intensity I_0 of the laser beam and the point of the energy distribution, where the energy level falls to 0.135 or $1/e^2$ of the maximum intensity. Another definition is given by the FWHM, where the respective intensity level is 0.5 of the maximum of the Gaussian distribution. Both concepts serve to standardise the communication of the beam diameter. However, the actual diameter of a micromachined line depends on the material's ablation threshold under the employed experimental conditions and is therefore not identical with the beam diameter. Hence, both can serve as a reference area in intensity and overlap calculations. Here, we distinguish between $1/e^2$ as the theoretical beam diameter (ω_{theo}) and the effective width of an ablated line (ω_{eff}). The line width ω_{eff} can be either larger or smaller than ω_{theo} depending on whether the intensity at ω_{theo} is above or below the ablation threshold. Researchers tend to use the theoretical diameter ω_{theo} as a reference area in the calculation of fluence and intensity (Perrie, Gill et al. 2004, Groenendijk and Meijer 2006, Paschotta 2008, Kam, Bhattacharya et al. 2012), since it allows to report values for I_0 and $I_{line\text{-}accumulated}$ as well as the respective intensity thresholds that are independent from the experimental conditions. However, as outlined in the following ω_{eff}, which depends on a specific ablation threshold and is a function of the energy applied during the micromachining process, seems the more suitable parameter in the calculation of the overlaps.

Figure 3.1 illustrates overlap in *x*- and *z*-direction. Micromachining a line or a patch with a scanning Gaussian beam requires an overlap φ [%] to compensate for the decreasing energy towards the tails of the distribution in order to achieve a homogeneous energy exposure of the target surface. Eq. (3.3) describes the overlap of consecutive pulses along a line φ_{pulse} in *x*-direction. The overlap φ_{pulse} depends on repetition rate f_p and scanning velocity υ_0.

$$\varphi_{pulse} = \left(1 - \frac{v_0}{\omega\, f_p}\right) \times 100 \tag{3.3}$$

Eq. (3.4) represents the overlap of consecutive lines φ_{line} in z-direction with a distance Δz between the centers of the overlapping lines at v_0.

$$\varphi_{line} = \left(1 - \frac{\Delta z}{\omega}\right) \times 100 \tag{3.4}$$

Thereby, the energy exposure of the target surface is *immediate* for φ_{pulse} in one direction and *delayed* for φ_{pulse} in the orthogonal direction. Both φ_{pulse} and φ_{line} contribute to the total intensity, to which the target surface is exposed. In the case of repetition rates above 5 kHz the denominator of Eq. (3.4) governs the calculation of φ_{pulse} and only large v_0 values of more than 10 mm/s allow φ_{pulse} to decrease below 90 % for values of ω_{theo} of up to 50 µm. The line-overlap φ_{line} is set independently from f_p and v_0 but based on a distance, which can be either ω_{theo} or ω_{eff}.

Eq. (3.2) has been modified to Eq. (3.5) in order to permit the discrimination between the immediate and the delayed energy inputs into the target surface. Eq. (3.5) allows calculating the intensity of the pulse-train in x-direction $I_{pulse\text{-}accumulated}$, which is the intensity that results from φ_{pulse}.

$$I_{pulse-accumulated}(x, i_x) = I_0 exp\left(-2\left(\frac{\left(x + \frac{v_0}{f_p} i_x\right)^2}{\left(\frac{\omega}{2}\right)^2}\right)\right) \tag{3.5}$$

At large values of φ_{pulse} above 99 % the intensity profile in x-direction is basically flat so that $I_{pulse\text{-}accumulated}$ can be substituted as a constant into Eq. (3.2) to give Eq. (3.6), which allows the calculation of $I_{line\text{-}accumulated}$ from overlapping line intensities.

$$I_{line-accumulated}(z, j_z) = I_{pulse-accumulated}\,exp\left(-2\left(\frac{\left(z + \frac{v_0}{f_p} j_z\right)^2}{\left(\frac{\omega}{2}\right)^2}\right)\right) \tag{3.6}$$

A certain overlap value φ is required to obtain a particular periodicity or homogeneity of structures. Typically, the surface topology that results from the micromachining process is evaluated visually and φ_{pulse} and φ_{line} are adjusted accordingly. Which φ to modify is decided based on the desired surface pattern. Clearly, both ω_{theo} and ω_{eff} can be used as reference area to calculate φ_{pulse} and φ_{line} in Eq. (3.3) and Eq. (3.4). All the above introduced aspects regarding intensity and overlap have been applied and verified throughout our experiments, as outlined in the following.

3.4 Materials and methods

A Coherent Libra femtosecond laser system with wavelength of 800 nm and pulse duration of <100 fs was used for the experiments. The average laser output power of 4 W was attenuated to the desired level by combining a half-wave plate and a polarizing beam splitter. Titanium samples (99.9 % purity, McMaster-Carr, USA) were polished with 600 grit and 1200 grit sand paper and cleaned before and after micromachining with acetone in an ultrasonic bath for 10 min. The samples were mounted perpendicular to the beam on a computer controlled translation stage inside a sealed reactor vessel. The laser beam entered the reactor vessel through a 6.35 mm thick silica glass window (refractive index $n_r = 1.46$). Experiments have been conducted in air at 450 Torr. The laser beam was focussed with a 200 mm lens to a theoretical beam diameter ω_{theo} of 66 µm. The lens was mounted on a micrometer-stage to adjust the distance between lens and sample surface. Lines of 3 mm length were micromachined for average power values between 0.015 and 2 W to determine the effective beam diameter ω_{eff} for different power settings. The scanning velocity v_0 was 1.5 mm/s and the repetition rate f_p was 10 kHz. Both were held constant resulting in φ_{pulse} of 99.7 % and in a constant number of 300 pulses per spot (PPS) throughout all experiments. Square patches with an area of 9 mm^2 were micromachined, while the translation stage moved back and forward in *x*-direction and downwards in *z*-direction. The displacement Δz of the translation-stage was calculated for different φ_{line} between 50 and 90 %. Scanning electron microscopy (SEM) images of the surface morphology were taken with a Phenom™ FEI. Intensity profiles were simulated with Microsoft Excel. Based on the SEM images average dimensions have been determined. On each SEM n=30 feature diameters in *x*- and *z*-direction have been measured and the average has been calculated. The measurements have been taken in a fixed pattern following a line from the lower right to the upper left of the SEM image for 23 different experimental settings.

3.5 Results

3.5.1 Theoretical beam diameter and line width

The resulting structures are illustrated for the cases when the theoretical beam diameter ω_{theo} (Figure 3.2a and c) and the effective line width ω_{eff} (Figure 3.2b and d) have been used as a reference in Eq. (3.1) to Eq. (3.6) to calculate φ_{line} for two lines overlapping at 50 % and 70 %. Figure 3.3a and c show that material was left unaffected between the two ablated lines when ω_{theo} has been used to calculate φ_{line}, because the actual line width ω_{eff} (35 µm) was smaller than the theoretical diameter ω_{theo} (66 µm).

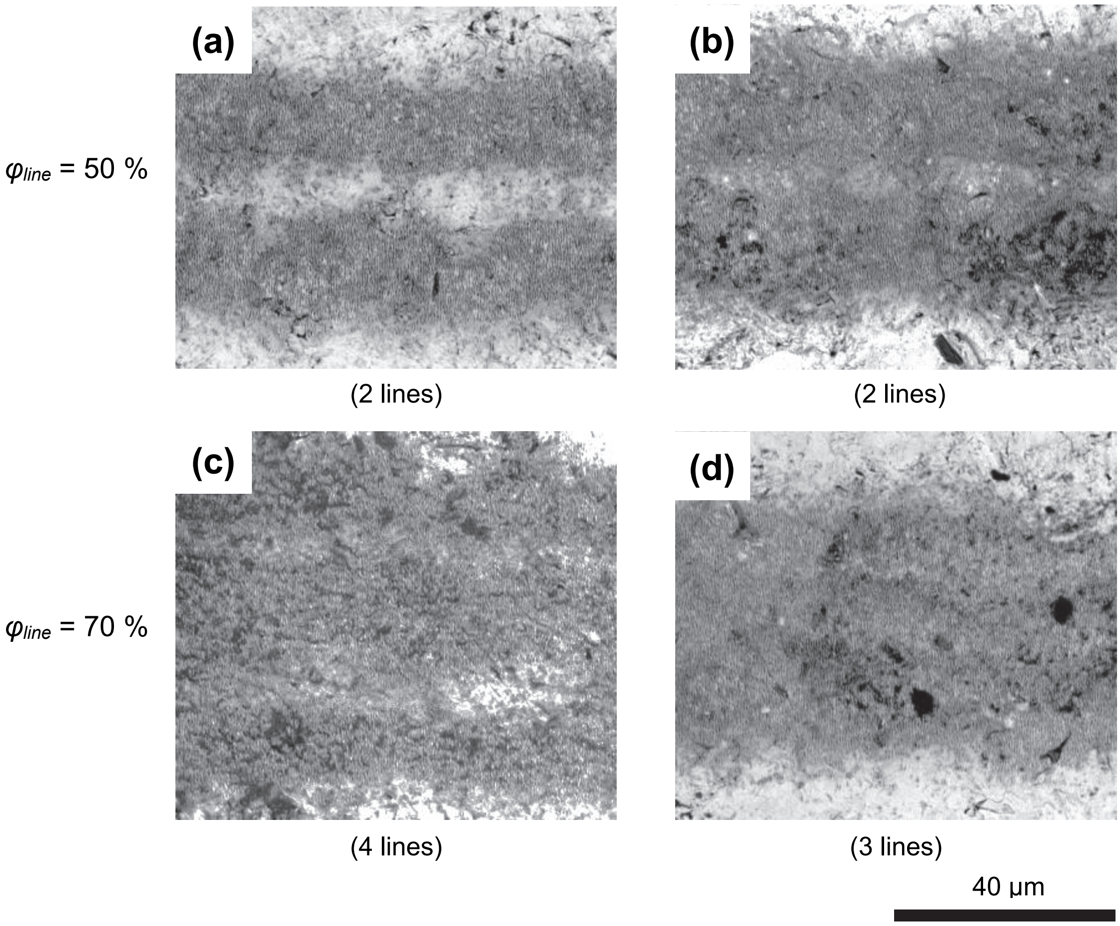

Figure 3.2: Overlapping lines at $I_{pulse\text{-}accumulated} = 0.29$ GW/m^2 with φ_{line} calculated from the theoretical beam diameter ω_{theo} (a and c) or the effective beam diameter ω_{eff} (b and d).

However, a nearly continuous area has been produced in the case of Figure 3.2b and d when ω_{eff} had been used to calculate φ_{line}. The adjustment of φ_{line} based on visual observations serves better to the fabrication of homogeneous patches, since homogeneity is only achieved when the actual experimental conditions like the repetition rate f_p and the ablation threshold I_{abl} are considered. Therefore, we have used ω_{eff} as reference for the calculation of φ_{line} throughout this paper.

3.5.2 *Homogeneous microstructures*

Two different microstructures have been found with correspondingly different morphologies (Figure 3.3). The first type consists of well-defined pillars of different geometries ranging from triangles, irregular squares and pentagons to circles (Figure 3.3a). Since the tops of these pillars are roundish, we named the features *pillow-like*. The second type shows similar geometries however these are less defined with more variety of shapes and sizes (Figure 3.3b). The spacing and feature sizes are less regular than for the pillow-like structures; therefore, we describe this second type of structures as *bumpy*. Figure 3.3c and d show lines that have been micromachined with the same $I_{pulse\text{-}accumulated}$ as the respective patches for pillow-like and bumpy structures. Interestingly, Figure 3.3c does not show any pillow-like structures, however bumpy structures are visible in Figure 3.3d. The average dimensions for the two types of microstructures identified above have been listed in Table 3.1 for three cases: close to the lower threshold of feature formation, homogeneous patches and close to the upper threshold of feature formation.

Table 3.1: Average dimensions of microstructures.

Average diameter (and STDEV) [µm]	**At lower threshold**	**For homogeneous patch**	**At upper threshold**
Pillow-like	15.4 (5.39)	11.6 (0.39)	11.6 (3.50)
Bumpy	5.8 (1.84)	8.1 (3.50)	8.3 (8.31)

Pillow-like structures evolved beginning at the lower threshold from large dimensions with high variation of the diameter to smaller dimension with less variation once a homogeneous patch had been achieved. Towards the upper threshold the feature size remained constant, while the variability increased again. The variability was larger for bumpy structures in the case of a homogeneous patch and close to the upper threshold. However, the average dimensions of both structures did not differ significantly from one another except close to the lower threshold.

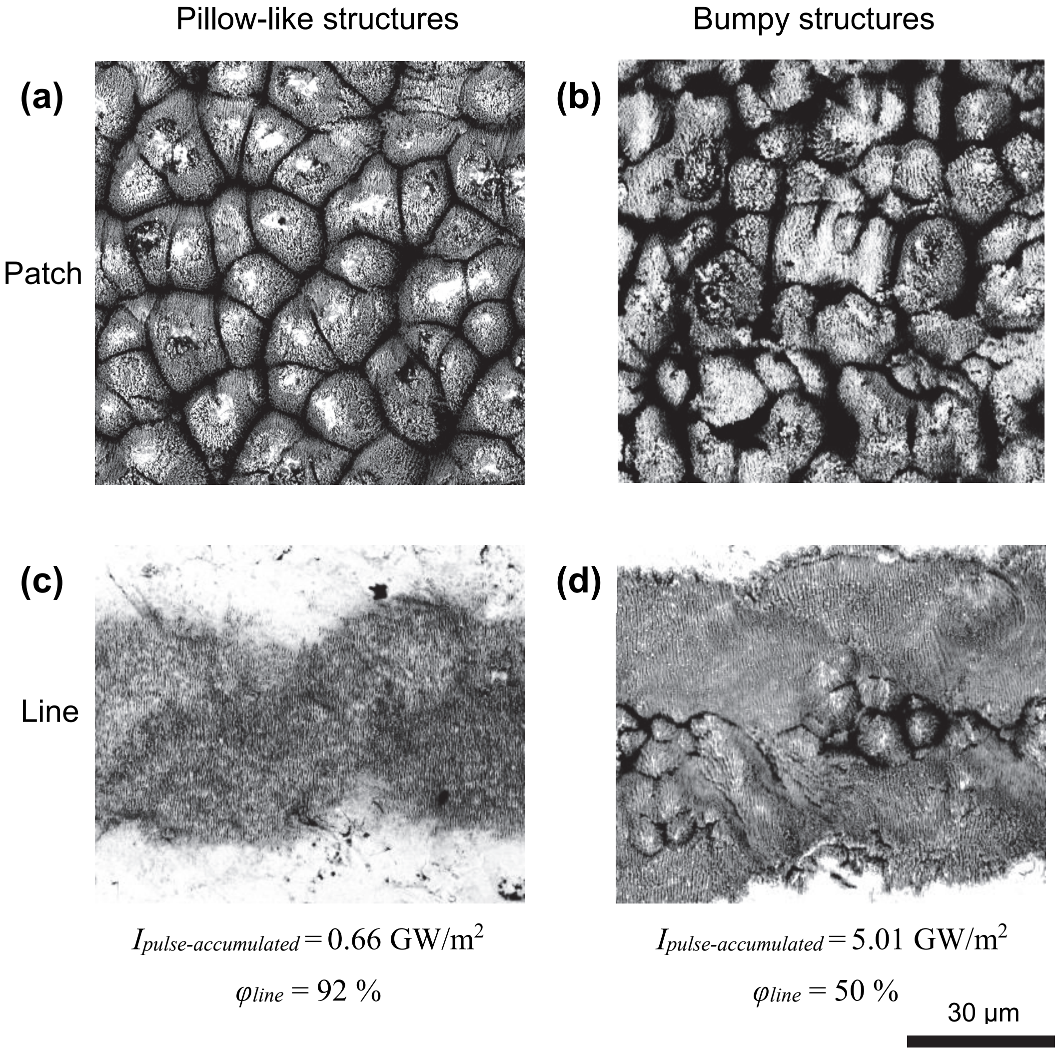

Figure 3.3: Patches and lines of homogeneous *pillow-like* and *bumpy* microstructures.

Figure 3.4a illustrates the different combinations of the intensity $I_{pulse\text{-}accumulated}$ and the overlap φ_{line} that led to the formation of the pillow-like or the bumpy microstructures. The figure shows clearly that the two types of microstructures have been found at totally different combinations of $I_{pulse\text{-}accumulated}$ and φ_{line}.

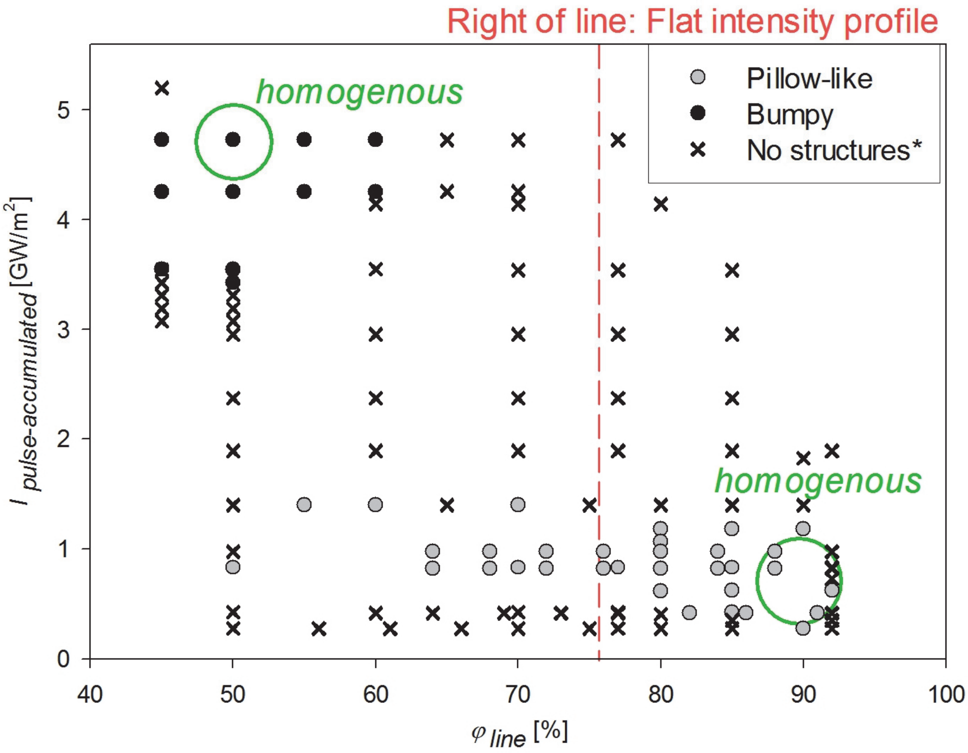

Figure 3.4: Combinations of φ_{line} and $I_{pulse\text{-}accumulated}$ that result in *pillow-like* and *bumpy* microstructures. (*No pillow-like or bumpy structures).

Pillow-like structures are located in an interval of $I_{pulse\text{-}accumulated}$ between 0.30 and 1.40 GW/m^2 and a wide range of φ_{line} of 50 to 95 %. However, the occurrence of homogeneous pillow-like structures (indicated with a circle in Figure 3.4) is limited to relatively high values of φ_{line} between 85 and 95 %. Bumpy structures are produced with higher values of $I_{pulse\text{-}accumulated}$ of 3.30 and 5.20 GW/m^2 but only in a narrow range of φ_{line} between 45 % and 65 %. For bumpy structures the overlap range to obtain homogeneous structures is less than 10 percentage points around a value of φ_{line} of 50 %. The variation of $I_{pulse\text{-}accumulated}$ and φ_{line} between the thresholds also led to different intermediate topologies. However, none of these showed any regular pattern that resulted in a homogeneous patch. The combinations of $I_{pulse\text{-}accumulated}$ and φ_{line} result in different levels of $I_{line\text{-}accumulated}$ calculated with Eq. (3.6) and displayed on the *z*-axis in Figure 3.5. $I_{line\text{-}accumulated}$ increases exponentially with increasing φ_{line} between 45 % and 95 %. While pillow-like structures have been found for low and high levels of $I_{line\text{-}accumulated}$, bumpy structures are only found at $I_{line\text{-}accumulated}$ above 23.6 GW/m^2. Above $I_{line\text{-}accumulated}$ = 56.6 GW/m^2 neither pillow-like nor bumpy structures have been produced.

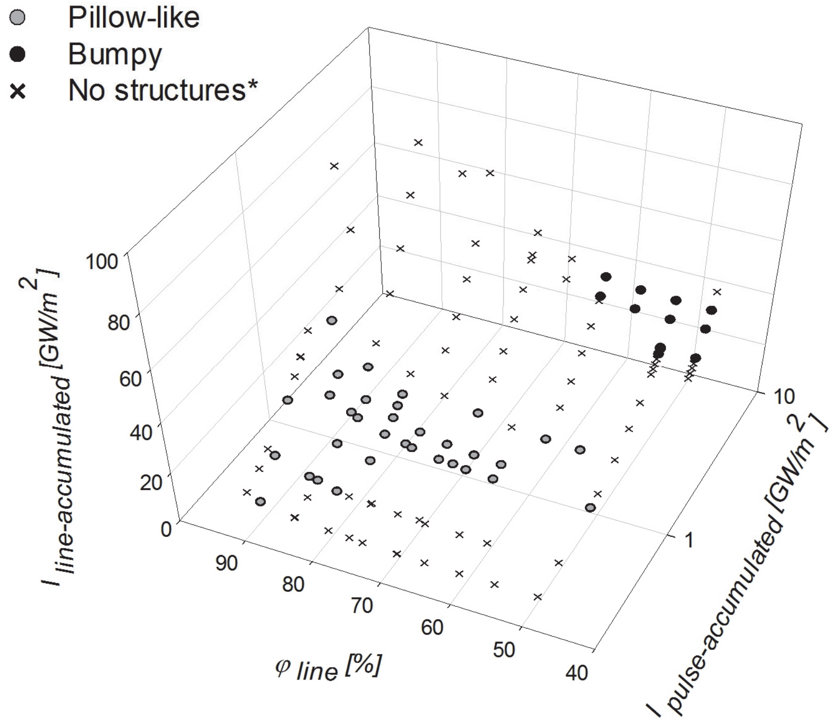

Figure 3.5: Areas for the formation of *pillow-like* and *bumpy* microstructures as combination of overlap φ_{line}, $I_{pulse\text{-}accumulated}$ and the resulting $I_{line\text{-}accumulated}$. (*No pillow-like or bumpy structures)**.**

The intensity profiles for homogeneous structures have been simulated in Figure 3.6. $I_{line\text{-}accumulated}$ is the resulting maximum intensity level, indicated by the dotted line. While homogeneous pillow-like structures occur only at a flat intensity profile (Figure 3.6a), homogeneous bumpy structures are formed from wavy intensity profiles (Figure 3.6b). Interestingly, the resulting values of 26.4 GW/m^2 for $I_{line\text{-}accumulated}$ for homogeneous pillow-like structures are similar to the minimum of the accumulated intensity profile of homogeneous bumpy structures at 23.6 GW/m^2.

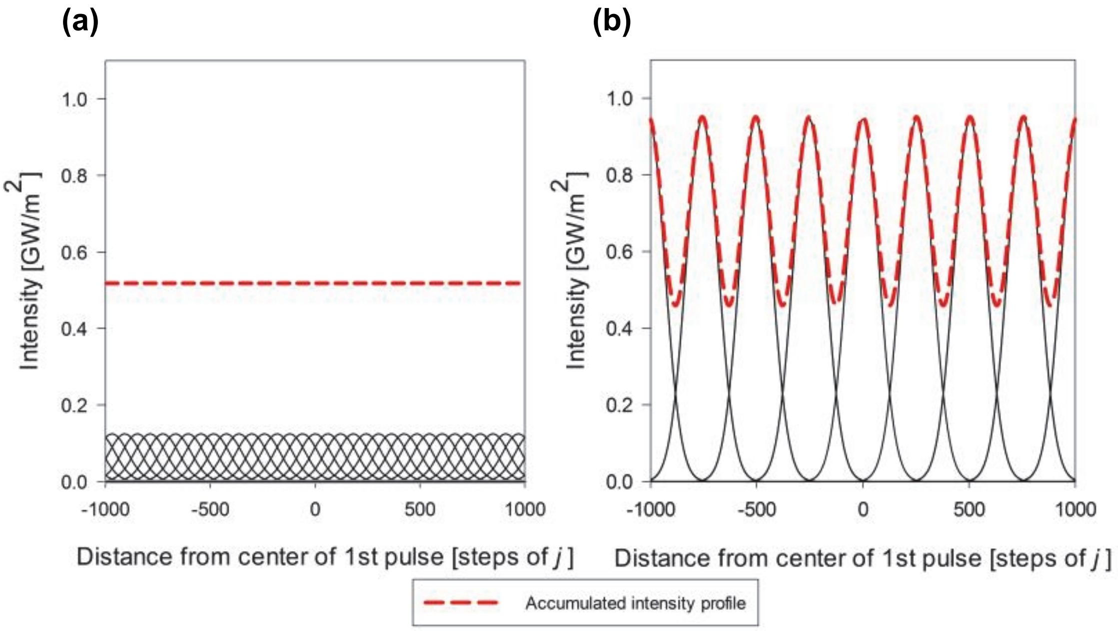

Figure 3.6: Intensity profiles for homogeneous patches of *pillow-like* (a) and *bumpy* (b) structures.

3.5.3 Initial feature formation and patch development

The borders of the zones where pillow-like and bumpy structures are formed can be defined by the threshold values listed in Table 3.2.

Table 3.2: Intensity thresholds for pillow-like and bumpy structures.

	Pillow-like		**Bumpy**	
	$I_{pulse\text{-}acc.}$ **(GW/m^2)**	$I_{line\text{-}acc.}$ **(GW/m^2)**	$I_{pulse\text{-}acc.}$ **(GW/m^2)**	$I_{line\text{-}acc.}$ **(GW/m^2)**
Lower threshold	0.29	4.5 to 18	3.56	25 to 40
Upper threshold	1.51	10 to 55	5.51	32 to 56
Total range	1.20	50.5	3.00	20

The lower threshold indicates the onset of microstructure formation. A threshold event has been defined as the occurrence of at least one feature of the pillow-like or bumpy pattern on the SEM image of the surface. The upper threshold has been identified qualitatively when the SEM images have shown less microstructure coverage than overexposed areas on a patch (see Appendix A).

The thresholds are quantified with the line intensity $I_{pulse\text{-}accumulated}$ and the accumulated intensity $I_{line\text{-}accumulated}$ to account for the fact that thresholds are different for lines and for patches (Figure 3.3). $I_{line\text{-}accumulated}$ thresholds are given as ranges, since $I_{line\text{-}accumulated}$ varies for the same $I_{pulse\text{-}accumulated}$ but with different φ_{line}. It can be seen in Table 3.2 that the lower thresholds for both types of microstructures are clearly different by a factor 5 ($I_{line\text{-}accumulated}$) to 10 ($I_{pulse\text{-}accumulated}$). However, the upper thresholds in particular expressed with $I_{line\text{-}accumulated}$ for both types of structures are similar. An interesting phenomenon was observed for the pillow-like structures illustrated in Figure 3.7.

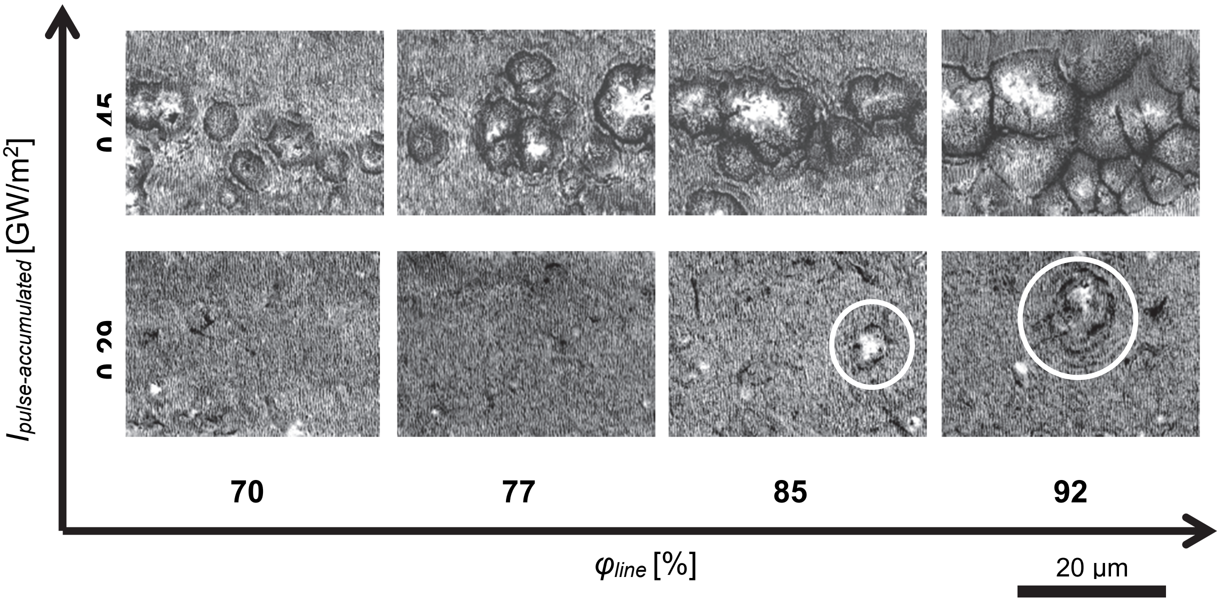

Figure 3.7: Approach of lower threshold for *pillow-like* structures with $I_{pulse\text{-}accumulated}$ and φ_{line}.

At constant φ_{line} of 70 % the increase of $I_{pulse\text{-}accumulated}$ from 0.27 to 0.43 GW/m^2 triggers the production of pillow-like microstructures. When φ_{line} was further increased from 77 % to 92 % with 0.43 GW/m^2 a homogeneous patch was obtained. While the increase of φ_{line} from 70 % to 92 % at constant $I_{pulse\text{-}accumulated}$ of 0.27 GW/m^2 also promoted the formation of pillow-like structures, a homogeneous patch was never produced. Correspondingly, Figure 3.7 illustrates that both with an increase of $I_{pulse\text{-}accumulated}$ and φ_{line} non-homogeneous pillow-like structures can be produced. The formation of a homogeneous patch, however, required sufficiently high $I_{pulse\text{-}accumulated}$, as illustrated previously in Figure 3.4.

Furthermore, Figure 3.8 illustrates that another phenomenon is relevant for the formation of bumpy structures. At high $I_{pulse\text{-}accumulated}$ of 4 GW/m^2 and above, the increase of φ_{line} has a strong effect on the surface topology and an additional phenomenon has been observed: bumpy microstructures that have been formed at φ_{line} of 50 % do not occur when more lines overlapped in a set of overlapping lines at higher φ_{line} (Figure 3.8a and c). The surface topologies are completely different:

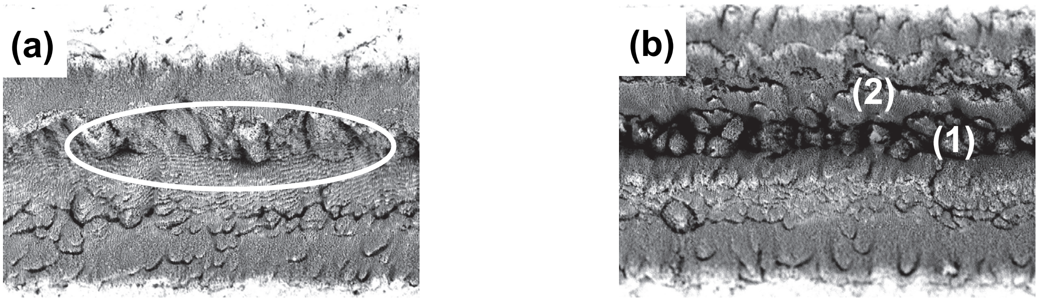

φ_{line} = 50 % (2 lines), $I_{pulse\text{-}tacc.}$ ($I_{tline\text{-}acc.}$) = 5.01 (50.5) GW/m^2

φ_{line} = 70 % (3 lines), $I_{pulse\text{-}acc.}$ ($I_{line\text{-}acc.}$) = 5.01 (63.2) GW/m^2

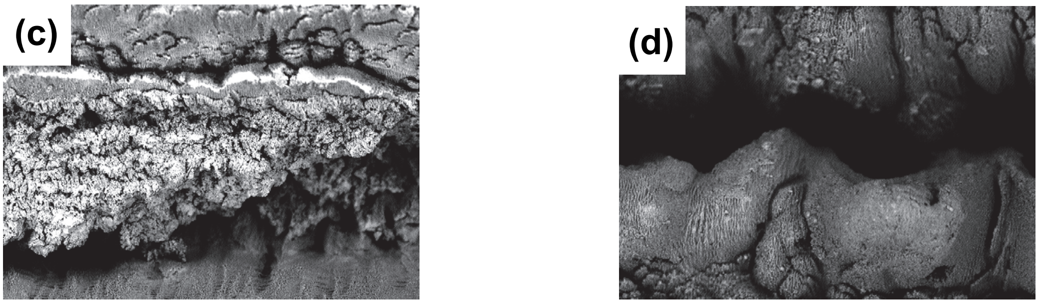

φ_{line} = 92 % (13 lines), $I_{pulse\text{-}tacc.}$ ($I_{line\text{-}acc.}$) = 5.01 (233.2) GW/m^2

φ_{line} = 0 % (0 lines), $I_{pulse\text{-}acc.} = I_{line\text{-}acc.}$ = 50.5 GW/m^2

Figure 3.8: Results from overlapping lines at high $I_{pulse\text{-}accumulated}$. ω_{eff} was 46.8 µm for (a) – (c) and 68 µm for (d).

While a patch is built up, microstructures that are visible at the advancing front (1) of Figure 3.8b will not occur on the final patch, which will look like zone (2). We named this phenomenon *overwriting*. Figure 3.8d shows a line that has been produced with $I_{pulse\text{-}accumulated}$ of 47.6 GW/m^2 to demonstrate that the same $I_{line\text{-}accumulated}$ as what was used for Fig 7a has a very different influence on the surface topology for a patch than it has for a single line.

3.6 Discussion

3.6.1 *Ablation regimes for microstructure formation*

The respective ranges between the lower and upper thresholds for pillow-like and bumpy structures (Table 3.2) are characteristic for each of the surface structures and allow discrimination between them (Bonse, Baudach et al. 2002, Eichstädt, Römer et al. 2013). The topology of the two microstructures originates at least partially from ablation, since particles have been produced during micromachining. The observation of two different microstructures at very different combinations of the line intensity $I_{pulse\text{-}accumulated}$ and the line overlap φ_{line} can be explained with the existence of two different *ablation regimes*.

Ablation regimes are determined by the intensity levels that are applied during the micromachining process (Le Harzic, Breitling et al. 2005, Hwang, Grigoropoulos et al. 2006). Therefore, for increasing intensity levels different material properties become relevant: at low levels the ablation correlates with the optical absorption coefficient of the material. However, at high levels the thermal absorption and conductivity coefficients are relevant, since thermal effects dominate the ablation process (Nolte, Momma et al. 1997). Two main ablation regimes are possible with fs – laser micromachining: non-thermal non-equilibrium ablation based on electrostatic Coulomb explosion (Cheng, Perrie et al. 2009, Gamaly 2011) and thermal ablation with phase explosion (Liu, Yen et al. 1979, Breitling, Ruf et al. 2004). For the latter, a train of successive pulses at high intensity is required (Miotello and Kelly 1999, Gamaly 2011). As a result, a range of 0.001 to 0.1 GW/m^2 was identified, where phase explosion becomes the dominant ablation mechanism as soon as the critical temperature of the metal is reached (Yang, Zhao et al. 2007).

In our experiments, the constant repetition rate f_p of 10 kHz with 300 PPS and the range of $I_{pulse\text{-}accumulated}$ from 0.5 to 5 GW/m^2, where pillow-like and bumpy structures are formed, fulfill the requirements for thermal ablation, which have been reported in the two studies discussed above. Therefore, the target surface must have been in a molten state at some point during the micromachining process. While we can conclude that thermal ablation regimes must be responsible for the occurrence of pillow-like and bumpy structures, the difference between the two morphologies is not as easily explained. However, the ranges for $I_{pulse\text{-}accumulated}$ as well as φ_{line} are quite different for both types of structures. This allows us to hypothesise that they are the determining parameters. A possible approach towards the understanding of their contribution is to consider the timescales of the energy input and the response of the target material.

Two situations of laser-material interactions are possible within an ablation regime that allows a molten surface: a subsequent laser pulse or a line either interacts with a surface that is currently in a molten state or it interacts with a surface that has previously been in a molten state. Material properties, in our case thermal properties like heat conductivity, differ for the liquid compared to the re-crystallized material (Cheng, Perrie et al. 2009). Consequently, the same energy input has a different effect on the surface morphology and the production of different kinds of surface features becomes possible, for instance pillow-like and bumpy structures.

The repetition rate f_p = 10 kHz used in our work results in pulse spacing of 100 µs, while the liquid phase exists up to 300 µs in the case of titanium (Semmar, Tebib et al. 2009). Thus, consecutive pulses of the pulse-train interact with a melted surface. However, this is only valid for the machining of a single line from consecutive pulses. For overlapping lines with φ_{line} the timescale of the repeated exposure exceeded several seconds in our experiments. Consequently, a beam scanning the subsequent line was not interacting with a molten surface anymore but with re-solidified material. Furthermore, in the case of the bumpy structures, a φ_{line} of 50 % means that half of the new line was machined on previously molten area and the other half on virgin material. However, in the case of pillow-like structures, at φ_{line} values of 80 % and above, the subsequent lines are machined almost completely on previously molten areas. This could explain why bumpy structures appear to be less regular. Also of relevance is that the single line for pillow-like structures does not show any microstructures (Figure 3.2c), while on the line for bumpy structures (Figure 3.2d) microstructures are visible. Clearly, the patches for both cases have a different morphology than the lines. Therefore, we suggest that the determining interaction regime must occur during the over-scanning step.

3.6.2 Parameter dependence of structure related thresholds

The boundaries between the regions for pillow-like and bumpy structures identified in Figure 3.3are linked to the structure-related thresholds listed in Table 3.2. These thresholds are specific for patches and are different for lines. Since the intensity $I_{pulse\text{-}accumulated}$ was identical when machining a line or a patch in our experiments, the overlap φ_{line} must be the parameter, which determined the threshold of a patch.

We have seen that for pillow-like structures, the lower threshold can either be reached by increasing $I_{pulse\text{-}accumulated}$ or φ_{line}, even when $I_{pulse\text{-}accumulated}$ was below the level of the lower threshold for a single line (Figure 3.7). As a result, the lower threshold of pillow-like structures can be considered to be dependent on φ_{line}. We compare this observation with a similar phenomenon known as the *accumulation effect* that has been reported for both static and moving beam (Jee, Becker et al. 1988, Güdde, Hohlfeld et al. 1998, Mannion, Magee et al. 2004). Consequently, the ablation threshold is parameter-dependent and decreases with increasing number of pulses (PPS). Since φ_{line} and PPS are related parameters, we can assume a similar relationship between φ_{line} and the lower threshold for pillow-like structures. We cannot make the same statement for the lower threshold for bumpy structures since they occur only at low φ_{line}, so that a patch receives twice as many PPS as a single line.

The upper thresholds for both types of structures are not parameter-dependent. Once $I_{pulse\text{-}accumulated}$ reaches the threshold intensity, no features are produced anymore. Overlap φ_{line} only plays a role in overwriting as shown in Figure 3.8. Consequently, φ_{line} determines where the overwriting occurs by increasing $I_{line\text{-}accumulated}$ above the threshold level. The intensity level, where the upper threshold is reached, remains unaffected by φ_{line}.

Finally, $I_{line\text{-}accumulated}$ alone cannot be used as to quantify thresholds but must be reported together with the respective $I_{pulse\text{-}accumulated}$ and φ_{line}. The upper threshold expressed in $I_{line\text{-}accumulated}$ is similar for both types of structures (Figure 3.5). However, the effect of a certain amount of intensity is different when a surface is exposed to the full amount at once, rather than stepwise during the scanning of overlapping lines (Figure 3.8d). Thus, the way intensity is delivered to the surface determines its resulting morphology more explicitly than the total amount does.

3.6.3 Feature dimensions and homogeneity

Homogeneity and the average feature dimension are linked for pillow-like microstructures. Both are determined by line intensity $I_{pulse\text{-}accumulated}$ and overlap φ_{line}. Figure 3.7 and Table 3.1 show that feature size of pillow-like structures increase with $I_{pulse\text{-}accumulated}$ and φ_{line}. The correlation between average feature size and $I_{pulse\text{-}accumulated}$ fits with the reported results from the literature (Bonse, Baudach et al. 2002, Groenendijk and Meijer 2006, Cheng, Perrie et al. 2009). However, the circumstance that pillow-like structures evolve to larger dimensions with increasing φ_{line} at constant $I_{pulse\text{-}accumulated}$ might also originate from the existence of different ablation regimes on previously melted material as discussed in Chapter 3.6.1.

The extent of the average dimensions for a homogeneous fully covered patch is limited by the available space for the intensity-driven growth of the features for different combinations of $I_{pulse\text{-}accumulated}$ or φ_{line}. At higher φ_{line}, once a patch gets fully filled with pillow-like structures their size is constant, however larger and less features appear on the same area when either $I_{pulse\text{-}accumulated}$ or φ_{line} are further increased (see Appendix A). This explains the increase of variability towards the upper threshold, and also why homogeneous pillow-like structures were only obtained at a certain range of combinations of $I_{pulse\text{-}accumulated}$ and φ_{line}. Consequently, to achieve homogeneity, a compromise must be made regarding the desired feature dimensions.

The progression of feature dimensions for bumpy structures between the thresholds correlates with the increase of $I_{pulse\text{-}accumulated}$, as expected from the literature. The occurrence of bumpy structures only in a small range of φ_{line} at high $I_{pulse\text{-}accumulated}$ is explained as follows: even the tails of the Gaussian beam have relatively high intensity levels, so that small adjustments of φ_{line} increase the energy input into the target surface significantly and the upper threshold is passed, where no clear features can be obtained anymore. As a result, φ_{line} is only of limited use to improve homogeneity or control the feature dimensions.

The simulation of the intensity profiles has shown that homogeneous structures can be obtained independently of the shape of the intensity profile. However, we attribute the larger variation of the feature dimensions of the bumpy structures to the wavy intensity profile, since the energy exposure of the surface is not equal across the patch. In the case of the pillow-like structures, the intensity profile is flat for a homogeneous patch. Figure 3.4 however, shows that the border between the wavy profile and the flat profile is located at a lower φ_{line} than what is required to obtain homogeneous pillow-like structures.

3.7 Conclusions

The role of line intensity $I_{pulse\text{-}accumulated}$ and line overlap φ_{line} on the formation of two different types of microstructures on titanium micromachined in air has been described. Two types of structures, pillow-like and bumpy, have been produced at totally different combinations of $I_{pulse\text{-}accumulated}$ and φ_{line}. Their occurrence has been attributed to two different thermal ablation regimes. Pillow-like structures are more regular and their homogeneity and feature dimensions can be controlled more easily. Micromachining with overlapping Gaussian beams requires a particular combination of $I_{pulse\text{-}accumulated}$ and φ_{line} to obtain homogeneous structures. Therefore, overlap should be calculated based on the effective beam diameter ω_{eff}. The control of the spatial and temporal flux of laser energy is crucial to obtain the desired surface topology: adjusting only the total energy is insufficient. Therefore, instead of the accumulated intensity $I_{line\text{-}accumulated}$, the underlying values of $I_{pulse\text{-}accumulated}$ and φ_{line} should be communicated to allow the reproduction of results from different experimental setups. This is of particular importance for structure-related threshold values because they are partially parameter dependent.

We have successfully linked simulated intensity profiles for overlapping Gaussian beams to the homogeneity of patches. Even though in our case a flat intensity profile could not be demonstrated to be a necessary condition for homogeneous structures, we consider simulations as a useful tool to quantify the actual local energy input and to attribute it to the resulting microstructures.

Acknowledgment

This research has been supported by the National Science and Engineering Research Council of Canada (NSERC). We thank the Plasma Processing Laboratory for the possibility to use its characterization infrastructure.

References

Please refer to the global bibliography at the end of the thesis.

Chapter 4

4. The influence of the gas environment on morphology and chemical composition of surfaces micromachined with a femtosecond laser

4.1 Preface

This chapter presents an article that has been published in the journal *Applied Surface Science*. The complete citation of the published article is:

Lehr, J., et al., The influence of the gas environment on morphology and chemical composition of surfaces micromachined with a femtosecond laser. Applied Surface Science, 2014. 320(0): p. 455-465.

During the course of investigating the influence of the environment on the chemical composition of femtosecond laser micromachined surfaces, preliminary experiments to this paper had shown that the gas environment during laser micromachining also influences the surface topology: Keeping all other machining parameters constant, only changing the gas environment led to a different surface topology. In particular, the settings determined for the two types of surface structures pillow-like and bumpy in air (see chapter 3) did not deliver the same structures when the environment was changed to pure oxygen, nitrogen or helium. This phenomenon was investigated in detail in this chapter 4 to understand the role of the gas environment and to attribute the micromachining results to the physical properties of the gas.

Three different interaction mechanisms between the laser beam and the environment during machining are known to be possible in an experimental setup as used in this study: The laser beam can interact with the gas environment itself (Chiron, Lamouroux et al. 1999, Martirosyan, Altucci et al. 2004, Gamaly 2011) and with the cloud of particles that is formed during ablation (Burghardt, Scheede et al. 1999, Zhigilei 2003, Grojo, Hermann et al. 2005). The third interaction mechanism between the laser beam and the ablation plasma is often considered irrelevant because of the corresponding time scales (Leitz, Redlingshöfer et al. 2011). However, researchers have found that pre-pulses can initiate a micro-plasma that interacts with the subsequent main pulse (Mao, Chan et al. 1993).

The interaction between the laser beam and the gas environment can be considered irrelevant since the required intensities to cause self-focussing according to the Kerr effect were not reached in this study (Gamaly 2011). Since the experimental setup did not permit direct measurements, the relevant time scales of the energy input and the formation of plasma and particles had to be considered to develop a hypothesis that would serve to explain which of the remaining two interaction mechanisms was ultimately responsible for the observed dependence of the surface topology on the gas environment (chapter 4.4).

The energy input to the surface results from the pulse duration of ~100 fs and the pulse spacing of approximately 100 µs. The invisible initial micro-plasma (Chen and Mao 2008) originating from the pre-pulse lasts throughout the duration of the pulse and in the case of helium is dense enough to cause significant absorption of the laser energy so that the effective intensity I_{eff} is lower in helium compared to the same in the oxygen and nitrogen environment, where the micro-plasma is expected to be of considerably lower density (Batani, Jafer et al. 2010, Miloshevsky, 2014 #1670). Hence, the observed difference between I_{eff} in the case of bumpy structures between oxygen, nitrogen, and helium (chapter 4.4) is not solely explainable with the properties of the particle cloud (as stated chapter 4.5) but most likely rather driven by the plasma properties.

However, this effect seems to become relevant only at high intensities ($I_{pulse\text{-}accumulated} > 30$ GW/m^2) since the dependence of the resulting surface topology on the gas environment was only visible at intensities necessary to obtain bumpy structures.

While the state of the micro-plasma serves to explain the results obtained for bumpy structures in helium, the clear difference between I_{eff} for bumpy structures between oxygen and nitrogen cannot be explained with plasma interactions since the relevant physical properties of the two gases that determine the plasma density (see table 4.5 in chapter 4.5), in particular the sonic speeds (0_2 = 316 m/s vs. N_2 = 353 m/s), are alike. Hence, the physical properties of the produced particles seem to determine the resulting topology when machined in oxygen and nitrogen.

Particles are produced at the end of the laser pulse after a few µs when the expanding plasma cools down and the expansion velocity has decreased to the velocity of sound (Miloshevsky, Harilal et al. 2014). Even though the particles are produced before the subsequent pulse reaches the target, interaction with the laser beam is limited due to the fact that the particles keep their momentum and are carried away from the surface (Glover 2003). Under the experimental conditions in this study the particles reached the walls of our reactor after 100 to 300 µs. However, after the experiments particles were found on the samples' surface so that it can be assumed that a significant share of the particles is not carried away from the surface. This strengthens our hypothesis that the chemical composition of the ablated particles is responsible for the observed differences (see chapter 4.5).

Furthermore, the term "incorporated" employed in the following text describing the detected TiN on the surface after micromachining might lead to confusion, as the detected TiN most was rather deposited on the surface than evenly distributed throughout the material matrix. Further research is required to investigate the morphology, chemical composition and physical depth of TiN.

The influence of the gas environment on morphology and chemical composition of surfaces micromachined with a femtosecond laser

Jorge Lehr[a], Fabrizio de Marchi[b], Luke Matus[a], Jennifer MacLeod[b], Federico Rosei[b,c], Anne-Marie Kietzig[a]
[a] *Department of Chemical Engineering, McGill University, 3610 University Street, H3A 0C5, Montreal, QC, Canada*
[b] *Institut National de la Recherche Scientifique, Centre Énergie, Materiaux, Telécommunications, 1650 Lionel Boulet Boulevard, J3X 1S2, Varennes, QC, Canada*
[c] *Center for Self-Assembled Chemical Structures, McGill University, H3A 2K6 Montreal, Quebec, Canada.*

Abstract

We investigated the influence of different gas environments on the fabrication of surfaces, homogeneously covered with equally sized and spaced microstructures. Two types of structures have been successfully micromachined with a femtosecond laser on titanium surfaces in various atmospheres. The surface chemistry of samples machined in oxygen and helium shows TiO_2, while machining in nitrogen leads to an additional share of TiN. The actual surface structure was found to vary significantly as a function of the gas environment. We found that the ablated particles and their surface triggered two consecutive events: The optical properties of the gas environment became non-isotropic which then led to the pulse intensity being redistributed throughout the cross section of the laser beam. Additionally, the effective intensity was further reduced for TiN surfaces due to TiN's high reflectivity. Thus, the settings for the applied raster-scanning machining method had to be adjusted for each gas environment to produce comparable structures. In contrast to previous studies, where only noble gases were found suitable to produce homogeneous patches, we obtained them in an oxygen environment.

4.2 Introduction

Femtosecond laser micromachining has been successfully introduced in industry in areas like accuracy drilling (Nedialkov, Atanasov et al. 2007) and cutting (Chien and Gupta 2005) of metals, dielectrics and polymers. The high precision achieved with femtosecond lasers originates primarily from the limited heat affected zone (HAZ), which is smaller compared to that of laser systems with longer pulse duration such as nano- or picoseconds (Paatsch, Kautek et al. 1999, Delaigue, Honninger et al. 2012). It has been shown that three main factors influence the outcome of laser micromachining: the dynamic and static energy input (Lehr and Kietzig 2014), the choice of target material and the surrounding environment (Cheng, Perrie et al. 2009). Since the choice of material is primarily determined by the application, only the energy input and the environmental conditions can be controlled to optimize the machining quality. It has been shown that the type of gas also contributes to the quality of micromachined surface structures (Ju and Longtin 2004, Nayak, Gupta et al. 2008, Demir, Previtali et al. 2013). The present work focuses on the particular case of femtosecond laser micromachined arrays (*patches*) covered with equally sized and spaced microstructures. These *homogeneous* patches have been obtained for two types of microstructures on titanium: *pillow–like* (Kietzig, Hatzikiriakos et al. 2009) and *bumpy* (Lehr and Kietzig 2014) structures. These structures have been chosen since similarly structured titanium surfaces have been found to enhance biocompatibility (Park, Kim et al. 2009, Matschegewski, Staehlke et al. 2010).

The production of homogeneous patches of microstructures requires a line-wise build-up (Cheng, Perrie et al. 2009, Romer, Huis in't Veld et al. 2009). In the case of a Gaussian beam the spatial intensity distribution of a pulse needs to be considered (an explanatory scheme can be found here (Lehr and Kietzig 2014)). Pulses that compose a machined line, as well as lines that compose a patch have to overlap to compensate for the Gaussian profile. The energy input is commonly quantified by the intensity that is directed towards a certain area of the target surface. This intensity is calculated from the peak intensity of the beam I_0, the scanning velocity v_0 and the repetition rate f_p considering the number of pulses that effectively overlap on a single spot. The duration of a pulse is calculated from f_p, and therefore includes not only the actual pulse length (in fs) but also the delay time between the pulses of the pulse-train. Consequently, all calculated intensity values represent an average value over the entire time span (Paschotta 2008). In the case of a scanned line, the intensity input on any particular spot (described by its x-position on the sample and the intensity level at a certain position i_x of the Gaussian beam) is calculated in Eq. (4.1) as the accumulated intensity of the number of pulses ($I_{pulse\text{-}accumulated}$) that overlap with φ_{pulse} [%].

$$I_{pulse-accumulated}(x, i_x) = I_0 exp\left(-2\left(\frac{\left(x + \frac{v_0}{f_p} i_x\right)^2}{\left(\frac{\omega}{2}\right)^2}\right)\right) \tag{4.1}$$

Since in the case of scanned lines the latter also overlaps with φ_{line} [%], the accumulated input intensity ($I_{line\text{-}accumulated}$) consequently adds up with the number of lines in Eq. (4.2). Here, the position on the sample is describes with the x- and z-coordinate and the intensity level with i_x and j_z (the detailed derivation of $I_{pulse\text{-}accumulated}$ and $I_{line\text{-}accumulated}$ can be found in Appendix B).

$$I_{line-accumulated}\,(x, z, i_x, j_z) = I_0 exp\left(-2\left(\frac{\left(x + \frac{v_0}{f_p} i_x\right)^2 + \left(z + \frac{v_0}{f_p} j_z\right)^2}{\left(\frac{\omega}{2}\right)^2}\right)\right) \tag{4.2}$$

The reference area for I_0, $I_{pulse\text{-}accumulated}$, $I_{line\text{-}accumulated}$, φ_{pulse} and φ_{line} is calculated from the theoretical beam diameter ω_{theo}, which depends solely on the physical properties of the laser beam and the optics along the beam patch. However, it has been shown that the formation of homogeneous patches can be precisely controlled only by using the effective line width ω_{eff} to calculate φ_{line} instead of ω_{theo} (Lehr and Kietzig 2014). Thereby, ω_{eff} equals the diameter of a laser irradiated line, which is visible on the target surface after micromachining. However, ω_{eff} does not necessarily correlate with the theoretical values of $I_{pulse\text{-}accumulated}$ or $I_{line\text{-}accumulated}$, but it represents the intensity that effectively impinges on the surface (I_{eff}) under the experimental conditions. Except in the case of micromachining in a complete vacuum, I_{eff} is always different from $I_{pulse\text{-}accumulated}$ and $I_{line\text{-}accumulated}$ (Sun and Longtin 2001).

There are different interaction regimes between the laser beam and the gas environment in three different zones (Figure 4.1) that determine the extent of I_{eff}. The interaction regimes have been studied for nano-(Chang, Warner et al. 1998, Burghardt, Scheede et al. 1999, Barthélemy, Margot et al. 2005, Henley, Carey et al. 2005) and picosecond lasers(Mao, Chan et al. 1993, Rae 1994, Zhigilei 2003) and more recent for femtosecond lasers(Chiron, Lamouroux et al. 1999, Mengqi and Grigoropoulos 2001, Sun and Longtin 2001, Margetic, Ban et al. 2003, Ju and Longtin 2004, Barthelemy, Margot et al. 2005, Grojo, Hermann et al. 2005, König, Nolte et al. 2005, Vujicic, Skenderovic et al. 2006, Vatsya and Nikumb 2007).

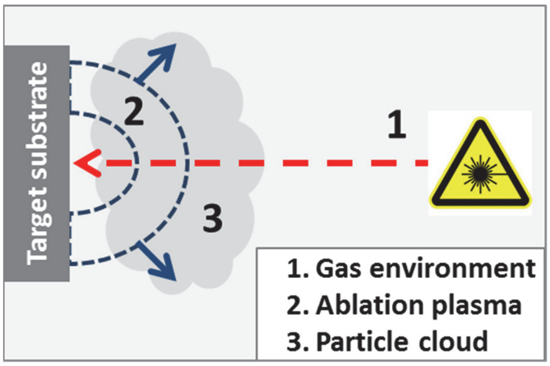

Figure 4.1: Laser beam interaction with gas environment, expanding ablation plasma plume and particle cloud.

Gas Environment: A laser beam pointing towards the target substrate interacts with the surrounding gas environment (see 1 in Figure 4.1). When the gas is ionized above the threshold of about 10^8 GW/m^2, opposing effects have to be considered (Chiron, Lamouroux et al. 1999, Martirosyan, Altucci et al. 2004, Gamaly 2011). The Kerr effect causes the refractive index n_r of the gas to increase with the laser beam intensity I_0 and the beam to self-focus, which increases I_{eff} on the target. As a result, the gas plasma density grows, subsequently causing the refractive index to decrease again (Sun and Longtin 2001, Ju and Longtin 2004). Plasma channels in the ionized gas increase I_{eff} further (Vujicic, Skenderovic et al. 2006).

Ablation Plasma: When laser pulses with energy levels higher than the ablation threshold I_{abl} reach the surface during the ablation process, plasma is generated, which ionizes the surface (see 2 in Figure 4.1). Once the plasma formed reaches high enough density, it adsorbs laser energy through *shielding* (Mao, Chan et al. 1993) and increases the surface temperature which promotes surface ablation (Chang, Warner et al. 1998).

Ablation Particles: Together with the ablation plume, a particle cloud is produced from condensing vapor (see 3 in Figure 4.1). Subsequently, the incoming laser pulses interact with the particles and I_{eff} decreases (Burghardt, Scheede et al. 1999, Zhigilei 2003, Grojo, Hermann et al. 2005).

Up to now, there have been very few publications about the micromachining of homogeneous surface structures on metals in a specific gas environment using a femtosecond laser (Perrie, Gill et al. 2004, Robinson and Jackson 2006, Nayak, Gupta et al. 2008). Robinson and Jackson compared air and nitrogen with argon and reported the most homogeneous patches on aluminum with argon. Nayak *et al.* investigated possible chemical reactions between the environment and the surface on titanium. They showed that the bi-directional shockwave which occurs during ablation enables the ablated reactive material to return to the surface and to subsequently become incorporated (Nayak, Gupta et al. 2008). In addition, it was demonstrated that the velocity of the shockwave depended on the sonic speed in the gas. Similarly, others have also found that the chemical composition of the surface after laser micromachining in a reactive gas was altered, and that the gas species was incorporated into the surface (Hencˇ-Bartolic´ 1995). In the case of machining titanium in nitrogen, the irradiated surface contained titanium nitride (Lima, Folio et al. 2005).

The goal of our investigation is to understand the role played by the machining gas environment in both the formation of a homogeneous patch and the alteration of the surface chemistry. To the best of our knowledge these two aspects of femtosecond laser micromachining have not yet been investigated together. The three variables studied in our experiments include: the gas environment, $I_{pulse\text{-}accumulated}$, and φ_{line} necessary to obtain patches. The control of surface morphology and surface chemistry is of particular importance in the context of surface wetting (Kietzig, Hatzikiriakos et al. 2009, Jiwhan, Jae-Hoon et al. 2010, Luo, Shum et al. 2010) and biocompatibility (Yahyapour, Eriksson et al. 2004, Zhang, Andrukhov et al. 2010). Further control of surface chemistry could lead to tailor-made surfaces with targeted levels of wettability in a one-step femtosecond laser machining process.

4.3 Materials and Methods

Titanium samples (99.9 % purity, McMaster-Carr, USA) were micromachined with a Coherent Libra femtosecond laser system with a wavelength of 800 nm, repetition rate of 10 kHz and pulse duration <100 fs. A half-wave plate and a polarizing beam splitter were used to attenuate the average laser output power of 4 W. The titanium sheets were polished to an average roughness r_{RMS}=180 nm and sonicated in acetone for 10 min before being attached to a computer-controlled x-z-translation stage which was located inside a sealed reactor vessel (Figure 4.2) with a volume of approximately 4.5 l to control the gas environment (6 mm thick silica glass window; refractive index n_r = 1.46).

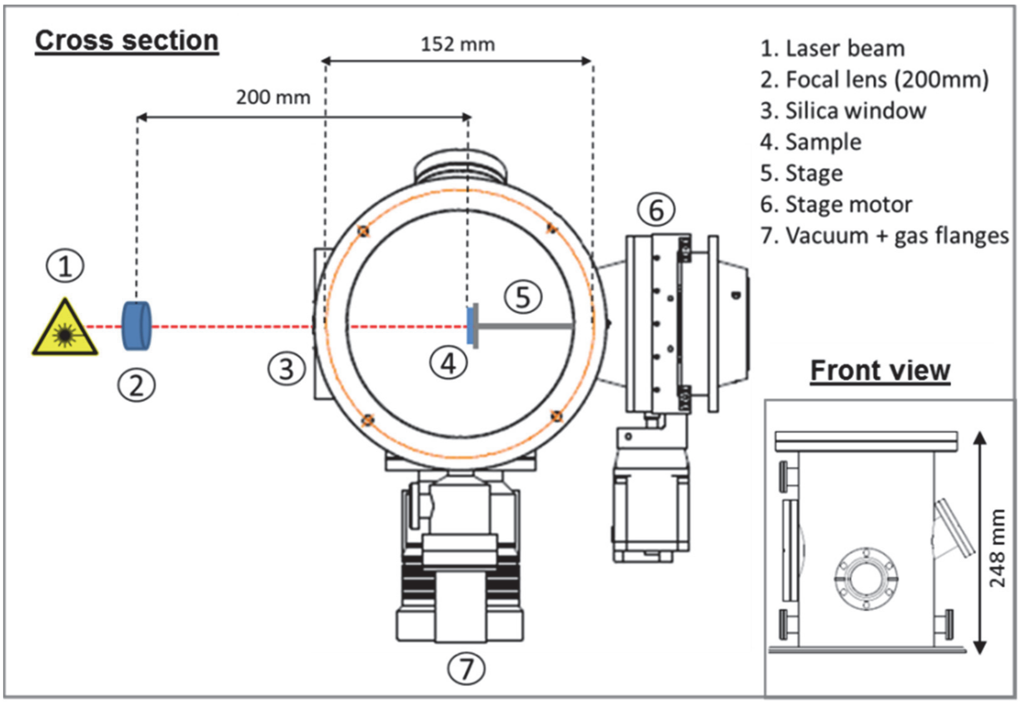

Figure 4.2: Reactor setup for micromachining in different gas environments.

The sample was located at the focus of a 200 mm focal lens. The beam diameter ($1/e^2$) entering the lens was 4.7 mm, measured with a home built CCD beam profiler (CCD: Point Grey, Canada).

The resulting theoretical beam diameter at focus ω_{theo} after entering the reactor through a silica window was 66 µm. Micromachining was conducted in helium, nitrogen and oxygen (99.999 % Praxair, Canada) at 450 Torr after evacuating the reactor vessel to 400 mTorr. The effective line width ω_{eff} was determined by line width experiments for a range of $I_{pulse\text{-}accumulated}$ values between 0.8 and 52.2 GW/m^2. The corresponding range of the single pulse peak intensity I_0 was 0.29 to 10.52 TW/m^2. Square patches were micromachined by raster scanning the sample under the beam. To achieve a specific overlap of the scanned lines φ_{line}, the displacement Δz of the translation stage was calculated based on ω_{eff}. The scanning velocity in the x-direction was held constant at $v_0 = 1.5$ mm/s for both line and patch experiments. The resulting overlap of the laser pulses in the x-direction φ_{pulse} was 99.7 %. Samples were kept inside the reactor for exposure with either the same or a different gas after micromachining. A vacuum (400mTorr) was pumped before refilling the vessel for exposure. The exposure time (the time the sample spent after machining inside the reactor) was 18 h at a pressure of 700 Torr and temperature at 60°C. After the experiments, the samples were sonicated for 10 min in acetone. During storage and transport the samples were kept in an evacuated stainless steel chamber. Images of the surface morphology were obtained with a Phenom™ FEI scanning electron microscope (SEM). Roughness values (r_{RMS}) were determined with an Asylum (USA) MFP-3D atomic force microscope, using Aspire CFM-10 probes on four different spots on the surface over an area of 90 by 90 µm. The chemical composition of the surface and ablated particles were analyzed with a Thermo Fisher (USA) VG Escalab 220i XL X-ray photoelectron spectroscope (XPS).

4.4 Results

4.4.1 Line width analysis

The line width ω_{eff} has been determined from SEM images (Figure 4.3 right) of single machined lines at different intensities $I_{pulse\text{-}accumulated}$ in all three gases. The squared line width ω_{eff}^2 increases logarithmically with $I_{pulse\text{-}accumulated}$ (Figure 4.2 left), consistently with the literature (Uppal and Shiakolas 2008, Cheng, Perrie et al. 2009).

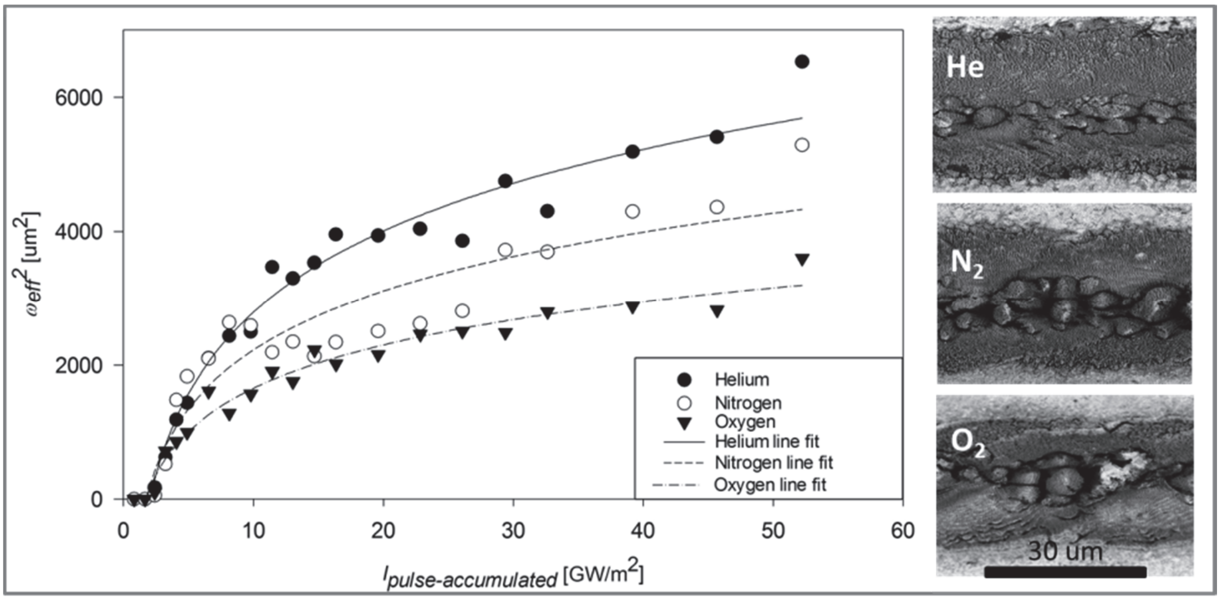

Figure 4.3: Left: Micromachined lines in oxygen, nitrogen and helium at 450 Torr. Each data point represents 3 measurements (error bars are not shown to maintain clarity of figure). Right: SEMs of lines at $I_{pulse\text{-}accumulated}$ of 39.2 GW/m^2.

The largest ω_{eff} was obtained for lines in helium, whereas in nitrogen and oxygen ω_{eff} was smaller. Figure 4.3 further shows the regression fit modeled according to (Eq. (4.3)).

$$\omega_{eff}{}^2 = \beta_1 \ln\left(I_{pulse-accumulated}\right) + \beta_0 \tag{4.3}$$

Table 4.1 summarizes the regression results with different values for β_0 and β_1 for each gas. The fitting quality R^2 is high for oxygen and helium, while it is smaller for nitrogen. This can be attributed to a change in the trend of the ω_{eff} data for nitrogen at 30 GW/m^2.

Table 4.1: Regression results for beam diameter (ω_{model}) and ablation threshold (I_{abl}) for each gas.

	Oxygen	**Nitrogen**	**Helium**
$\boldsymbol{\beta_1}$	933.03	1272.07	1754.30
$\boldsymbol{\beta_0}$	-496.10	-704.31	1250.30
$\boldsymbol{R^2}$	0.97	0.88	0.97
$\boldsymbol{\omega_{model}}$ **[um]**	43.2	50.4	59.2
$\boldsymbol{I_{abl}}$ **[GW/m^2]**	1.70	1.74	2.04

The results from the regression analysis were linked to a model (Eq. (4.4)) developed by Liu, which is known as *D^2-model* (Liu 1982). This model, which can also be applied in multi-pulse experiments (Uppal and Shiakolas 2008), relates the square of the effective line width ω_{eff}^2 and the logarithm of the applied peak intensity (I_0). When machining a line instead of a single spot, $I_{pulse\text{-}accumulated}$ needs to be used instead of I_0 to adapt Liu's model to the case of a scanned line.

$$\omega_{eff}{}^2 = 2\left(\frac{\omega_{model}}{2}\right)^2 \left(ln\left(I_{pulse-accumulated}\right) - ln(I_{abl})\right) \tag{4.4}$$

In Eq. (4.4) ω_{model} is the theoretical diameter of the beam. However, as we will show later, it is different from ω_{theo}. Similar to the approach taken by Uppal *et al.*, the regression coefficients β_0 and β_1 have been used together with Eq. (4.4) to derive the ablation threshold intensity I_{abl} (Eq. (4.5)) and the beam diameter ω_{model} (Eq. (4.6)).

$$\beta_0 = -2\left(\frac{\omega_{model}}{2}\right)^2 ln(I_{abl}) \;\; and \;\; I_{abl} = e^{\left(\frac{-2\beta_0}{\omega_{model}{}^2}\right)} = e^{\left(-\frac{\beta_0}{\beta_1}\right)} \tag{4.5}$$

$$\beta_1 = 2\left(\frac{\omega_{model}}{2}\right)^2 \text{ and } \omega_{model} = \sqrt{(2\,\beta_1)} \tag{4.6}$$

The calculated threshold intensity I_{abl} and ω_{model} were different for each gas, lowest for oxygen and highest for helium (Table 4.1).

4.4.2 *Surface topology*

The effective line width ω_{eff} was used to calculate the overlap φ_{line} to micromachine patches. Pillow-like (Figure 4.3a, c, d and e) and bumpy (Figure 4.4g - i) structures have been produced, similarly to what was found in previous experiments in air (Lehr and Kietzig 2014).

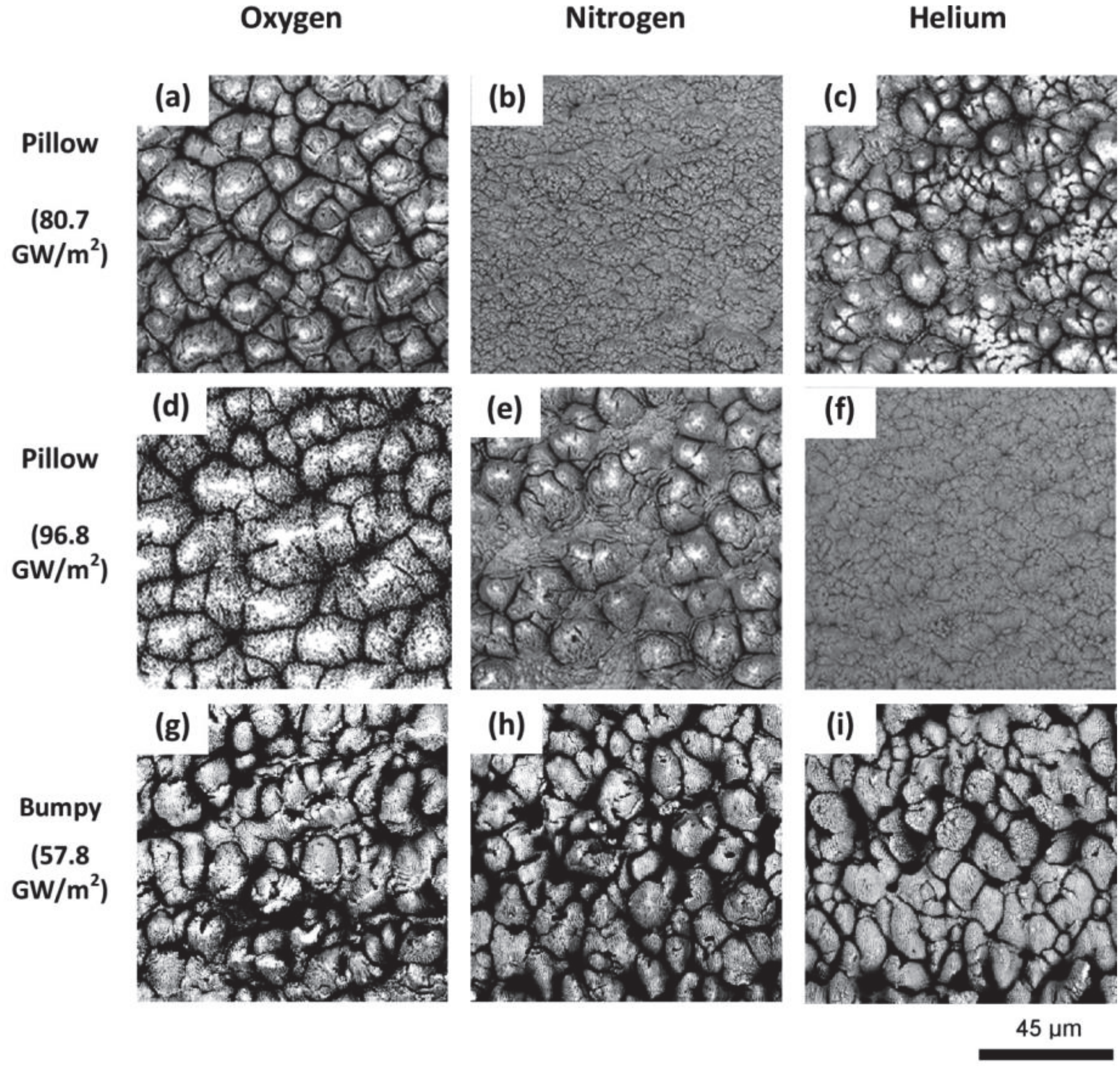

Figure 4.4: SEMs of pillow-like and bumpy structures at the same $I_{line\text{-}accumulated}$ with φ_{line} being varied.

The resulting surface morphology clearly differs between the gases for pillow-like structures (Figure 4.4a - f). Homogeneous patches completely covered with pillow-like structures have only been obtained in oxygen (Figure 4.4a). The “best” (= most homogeneous) patches of pillow-like structures in helium were produced (Figure 4.4c) with similar settings as for machining in oxygen. In a nitrogen atmosphere, the “best” patches were achieved at higher $I_{pulse-accumulated}$ than in oxygen and helium, as shown in Figure 4.4e. The structures found in Figure 4.4b for nitrogen and Figure 4.4f for helium were not classified as pillow-like since their morphology is clearly different from the structures on the other SEM images (Figure 4.4a,c-e). This kind of intermediate structure occurred in our experiments only in helium and nitrogen either close to the lower or above the upper threshold for pillow-like structures. However, these structures were reported previously on other materials and have been classified as micro-ripples (Bizi-Bandoki, Benayoun et al. 2011, Bizi-Bandoki, Valette et al. 2013).

Apart from the coverage of the patches, the dimensions of the microstructures have also been determined. Pillow-like and bumpy structures have similar dimensions in the order of 10 μm. However, the size distribution is narrower for pillow-like structures, as seen from the standard deviation. The average roughness values are in the order of a few micrometers for both types of structures. However, the variation of the roughness within a patch is smaller for pillow-like structures than for bumpy structures.

Table 4.2: Geometrical dimensions, roughness r_{RMS} and ablation rate of pillow-like and bumpy structures. Average diameters were measured on SEM images. Roughness values were obtained by AFM. The ablation rate was determined for the same accumulated intensity for each type of structure by measuring the weight of the sample before and after micromachining.

	Pillow-like structures			**Bumpy structures**		
	Oxygen	Nitrogen	Helium	Oxygen	Nitrogen	Helium
Average diameter [µm]	12.3	11.1	7.8	11.0	10.8	10.1
Standard deviation [µm]	4.2	3.2	3.2	6.9	5.3	6.1
RMS roughness [µm]	1.8	1.9	2.9	1.2	2.4	2.2
Standard deviation [µm]	0.196	0.105	0.214	0.271	0.442	0.241
Ablation rate [mg/pulse]	9.79×10^{-10}	2.46×10^{-09}	1.85×10^{-09}	2.73×10^{-07}	3.43×10^{-07}	3.67×10^{-07}

The ablation rate per pulse has been determined gravimetrically from the difference between the untreated and the machined samples divided by the total number of pulses the patch was exposed to (Gamaly, Madsen et al. 2005). The ablation rate for bumpy structures is at least two orders of magnitude higher than the one for pillow-like structures and varies with the gas environment.

Figure 4.4g - i show the "best" patches of bumpy structures. They were obtained at the same accumulated intensity $I_{line\text{-}accumulated}$, however, for different combinations of $I_{pulse\text{-}accumulated}$ and φ_{line} for all three gases, as explained in the following. Figure 4.5 illustrates the combinations of φ_{line} and $I_{pulse\text{-}accumulated}$, which lead to pillow–like and bumpy structures respectively. For better visualization, Figure 4.5d schematically summarizes the results from Figure 4.5a - c.

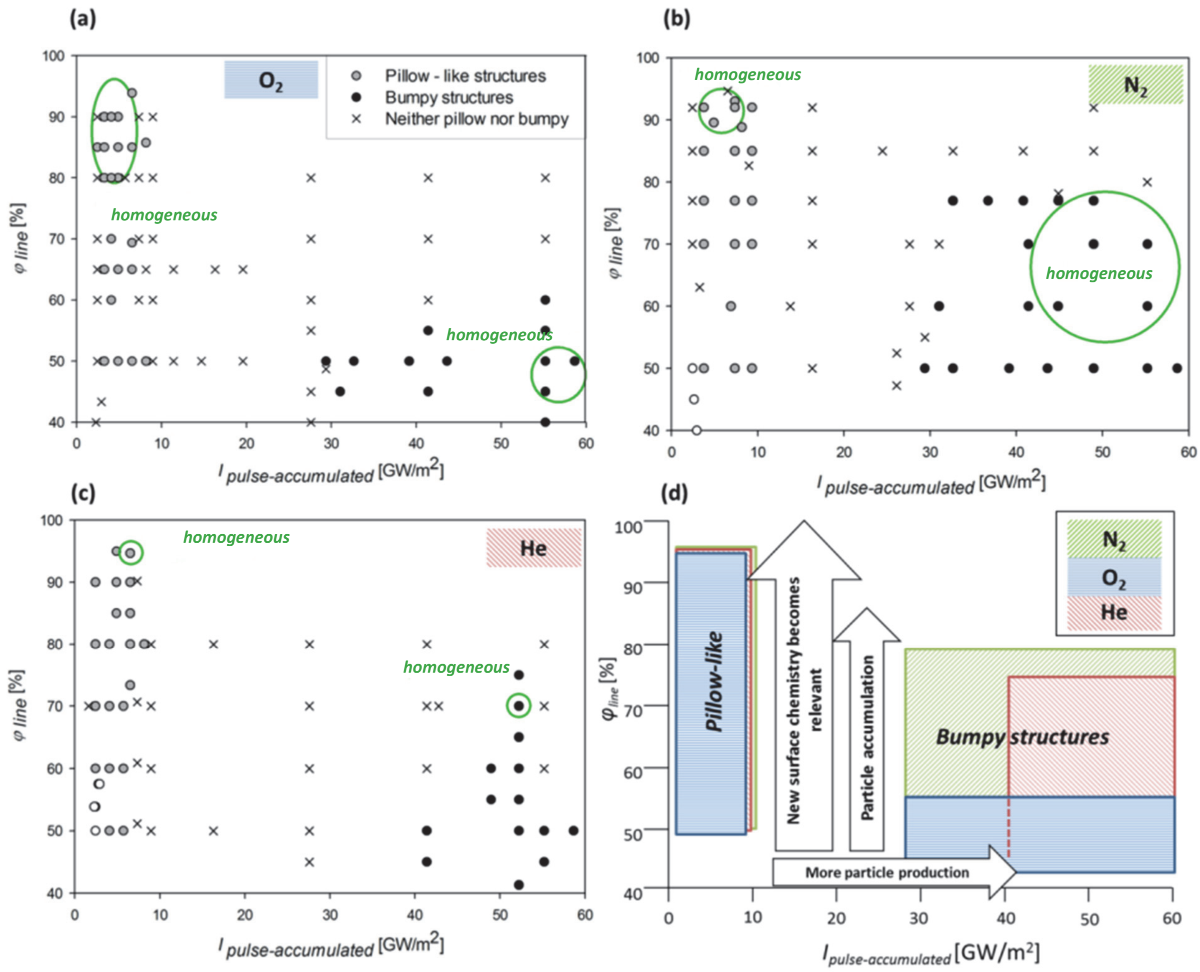

Figure 4.5: Overlap φ_{line} vs. $I_{pulse\text{-}accumulated}$ for oxygen (a), nitrogen (b) and helium (c). The graphs (a-c) are schematically summarized in (d).

Pillow-like structures have been found within the same range of settings for all three gases (Figure 4.5a - c) between similar lower and upper thresholds (Table 4.3).

Table 4.3: Intensity thresholds for pillow-like and bumpy structures.

		Lower threshold			**Homogenous**			**Upper threshold**		
		Oxygen	Nitrogen	Helium	Oxygen	Nitrogen	Helium	Oxygen	Nitrogen	Helium
Pillow-like	$I_{pulse\text{-}acc.}$ [GW/m^2]	2.4	3.1	2.4	6.6	4.9	6.6	8.5	8.5	8.5
	φ_{line} [%]	50	50	60	94	90	95	95	90	95
Bumpy	$I_{pulse\text{-}acc.}$ [GW/m^2]	28.0	28.0	40	29.4	52.2	52.2	55.0	55.0	55.0
	φ_{line} [%]	50	35	50	50	35	70	60	70	75

However, homogeneous patches of pillow-like structures as shown in Figure 4.4a, c and d were limited to only a few combinations of overlap φ_{line} and intensity $I_{pulse\text{-}accumulated}$ for nitrogen (Figure 4.5b) and only a single one for helium (Figure 4.5c), whereas in the case of oxygen several setting combinations result in the desired structures (Figure 4.5a). It is surprising that we found the most homogeneous patches of pillow-like structures and the widest range of appropriate settings in oxygen, whereas previous work has recommended a noble gas like helium to achieve optimum structure formation (Perrie, Gill et al. 2004, Robinson and Jackson 2006, Nayak, Gupta et al. 2008).

Bumpy structures are produced at the same intensity range for nitrogen and oxygen, while the lower intensity threshold was greater in helium (Table 4.3). The particularly large amount of combinations of settings in Figure 4.5b and d for nitrogen results from the upper threshold located at φ_{line} of 78 % and $I_{pulse\text{-}accumulated}$ of 28 GW/m^2. Interestingly, patches of homogeneous bumpy structures are found for a few combinations in nitrogen, but their occurrence is quite limited for the other two gases (green circle in Figure 4.5a - c).

Figure 4.5 shows that the surface morphology changes gradually with the gas mixture of oxygen and nitrogen. At constant $I_{pulse\text{-}accumulated}$ and φ_{line} patches of homogeneous pillow-like structures cannot be produced anymore with an increasing proportion of nitrogen in the mixture.

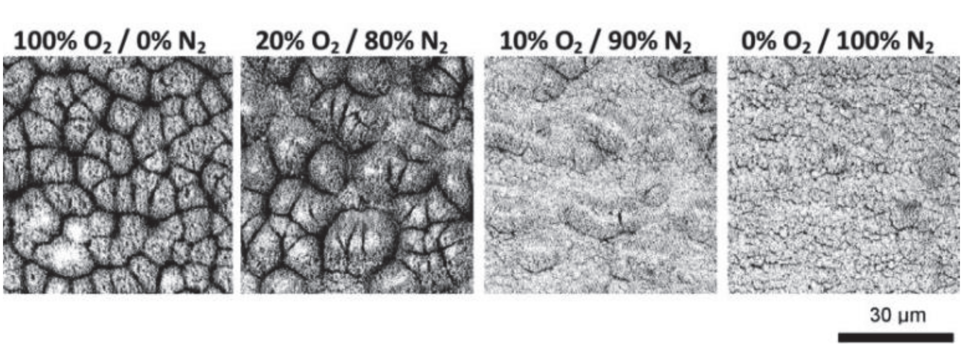

Figure 4.6: SEMs at $I_{line\text{-}accumulated}$ of 4.8 GW / m^2 and φ_{line} of 85 % at different mixtures of nitrogen and oxygen.

4.4.3 Surface chemistry

The chemical composition of the machined surface as well as of the ablated particles was analyzed for samples of pillow-like and bumpy structures that were machined in oxygen, nitrogen or helium and exposed to different gas environments after machining. The nomenclature that is used for the samples throughout this section is introduced in Table 4.4.

Table 4.4: Nomenclature of samples as combinations of machining and exposure gas environment.

		Machining		
		Oxygen	**Nitrogen**	**Helium**
Exposure	**Oxygen**	O_2-O_2	N_2-O_2	He-O_2
	Nitrogen	O_2-N_2	N_2-N_2	He-N_2
	Helium	O_2-He	N_2-He	He-He

Visual inspection of the surfaces after the final exposure step revealed characteristic colors (Figure 4.7a): for machining in oxygen a white-blue color indicates TiO_2 (Morales, Novaro et al. 1995), and for nitrogen a golden-brown color, which points towards TiN (Niyomsoan, Grant et al. 2002). Samples machined in helium were similar in color but darker than the ones machined in oxygen. After the cleaning step all samples showed basically the same color. Independently of the machining gas, the resulting topologies and length scales are alike for surface features of pillow-like and bumpy structures, respectively. Thus, these color variations cannot be classified as structural color (Gu, Uetsuka et al. 2003, Ahsan, Ahmed et al. 2011). The solution of the particles obtained from the cleaning step was much darker for machining in nitrogen than the solutions for the respective particles from machining in oxygen or helium. Only the particles for nitrogen maintain a stable suspension (Figure 4.7b). For particle size distribution of the solutions see Appendix B.

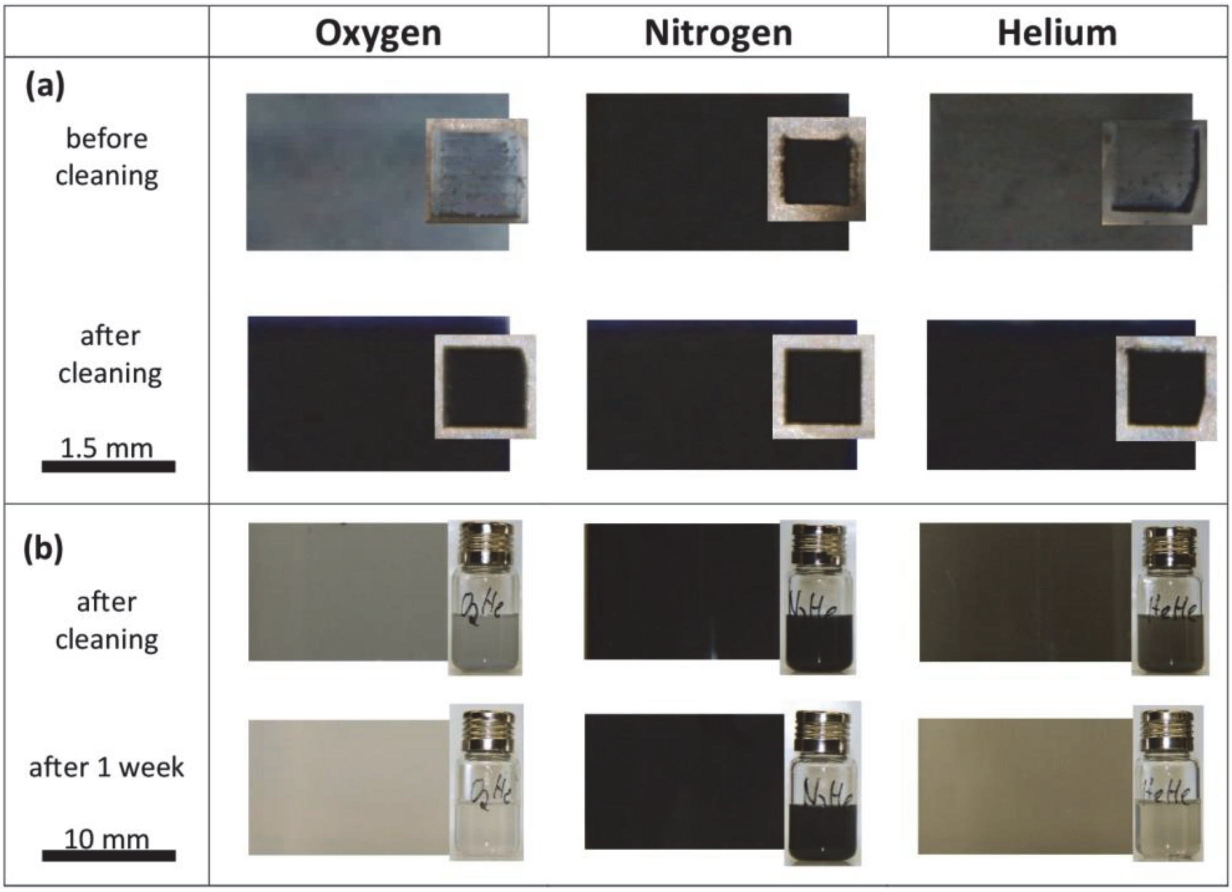

Figure 4.7: Surfaces (a) and particles in EtOH solution (b) after machining of homogeneous bumpy structures in oxygen, nitrogen and helium with subsequent exposure to helium. Images in (a) are highly magnified.

The XPS derived data in Figure 4.7 show the relative proportions of Ti, O, N and C for each combination of machining and exposure environment as well as for a non-machined blank sample. The content of O1s and C1s did not vary significantly. However, samples that were machined in nitrogen (N_2–N_2, N_2–O_2 and N_2-He) have larger proportions of N1s than samples machined in oxygen, which is displayed as the averaged N1s value in Figure 4.8.

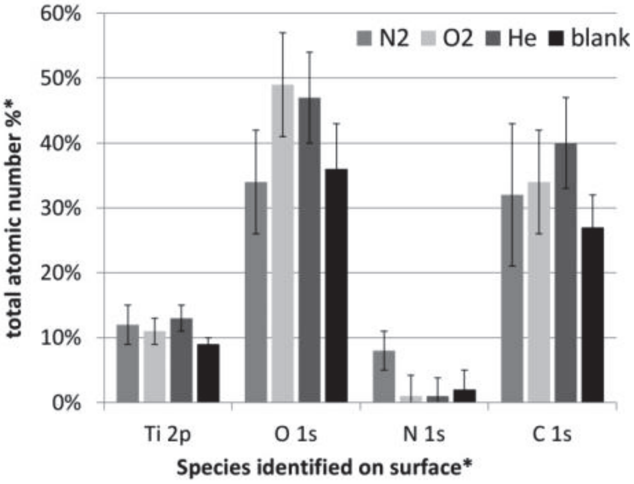

Figure 4.8: Species content in the surface obtained from XPS on samples machined in nitrogen, oxygen and helium for all exposure environments excluding contaminants*.

Figure 4.9a exhibits the peak for nitrogen N1s for the surfaces machined in oxygen (O_2-O_2) and nitrogen (N_2-N_2). The O_2-O_2 sample shows molecular nitrogen at around 400 eV. For the N_2-N_2 sample the peak has shifted to about 399 eV and two new peaks can be discerned: TiN at 396.5 eV and oxidized TiN around 395.5 eV (Prieto and Kirby 1995). We assume that the oxidation of TiN occurs instantaneously during the transfer of the sample from the reactor to the transport vessel.

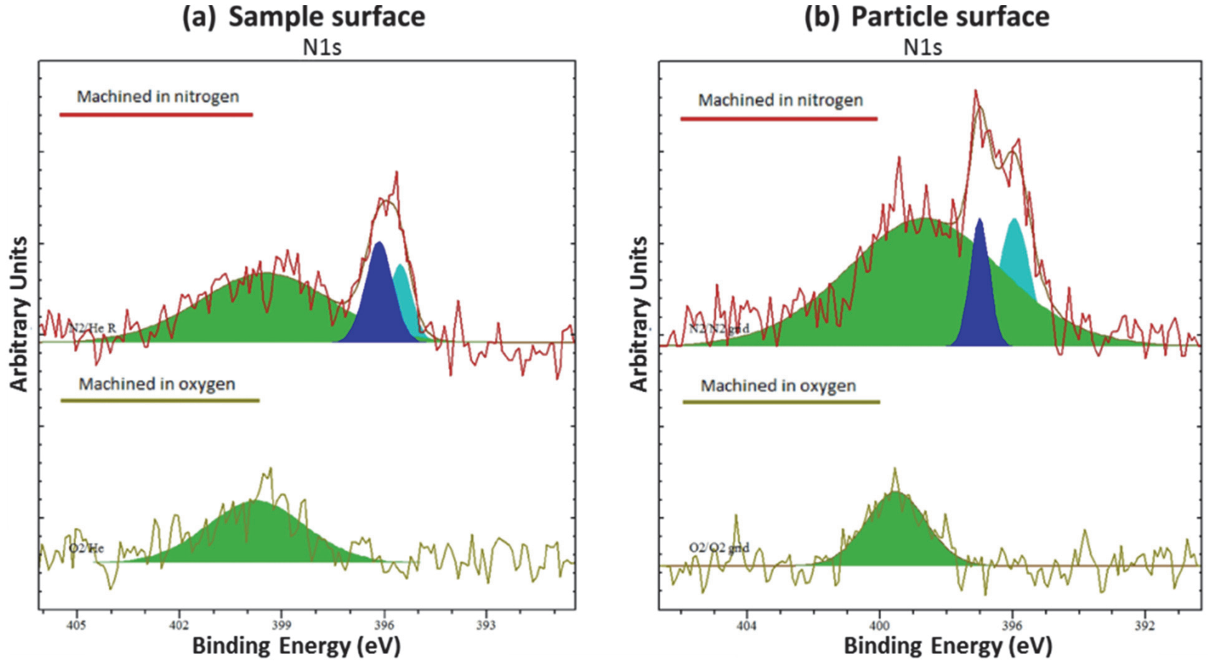

Figure 4.9: XPS spectra for N2-He and O2-He samples (a). XPS spectra for the particles ablated of N2-He and O2-He samples (b). Green: N_2, dark blue: TiN, light blue: oxidized TiN.

The larger amount of nitrogen reported in Figure 4.8 is linked with a smaller relative proportion of oxygen, while the relative proportion of Ti2p was similar for all treatments. The subsequent exposure to nitrogen of a sample machined in oxygen or helium (O_2–N_2, He-N_2) did not lead to an increase of the nitrogen content at the surface. Generally, the exposure step had no significant effect on the final chemical composition of the surface (Detailed XPS data for all experiments can be found in the Appendix B). Surprisingly, the samples machined in helium showed oxygen content on the surface even though no oxygen had been present in the machining environment. This oxygen likely originates from the oxide layer already present on the sample before machining.

The chemical composition of the ablated particles was found to correspond to the chemical composition of the surface (see Figure 4.8b). The proportion of titanium contained in the different compounds for samples (surfaces and particles) machined in nitrogen is respectively, 60 to 70 %

for TiO_2 and 15 to 30 % for TiN (including oxidized TiN). The only difference between the particles and the surfaces was found in the O1s peak, which is related to the O-Ti bond. For the particles this peak is at 530 eV, on the surfaces (even in the as-received Ti samples) it is usually shifted by 0.5-0.7 eV to lower binding energy. After the sample was carefully cleaned by Ar+ ion sputtering, the peak shifted back to its canonical position, while peaks in the C1s signal related to hydroxyl and carboxyl carbon disappeared. We thus ascribe this shift to contamination that currently cannot be prevented during the transfer of the samples from the processing chamber to a portable vacuum chamber and from there to sonication in acetone.

4.5 Discussion

4.5.1 General interaction regimes and contribution of the gas environment

The line width experiments serve to identify how the gas environment affects the effective intensity I_{eff} and the ablation threshold I_{abl} (where the latter represents the initial material response), independently of the applied raster scanning method for patches. The dependence of I_{abl} on the gas environment has been postulated before by Gamaly *et al.* (Gamaly, Madsen et al. 2005, Gamaly 2011) and is confirmed by our results (Table 4.1), since all other parameters that determine I_{abl} were constant during our experiments: pulse duration (Le Harzic, Breitling et al. 2005), repetition rate (Mannion, Magee et al. 2004, Uppal and Shiakolas 2008) and target material (Mannion, Magee et al. 2004). We suggest that changes in I_{eff} are caused by the laser energy being absorbed, while the optical properties of the surrounding gas medium remain isotropic. However, the absorption can occur in combination with a temporal and spatial disturbance of the beam propagation, which results in a redistribution of the intensity throughout the beam cross section. The disturbances originate from non-isotropic optical properties of the surrounding medium (Miles, Carruthers et al. 2011).

We suggest that the gas specific beam diameters ω_{model} that were obtained from Liu's model (Table 4.1) applied to our experimental results originate from such deformations of the ideal Gaussian intensity distribution. Since ω_{model} is defined for a specific fraction of the pulse energy ($1-1/e^2 = 86.5$ %), different values of ω_{model} indicate that this fraction is reached closer or further away from the center of the beam (ISO 2005). We hypothesize that I_{eff} depends mainly on effects caused by the interaction between the laser beam and its environment, as illustrated in Figure 4.1.

Our experiments have been conducted at several orders of magnitude below the threshold, where self-focusing effects or deformations of the beam shape due to the Kerr effect should be taken into account (Sun and Longtin 2001, Ju and Longtin 2004). There is also no relevant interaction between the laser pulses and the ablation plasma due to the different time scales of pulse duration and plasma development (Margetic, Ban et al. 2003, Henley, Carey et al. 2005, König, Nolte et al. 2005). Even with the pulse spacing of 100 µs in our experiments, the subsequent pulse cannot interact with the plasma produced by the former pulse (Barthélemy, Margot et al. 2005). Since titanium is ionized at only 6.82 eV (658.8 kJ/mol), and the resulting shock wave is not strong enough to maintain a relevant plasma density for more than 1 µs (Paolasini and Kietzig 2014). The laser beam interacts, however, with the particle cloud that forms in front of the target surface during ablation (see 3 in Figure 4.1) (Burghardt, Scheede et al. 1999) in particular at high $I_{pulse-accumulated}$, when respectively more particles are produced at high ablation rates (Table 4.2). Consequently, when the first particles are ablated from the target surface, the ablation rate depends only on $I_{pulse-accumulated}$. However, once the initial particle cloud is formed the ablation rate depends on I_{eff}, since only the intensity that reaches the surface contributes to ablation. The volume to which the particle cloud expands, is typically dictated by the sonic speed for the respective gas (Table 4.5) (Marble 1963).

Table 4.5: Material properties for molecular oxygen, nitrogen and helium (*(MSE_Handbook 1994)).

	Optical Kerr coefficient (Ju and Longtin 2004) [cm^2/W]	**Sonic speed*** [m/s]	**Atomic mass*** [u]	**Density at 273 °K, 1atm*** [kg/m^3]	**Thermal velocity*** [m/s]	**Thermal conductivity*** [W/(m K)]
Oxygen	9.7×10^{-19}	316	16	1.331	460	23.8
Nitrogen	4.5×10^{-19}	353	14	1.249	471	25.8
Helium	3.5×10^{-21}	1019	4	0.179	1246	148.1

Accordingly, the particle cloud is largest for helium due to the three-fold larger sonic speed compared to the other gases. Thus the non-machined surface is shielded in the direction of the incoming laser beam and also in the machining direction of a line (Figure 4.10a3). In our experiments we observed visually that this effect was very pronounced at higher $I_{pulse\text{-}accumulated}$ with increasing density of the particle cloud due to more particle production (Figure 4.10c3 and Table 4.2). In contrast, the lower sonic speeds for oxygen and nitrogen cause the particle cloud to stay close to the irradiated spot on the surface (Figure 4.10a1-a2 and c1-c2). The relative difference of the values for the sonic speed in the three gases (Table 4.5) fits with the relative locations of the curves in Figure 4.3. However, above $I_{pulse\text{-}accumulated}$ of 30 GW/m^2 the results for nitrogen and helium do no longer correlate directly with the gas properties, which we explain by considering the XPS results. Figure 4.8 has shown that the particles ablated in nitrogen contain TiN, which has a higher reflectivity of 0.75 compared to 0.37 for TiO_2 (MRS handbook (1994)). We assume that this increased reflectivity leads to more scattering of the incoming laser light, when it hits the particle cloud.

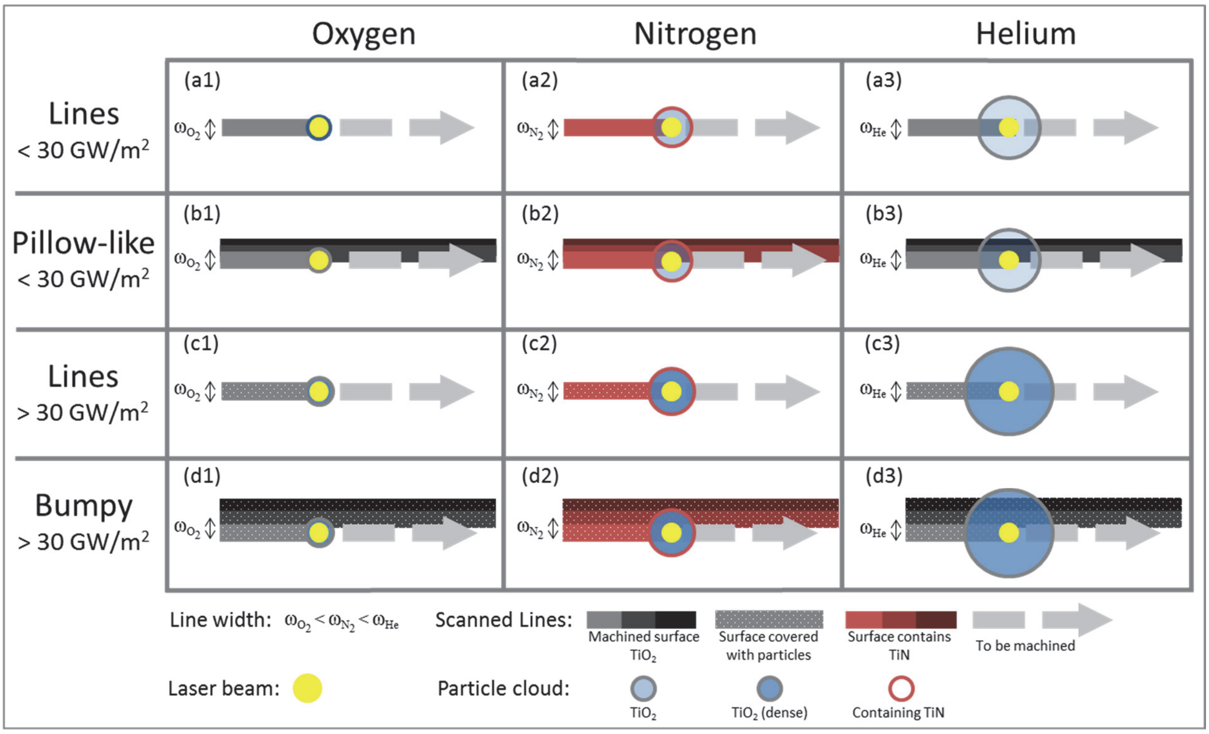

Figure 4.10: Particle cloud for machining of lines and microstructures and chemical composition of sample and particle surface for oxygen, nitrogen and helium environments.

We suggest that the actual values of ω_{eff} and ω_{model} in the three different gases are determined by the non-isotropic properties of the gas environment, which originate from the particle cloud and its chemistry. In oxygen the particle cloud shields the surface from the incoming laser irradiation. Thereby, the laser energy is absorbed by the particles (Figure 4.10a1 and c1) resulting in the lowest I_{eff} and consequently ω_{eff} of all three environments. In the case of the nitrogen environment below 30 GW/m^2 the particle cloud is of similar density and size as in oxygen background, which correlates with the measured ablation rate in Table 4.2, resulting in comparable ω_{eff} (Figure 4.10a2). The chemical composition of the particle cloud only plays a role above 30 GW/m^2, when the cloud is respectively larger (Figure 4.10c2): The higher reflection of the laser light on TiN causes more scattering at the particles of the cloud. However, we propose that the particle cloud is not dense enough to reassemble a homogeneous medium, so that the local refractive index in the particle cloud could vary, and the overall optical properties of the environment would have to be considered as non-isotropic. As a result, ω_{model} would become wider, consistently with our results.

A similar explanation can be given for helium (Figure 4.10a3 and c3). The relatively large cloud causes the incoming beam to travel a longer distance through the particle cloud, so that more scattering occurs, which results again in a non-isotropic refractive index. Consequently, the intensity across the beam is redistributed even more than in nitrogen atmosphere, as indicated by the largest ω_{model}. The SEM images in Figure 4.3 confirm this observation: The microstructures occur at the center of the lines, where intensity is highest. In helium environment the microstructures were less developed than those in nitrogen, but ω_{eff} was larger in helium. This indicates a shift to higher intensities at the tails of the beam and lower peak intensity I_0 in the center.

4.5.2 Method specific interaction regimes

In contrast to the machining of a single line, structure formation on a patch depends not only on the immediate intensity input during the machining of each line (expressed by $I_{pulse\text{-}accumulated}$), but also on the delayed input, when the lines overlap with φ_{line}. Besides the resulting higher $I_{line\text{-}accumulated}$, the spatial aspects of the machining process, as well as possible effects resulting from the increasing total processing time must also be considered. In Figure 4.5d the arrows along the y-axis represent effects that depend on the applied machining process.

The production of homogeneous patches of pillow-like structures requires generally high overlap φ_{line} (Figure 4.6). Even though particle production is limited due to the low $I_{pulse\text{-}accumulated}$ (Table 4.3), the relatively long machining time of approximately one hour allows particle accumulation in the environment and on the sample itself. More importantly, a subsequently machined line is machined on a surface that had already been topologically and chemically modified by the previously scanned line (Figure 4.10b1 to b3). While the resulting topology is identical for all three gases, the surface chemistry varies (Figure 4.8 and Figure 4.9). The most homogeneous patches of pillow-like structures in nitrogen environment were only obtained at higher $I_{pulse\text{-}accumulated}$ than those for the other two gases yet with the least coverage of features (Figure 4.4e). This observation points towards a particular role of TiN as one of the main components of the surface (Figure 4.10b2). While the contribution of TiN is relatively weak with a share of maximum 20 % of the chemical species on the surface (see section 3.3), the considerably higher reflectivity of 0.75 for TiN, compared to 0.37 for TiO_2 (1994) nevertheless reduces I_{eff}. Figure 4.6 confirms this observation, as differences of the surface topology compared to 100 % oxygen became visible only in an environment with more than 90 % nitrogen. The identical thresholds for the formation of pillow-like structures (Table 4.3) in helium and oxygen environments indicate that the machining of a single line (Figure 4.10a3) and a patch (Figure 4.10b3) follows the same mechanism in both gases. Since the larger ω_{eff} in helium had been compensated in the calculation of the overlap φ_{line}, the zones for pillow-like structures in all gases in Figure 4.5d are identical. However, further investigation is required to determine, why a homogeneous patch of pillow-like structures was only obtained for one single combination of $I_{line\text{-}accumulated}$ and φ_{line} in helium.

The production of bumpy structures (Figure 4.5d) is greatly influenced by the applied raster scanning machining method with overlapping lines, since differences between the gases appear only with increasing φ_{line}. Bumpy structures were produced at $I_{pulse\text{-}accumulated}$ greater than 30 GW/m^2, which is the intensity level, where ω_{eff} in nitrogen becomes similar to ω_{eff} in helium (Figure 4.3) as outlined before. Thus, the previous discussion of the particle cloud for the machining of lines Figure 4.10c1 to Figure 4.10c3 applies for the production of bumpy structures as shown in Figure 4.10d1 to Figure 4.10d3. Additionally, particles are increasingly deposited on the surface during the machining of bumpy structures. In the case of nitrogen (Figure 4.10c2), the actual coverage of the surface with TiN is larger than 30 % (see section 3.3), as particles containing TiN are re-deposited onto the surface. Therefore, we conclude that the optical properties of TiN prevail even at low φ_{line}.

A simple calculation illustrates the attenuation of I_{eff} on a hypothetical surface of pure TiN: The upper threshold for bumpy structures in nitrogen was reached at $I_{pulse\text{-}accumulated}$ of 40 GW/m^2 and φ_{line} = 80 % (Table 4.3), which is equivalent to the total theoretical intensity $I_{line\text{-}accumulated}$ of 120 GW/m^2. Considering that TiN reflects twice as much laser energy as TiO_2, I_{eff} could be as low as 60 GW/m^2 (= 50 % $I_{line\text{-}accumulated}$). This intensity can be achieved with only φ_{line} = 55 % at constant $I_{pulse\text{-}accumulated}$ of 40 GW/m^2 in oxygen, which is the upper threshold for bumpy structures machined in oxygen (Table 4.3 and Figure 4.5d). In the case of helium the higher ablation threshold I_{abl} (Table 4.1) translates into a higher intensity threshold for the production of bumpy structures. The extension of the zone of combinations of $I_{pulse\text{-}accumulated}$ and φ_{line} for helium in Figure 4.5d with φ_{line} up to 75 % is possible with the redistribution of intensity throughout the cross section of the beam in helium, which we reported from the line width experiments. With such a beam profile, higher overlap φ_{line} is possible, before the upper threshold is reached, since the increase of the total intensity $I_{line\text{-}accumulated}$ is dampened, when lines with lower peak intensities overlap.

4.6 Conclusions

The influence of the gas environment during the machining of microstructures with a femtosecond laser has been determined to originate from the production of intensity attenuating particles in combination with the altered chemistry of both the target surface and the ablated particles. Although it is challenging to control these interacting effects, the goal of this work is to produce homogeneous patches of microstructures with the same quality that was achieved for bumpy structures in the case of all three gases. Bumpy structures proofed to be more robust against variations in the effective intensity I_{eff} than the pillow-like structures. Homogeneous patches of pillow-like structures have been produced in oxygen and with lower quality in nitrogen and helium. In contrast to previously reported experiments (Perrie, Gill et al. 2004, Robinson and Jackson 2006, Nayak, Gupta et al. 2008), we found that oxygen is the ideal machining environment for highly homogeneous patches. The presence of a certain gas can actually be used to control I_{eff}, which is ultimately responsible for the resulting surface morphology. The alteration of surface chemistry happens only during the machining process, when the ablation plasma is present. A subsequent exposure step does not alter the shares of TiO_2 and TiN any further. We have shown for the specific case of laser machining in nitrogen atmosphere, that both surface morphology and surface chemistry can be modified in a single step. Titanium in particular is of high interest for biomedical applications. It has recently been found that rough titanium alloys promote the growth of bone cells and the attachment of blood vessels since the roughness helps to maximize the necessary interaction between the adhering cells and the implant material (Olivares-Navarrete, Hyzy et al. 2013). Furthermore, surfaces containing TiN promote cell growth compared to surfaces consisting of TiO_2 (Czarnowska, Wierzchoń et al. 1999, Zhao, Wong et al. 2013). The process presented in this research seems like a promising candidate not only to provide the required roughness but also to enhance biocompatibility.

Acknowledgment

This research has been supported by the National Science and Research Council (NSERC) of Canada through individual Discovery Grants to A. Kietzig and F. Rosei. We thank the Plasma Processing Laboratory for access to its infrastructure. A. Kietzig and F. Rosei acknowledge FRQNT for a team grant. F. Rosei is grateful to the Canada Research Chairs program for partial salary support and thanks NSERC for a EWR Steacie Memorial Fellowship.

References

Please refer to the global bibliography at the end of the thesis.

Chapter 5

5. Dependence of capillary forces on relative humidity and the surface properties of femtosecond laser micromachined titanium

5.1 Preface

This chapter presents an article that has been published in the *Journal of Colloid and Interface Science*. The complete citation of the published article is:

Lehr, J. and Kietzig, A.-M., Dependence of capillary forces on relative humidity and the surface properties of femtosecond laser micromachined titanium. Journal of Colloid and Interface Science, 2015. 448: p. 356-366.

The types of microstructures that are presented in the previous chapters were used for the force measurements with AFM. Additionally to the bumpy like structures obtained in pure oxygen and nitrogen, ripple structures (LIPSS) with less roughness were chosen. These were also machined in oxygen and nitrogen like the bumpy structures. A third type of ripple structures was added that had been obtained from micromachining in water during other experiments carried out by Luke Matus in our laboratory. Furthermore, these samples were subsequently to micromachining exposed to three different media: Oxygen, carbon dioxide or water. The purpose of this additional exposure step was to investigate the phenomenon of contact angle evolution. The high sensitivity of AFM towards variations of the chemical composition of the surface was expected to permit detecting variations of the capillary force between the three exposure environments. Capillary force had never been investigated on femtosecond laser micromachined surfaces before.

Dependence of capillary forces on relative humidity and the surface properties of femtosecond laser micromachined titanium

Jorge Lehr, Anne-Marie Kietzig

Department of Chemical Engineering, McGill University, 3610 University Street, H3A 0C5, Montreal, QC, Canada

Abstract

The magnitude of capillary forces has to be limited in technical applications like precision printing to allow accurate positioning of liquids on the target surface. Colloidal probe atomic force microscopy (AFM) was carried out on rough femtosecond laser micromachined titanium in a controlled environment at three different levels of relative humidity. The titanium samples were covered either with periodic nanoscale ripple structures or with microscopic bumpy structures. Three machining environments were chosen: While machining in pure oxygen and water resulted in surfaces consisting of TiO_2, machining in pure nitrogen resulted in a composite surface of TiO_2 and TiN. All types of samples were subsequently exposed to pure oxygen, carbon dioxide or water, and showed different levels of wettability and capillary force.

Ripple structures machined in pure oxygen were found to hinder the formation of capillary forces and were least sensitive to an increase of relative humidity. This study confirms that roughness and chemical composition at the relevant nanoscopic length scale determine the formation of capillary bridges and thus the extent of capillary forces. Furthermore, we observed a correlation between the receding contact angle and the capillary force which provides evidence that the exposure step after micromachining alters the chemical composition of the surfaces.

5.2 Introduction

The magnitude of capillary forces, which are the dominant attractive forces between two surfaces (de Gennes 1985), is altered by changes of the relative humidity (Quon, Ulman et al. 2000). Researchers have extensively studied the influence of the latter on the extent of capillary forces, since fluctuations of the relative humidity have to be considered in many technical applications, when the environmental conditions are not controlled (Ando 2000, Quon, Ulman et al. 2000, Sedin and Rowlen 2000, Ata, Rabinovich et al. 2002, Jang, Schatz et al. 2004, Riedo, Pallaci et al. 2004, Feiler, Stiernstedt et al. 2007, Sheng Chao and Jen Fin 2008, Butt and Kappl 2009, Butt and Kappl 2010). It is important to anticipate how much capillary forces vary with respect to a certain humidity level, particularly in the context of stick-slip motion (Bhushan, Wang et al. 2009) and wet friction (Kietzig, Hatzikiriakos et al. 2010) between two surfaces or during the coating of surfaces (Hecht, Schilz et al. 1998, Assad, Leshansky et al. 2012, Kargl, Mohan et al. 2013, Masheder, Urata et al. 2014). Furthermore, controlling capillary forces is crucial, when liquids have to be positioned accurately on a surface during precision printing of polymers (Shield, Bogy et al. 1986, Lee, Lin et al. 2010, Mhetre, Carr et al. 2010, Schirmer, Kullmann et al. 2010), of polymer-electronics (Garnier, Hajlaoui et al. 1994) or of biomolecules on lab-on-a-chip devices (Xu, Junfei et al. 2010, Yamaguchi, Ueno et al. 2012).

The magnitude of capillary forces, which are usually measured with colloidal probe atomic force microscopy (AFM), depends mainly on the actual contact geometry and the surface wettability (Fisher and Israelachvili 1981, Butt 1991, Ducker, Senden et al. 1991, Xudong and Linmao 2000, Ata, Rabinovich et al. 2002, Riedo, Pallaci et al. 2004, Zhang, Lamb et al. 2007, Butt and Kappl 2009). Hence, measuring capillary forces allows exploring the relationship between surface wettability and capillary forces (Preuss and Butt 1998, Mittal 2008). The fundamental work on capillary forces measured with AFM has been performed by Weisenhorn *et al.* (Weisenhorn, Hansma et al. 2009) on flat surfaces and by Ata *et al.* as well as by Butt *et al.* on rough surfaces (Ata, Rabinovich et al. 2002, Butt, Farshchi-Tabrizi et al. 2006). Capillary force can be measured when the meniscus, which is formed between the surface and the AFM probe at a distance that equals the Kelvin-length λ_k (Eq. (5.1)), is stretched to a capillary bridge. The formation of capillary bridges is hindered when the roughness of the AFM probe and/or the roughness of the sample surface are of the same length scale as the Kelvin-length λ_k or the curvature of the meniscus r_{curv} (Eq. (5.2)) (Butt and Kappl 2009, Israelachvili 2010).

$$\lambda_k = \frac{\gamma_{LA} V_M}{RT} \tag{5.1}$$

$$r_{curv} = \frac{V_M \gamma_{LA}}{RT ln\left(\frac{p_v}{p_s(T)}\right)} \tag{5.2}$$

Both r_{curv} and λ_k are functions of the liquid's surface tension γ_{LA}, the molar volume V_M, the ideal gas constant R, the temperature T, the vapor pressure p_v and the saturation vapor pressure $p_s(T)$. For the case of water at ambient conditions Eq. (5.1) and Eq. (5.2) compute to a value in the range of 0.5 to 5 nm as the topological length scale that influences the formation of capillary bridges, denoted by l_{cap} in this study (see calculation in the Appendix C). Butt *et al.* have pointed out that performing roughness measurements at l_{cap} is a challenging and hence rarely performed task; however, it is required to accurately predict the magnitude of capillary forces on a rough surface (Butt and Kappl 2009).

Since force measurements with AFM do not discriminate between capillary forces and the other components of surface forces, like van der Waals (vdW) forces, we introduce the concept of *humidity sensitivity* (S_X) to expose the particular dependence of capillary forces on relative humidity (RH). S_X (Eq. (5.3)) quantifies how capillary forces change with different levels of RH on a particular type of surface. S_X is defined as the ratio of the measured forces ($F_{(X)}$) at a certain RH level X to the force at 0 % RH (F_0), where capillary forces can be neglected (Rabinovich, Singh et al. 2011), and the total surface force is predominantly composed of vdW forces (Stifter, Marti et al. 2000).

$$S_X = \frac{F_{(X)}}{F_0} \tag{5.3}$$

In this study, two types of homogeneous surface structures were used, which were obtained from micromachining titanium sheets with a femtosecond laser: The first type is well-known as *laser induced periodic surface structures* (LIPSS) or *ripple* structures (Nayak, Gupta et al. 2008, Chen, Fu et al. 2009, Cheng, Perrie et al. 2009, Eichstädt, Römer et al. 2013, Yong, Chen et al. 2013); the second type shows characteristic microscale *columnar* or *bumpy* features that are covered with ripples (Perrie, Gill et al. 2004, Groenendijk and Meijer 2006, Vorobyev and Guo 2007, Nayak, Gupta et al. 2008, Jiwhan, Jae-Hoon et al. 2010, Lehr and Kietzig 2014). The difference between the two types of structures originates from the level of laser machining fluence, which is 5 to 10 times larger for bumpy than for ripple structures.

Femtosecond laser micromachined surfaces are ideal objects for studies on wettability and capillary forces since they exhibit two particular phenomena: Our recent study has shown that the surface topology and chemistry are altered simultaneously when micromachining takes place in a pure environment of nitrogen (Lehr, de Marchi et al. 2014). Since the wetting behaviour depends on both surface topology and chemistry (Marmur 1992, Extrand 2003, Tadmor 2011), this allows for customized wettability. Furthermore, the exposure to air after micromachining without any further chemical or physical treatment has been observed to lead to an increase of the surface's contact angle resulting in hydrophobic metallic surfaces (Kietzig, Hatzikiriakos et al. 2009, Jagdheesh, Pathiraj et al. 2011, Bizi-bandoki, Valette et al. 2013, Kenar, Akman et al. 2013, Kruse, Anderson et al. 2013). Even though, it is still unclear to what extent O_2, CO_2, N_2 or H_2O (as reactive components of air) actually modify the surface chemistry during exposure to air, this observation opens a second path towards tailored wetting behavior.

Firstly, this study aims to determine the magnitude of capillary forces and humidity sensitivity on femtosecond laser micromachined titanium surfaces. Secondly, capillary force measurements will be used to explore the influence of the exposure to different environments during and after micromachining on the chemical composition and wetting behavior of the surface.

5.3 Materials and Methods

5.3.1 Preparation of samples

Square patches on sheets of titanium (McMaster-Carr, USA, 99.9 % purity) were prepared with femtosecond laser (Coherent Libra, USA) micromachining in a controlled environment. The wavelength was 800 nm, the repetition rate 10 kHz and the pulse duration <100 fs. The average output power of 4 W was attenuated with a half-wave plate and a polarizing beam splitter. The titanium sample surfaces were polished to an average roughness of $r_{RMS} = 180$ nm and sonicated in acetone for 10 min before being mounted on a computer controlled *x*-*z*-translation stage. The stage was located inside a sealed reactor vessel to maintain a stable the gas atmosphere (Lehr, de Marchi et al. 2014). For machining in liquid, the sample was placed inside a cuvette, which was mounted on another *x*-*z*-translation stage outside the reactor. The calculated beam diameter at focus was 66 μm inside the reactor and 15 μm inside the cuvette. The range of the applied fluence was 0.09 – 2.14 J/cm^2, and the accumulated intensities at 300 pulses per spot were 2.5 – 55.2

GW/m^2. Five types of samples (Table 5.1) with different surface topologies were prepared: ripple and bumpy structures in oxygen and nitrogen (99.999 % Praxair, Canada) at 450 Torr (Lehr, de Marchi et al. 2014) and ripple structures in water (Kietzig, Lehr et al. 2014). The subsequent exposure to O_2 and CO_2 took place inside the same reactor after micromachining, while the exposure to H_2O was conducted in a glass vial.

Table 5.1: Nomenclature of sample types that are used in the figures and tables in this manuscript.

		ripple			**rumpy**	
	machining environment	**O_2**	**N_2**	**H_2O**	**O_2**	**N_2**
exposure environment	**O_2**	$O_2(O_2)$ripple	$N_2(O_2)$ripple	$H_2O(O_2)$ripple	$O_2(O_2)$bumpy	$N_2(O_2)$bumpy
	CO_2	$O_2(CO_2)$ripple	$N_2(CO_2)$ripple	$H_2O(CO_2)$ripple	$O_2(CO_2)$bumpy	$N_2(CO_2)$bumpy
	H_2O	$O_2(H_2O)$ripple	$N_2(H_2O)$ripple	$H_2O(H_2O)$ripple	$O_2(H_2O)$bumpy	$N_2(H_2O)$bumpy

The exposure time was 18h at a pressure of 700 Torr and a temperature at 60°C. In the case of exposure to H_2O, the duration was 18h at ambient conditions. The samples were sonicated again for 10 min in acetone before characterization. In the following, the exposure environment, which is denoted inside brackets, is not shown when sample types are grouped by machining environments.

5.3.2 Preparation of AFM probes

Colloidal probes were prepared from soda-lime glass spheres (8.5-12 μm diameter, roughness r_{RMS} < 20 nm, Cospheric LLC, USA) and tip-less cantilevers (Type: TL-FM-10, Nanosensors™, Germany) following the method applied by Rutland *et al.* (1993) (Rutland and Senden 1993). The diameter of the spheres was chosen to be relatively large to maximize the force sensitivity (Derjaguin 1934, Butt, Cappella et al. 2005). The intrinsic contact angle (θ_E) of water on atomically-flat soda lime glass is $\theta_E = 0°$ (Sears 1955). A hydrophilic tip was chosen to improve the sensitivity towards capillary forces at low humidity levels (Jang, Schatz et al. 2004). The average spring constant was 2.44 N/m for the assembled probe and was determined before every measurement by thermal tuning with the AFM control software (Igor, Wavemetrix, USA). This spring constant was chosen to be large enough to avoid "jump-in" events (Butt, Cappella et al. 2005) and to reduce the noise caused by relatively low approach and retraction frequencies (see section 2.4).

5.3.3 Humidity control

A humidity cell (Asylum Research, USA) with integrated humidity sensor (Honeywell, USA) was used to ensure a controlled environment. The RH level was controlled by mixing dry nitrogen with water at different ratios in a wash bottle, which was connected to the humidity cell (Beach and Drelich 2011). Three different levels of RH were set: 0 %, 50 % and 70 % at a temperature of 28° +/- 2° Celsius. The force curves were taken 30 min after the desired RH level was reached to ensure that the RH level was constant within the entire cell. The cell was flushed with dry nitrogen after each measurement to avoid accumulation of water.

5.3.4 Contact mode AFM

100 pull-off force curves (Fisher and Israelachvili 1981, Larson, Drummond et al. 1993) were taken on each sample with an MFP-3D (Asylum Research, USA) at a scanning velocity of 3 nm/s in closed loop mode (Butt, Cappella et al. 2005). The force distance of 3 µm was chosen to cover the maximum height of a capillary bridge (~2.7 µm) (Uzhegova, Svistkov et al. 2014). The resulting scanning frequency was 0.5 Hz. The distance between each contact point on the surface was 10 µm so that every force curve was taken on a different spot on the surface. The virtual deflection [V/nm] and the deflection InvOLS [nm/V] were determined before every experiment. The κ factor was 1.09. The normal load on the surface was typically around 450 nN. Before

retraction the AFM probe rested on the sample for 10 s (dwell) to establish a thermodynamic equilibrium around the probe. The force data were numerically corrected with the radius of each colloidal probe and processed in Matlab®. Two-tail t-tests were carried out at a confidence level of 95 %. Flat titanium (RMS ~180 nm) and flat mica (RMS ~30 nm (Ostendorf, Schmitz et al. 2008)) served as control samples.

5.3.5 Imaging, goniometry & roughness measurements

The surfaces were imaged with scanning electron microscopy (SEM) with a FEI (USA) Inspect F-50 FE-SEM and a Hitachi (Japan) SU-8230 Field Emission-STEM equipped with an Oxford EBSD and INCA EDX (energy-dispersive X-ray spectroscope). The latter was used for chemical mapping, while the chemical composition of the surface was quantified with a Thermo Fisher (USA) VG Escalab 220i XL x-ray photon spectroscope (XPS). Image analysis was conducted in Matlab®. Lacunarity was determined with a program developed by T.J. Vadakkan (Vadakkan 2009). Roughness measurements were obtained with the MFP-3D AFM with an ultra-sharp tip (Olympus, Ø = 1 nm). Dynamic (advancing and receding) contact angles were measured with a Data Physics OCA 20 goniometer (Germany).

5.4 Results

5.4.1 Surface topology

Ripple (Figure 5.1a1 to c4) and bumpy (Figure 5.1d1 to e4) structures were obtained in three different machining environments. The characteristic topologies of these structures, which lead to their nomenclature (ripple, bumpy), are clearly visible at low magnification (1st and 2nd column in Figure 5.1): The highly ordered parallel line patterns that are typical for ripple structures can be seen after machining in oxygen (Figure 5.1a1 and a2) and nitrogen (Figure 5.1b1 and b2). However, H_2O ripple samples produced in water (Figure 5.1c1 and c2) have a less regular appearance with signs of previously melted material. O_2 bumpy (Figure 5.1d1 and d2) and N_2 bumpy (Figure 5.1e1 and e2) samples show essentially the same with ripple covered microstructures. Further differences between the machining environments are visible at higher magnifications (3rd and 4th column in Figure 5.1), where the SEM images show different types of features with dimensions of less than 500 nm. In particular on samples machined in oxygen, ripples are covered with spherical features with > 100 nm diameter, however these are smaller on ripple only samples (Figure 5.1a4) than on bumpy samples (Figure 5.1d4). The spherical as well as the irregularly shaped features are covered with substantially smaller nanoparticles with dimensions at the relevant length scale l_{cap} below 5 nm (Figure 5.1d4 and e4). The nanoscale topology of samples machined in water is clearly different (Figure 5.1c3 and c4): irregular shapes dominate, while > 100 nm spherical as well as the small nanoscale particles at l_{cap} are practically absent.

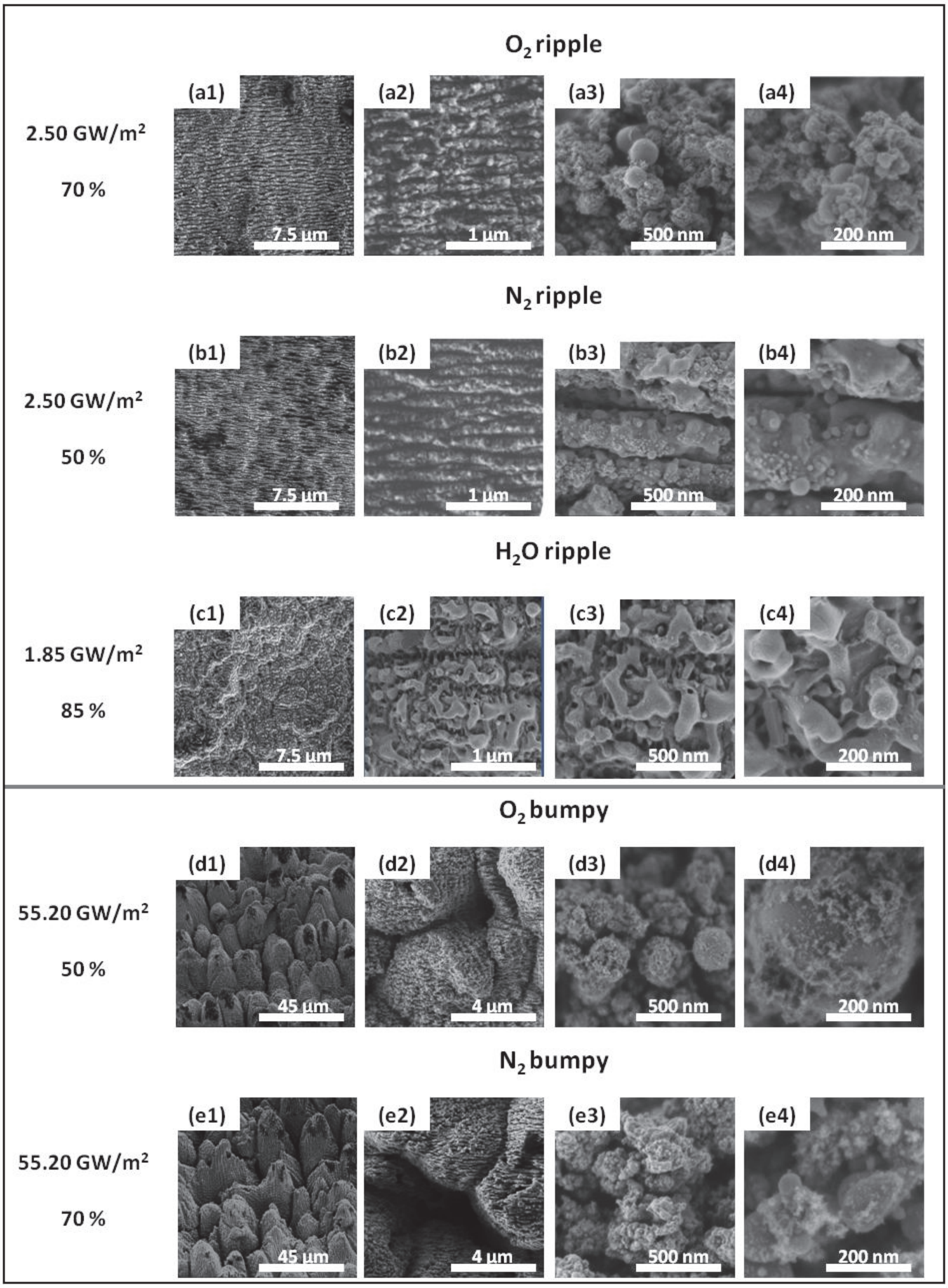

Figure 5.1: SEM images of ripple and bumpy structures machined in different environments.

Roughness values could not be determined by AFM on the samples in Figure 5.1 at the required length scale l_{cap} due to interactions between the sharp AFM tip and the larger surface features. Consequently, image analysis was used to obtain the feature dimensions from high resolution SEM images (3rd and 4th column in Figure 5.1). The resolution of the images allowed us to quantify feature dimensions with a lower limit of 1.5 nm. Hence, the images provide information of the order of l_{cap}. The histograms in Figure 5.2 show the distribution of dimensions for the detected nanoscale features. The boxes in Figure 5.2 highlight the percentage of features (l_{acc}) with a dimension smaller than the relevant length scale l_{cap} (< 5 nm) on each type of sample.

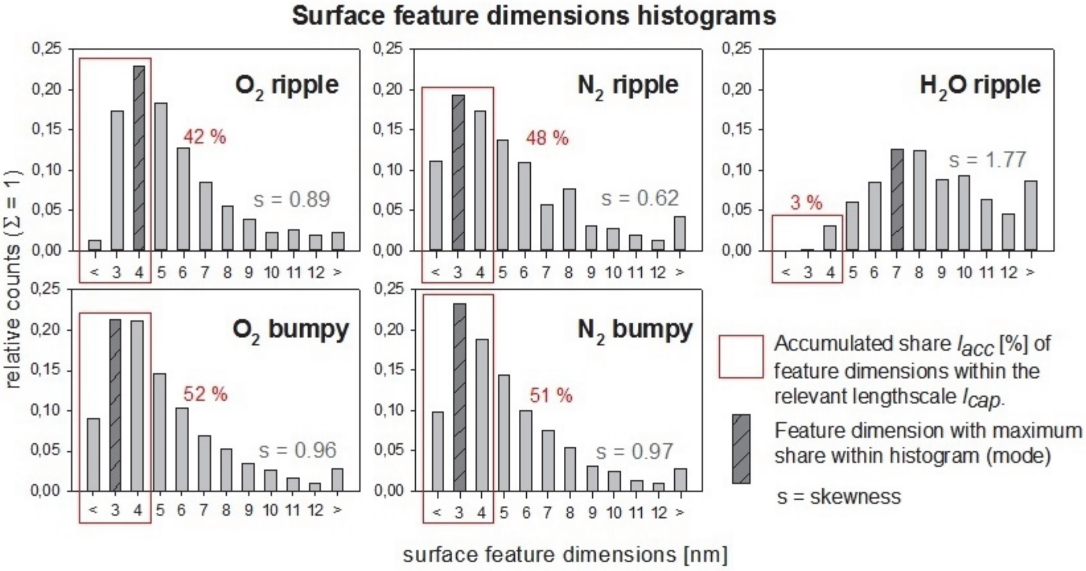

Figure 5.2: Histograms of surface feature dimensions.

The histograms show that O_2 ripple and H_2O ripple samples have a different surface topology on the nanoscale in comparison to all other types of samples; O_2 ripple samples have the lowest l_{acc} of 42 % and the highest *mode* at 4 nm among all samples machined in gases. The *mode* is even higher at 7 nm for H_2O ripple samples, and almost no features at the relevant length scale l_{cap} could be determined, which confirms the visual impression from Figure 5.1c4. Interestingly, l_{acc}, *mode* and *skewness* have essentially the same values for both types of bumpy structures; thus, the nanoscale topology of these samples can be considered identical.

5.4.2 Surface chemistry

The surface chemistry of the samples was analysed by XPS and EDX. Machining of titanium samples in pure oxygen leads to a surface solely consisting of TiO_2, while machining in nitrogen results in a mixture of TiO_2 and TiN (Lehr, de Marchi et al. 2014). Furthermore, XPS analysis on H_2O ripple surfaces showed that these consist of TiO_2. Table 5.2 shows the respective chemical surface composition of the five laser machined samples and the non-machined Ti control. The chemical states were quantified using a peak fitting process (Lehr, de Marchi et al. 2014), and the resulting data illustrates that the surface chemistry is comparable across the control samples and the samples machined in oxygen and water. However, the samples machined in nitrogen show less TiO_2 but more TiN and oxidized TiN. Furthermore, the relative shares found on N_2 bumpy samples are six times larger than those on N_2 ripple samples.

Table 5.2: Relative shares [%] of TiO_2 and TiN from XPS analysis.

machining environment	**O_2**	**N_2**	**H_2O**	**O_2**	**N_2**	**Ti**
structure	**ripple**	**ripple**	**ripple**	**bumpy**	**bumpy**	**control**
TiO_2	99	91	99	99	43	99
TiN	<1	4	<1	<1	25	<1
TiN oxidized	0	5	0	0	32	0

EDX surface mapping was additionally performed on all types of samples, since XPS does not provide enough spatial information about the distribution of the chemical species on the surface. Figure 5.3 shows the maps of the three relevant elements (titanium [Ti], oxygen [O], and nitrogen [N]) for the case of N_2 bumpy structures (More maps in Appendix C). N_2 bumpy samples are of particular interest due to their large share of TiN (Table 5.2). It can be seen from the magnified part of the maps in Figure 5.3 that the distribution of the species Ti and O follows the same surface pattern as seen on the SEM image, while this is not the case for the species N. This can be explained by the fact that EDX reaches up to 10 µm below the surface, which is similar to the vertical dimension of the bumpy features so that the Ti and O maps reflect the surface topology. Nitrogen, however, seems to be predominantly located on top of the bumpy features since the surface pattern do not appear on the map (see enlargement at 400nm).

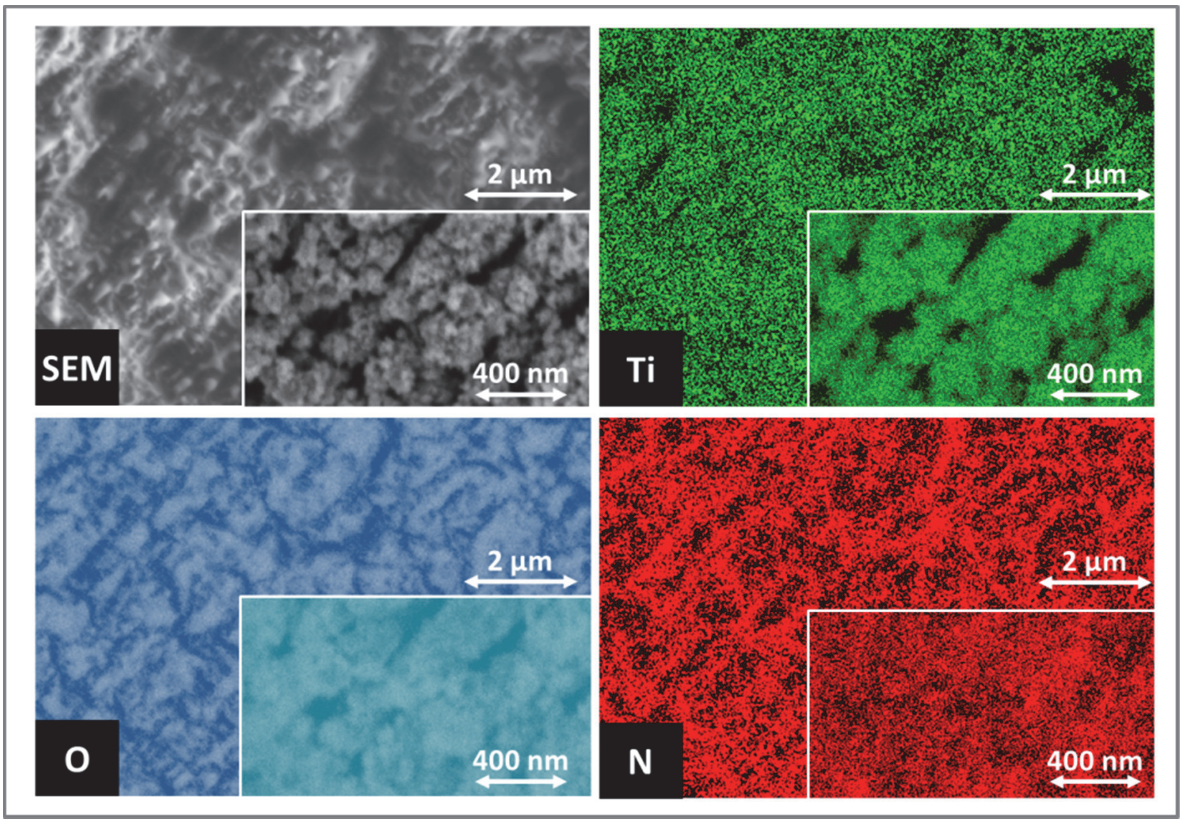

Figure 5.3: SEM image and the respective EDX maps obtained on N_2 bumpy samples.

Image analysis was applied on the EDX maps to obtain the necessary information on the nanoscale to further correlate the chemical surface composition with the formation of capillary bridges. The concept of *lacunarity*, which has its origin in fractal analysis (Mandelbrot 1983), was chosen for image analysis. Here, lacunarity represents the distribution of chemical species across the sample. Large lacunarity values indicate a non-uniform distribution. Table 5.3 shows lacunarity values obtained from the EDX maps for all samples for the four chemical species. Oxygen is least uniformly distributed compared to the other species, which can be attributed to thickness of the oxide layer. Interestingly, oxygen is less homogeneously dispersed on samples machined in oxygen than in the other cases, where oxygen originates from the oxide layer already present on the surface before machining. The distribution of nitrogen is uniform and does not depend on whether or not the samples were machined in a nitrogen atmosphere.

Table 5.3: Lacunarity values indicating the homogeneity of species distribution.

topology	Ti	O	N
O_2 ripple	1.07	4.14	1.25
N_2 ripple	1.09	2.82	1.36
H_2O ripple	1.00	3.17	1.30
O_2 bumpy	1.05	5.11	1.22
N_2 bumpy	1.07	2.10	1.36
average	**1.05**	**3.47**	**1.30**

5.4.3 Capillary force and humidity sensitivity

We follow the argument by Vogler (Vogler 1998) that surfaces exhibiting CAs > 65° can be considered as hydrophobic, since water between two surfaces exhibits characteristic self-cohesion only at measured adhesion values > 30 dyn/cm, which correspond to a CA > 65°. Thus, all micromachined samples in our study were hydrophobic based on their advancing CA (Table 5.4). The advancing CA for ripple samples is lower than for bumpy samples and only slightly higher than that of untreated titanium (Ti control). In general, hysteresis is relatively large, as seen from much lower receding CAs with respect to the advancing CAs.

Table 5.4: Advancing and receding contact angles for samples grouped by machining environment.

	O_2 ripple	N_2 ripple	H_2O ripple	O_2 bumpy	N_2 bumpy	Ti control
Advancing CA	82	94	85	114	128	73
Receding CA	48	56	61	72	96	54

The results from all force measurements with AFM are displayed in Figure 5.4, which indicate that the formation of capillary bridges depends on the type of sample surface. At 0 % RH the measured force was statistically independent of the machining environment and relatively constant across all laser machined samples with the exception of N_2 bumpy samples. The average force at 50 % RH and 70 % RH was smallest for O_2 ripple samples. Considering all ripple samples, the average force increased significantly only at 70 % RH. In contrast, on bumpy structures, the force increased already at 50 % RH. In general, all laser-machined samples showed a lower average force than the flat titanium and mica control samples. The statistical error was large on all samples (Figure 5.4a), which is explained when considering the extent of the maximum force (Figure 5.4b) measured during retraction of the probe.

The coefficient of variation (Figure 5.4c) was calculated based on the average force data to normalize the standard deviation and to investigate whether the error depends on the sample type and/or the humidity level. No trend is seen for ripple samples; however, the normalized error seems to increase with relative humidity on bumpy samples. The average force during dwell (Figure 5.4d) was constant for all samples and humidity levels. Thus, we can assume that the forces measured during the retraction of the AFM probe are capillary forces (Rabinovich, Singh et al. 2011). Interestingly, the force during dwell was significantly larger at 0 % RH for N_2 bumpy structures than for all other samples.

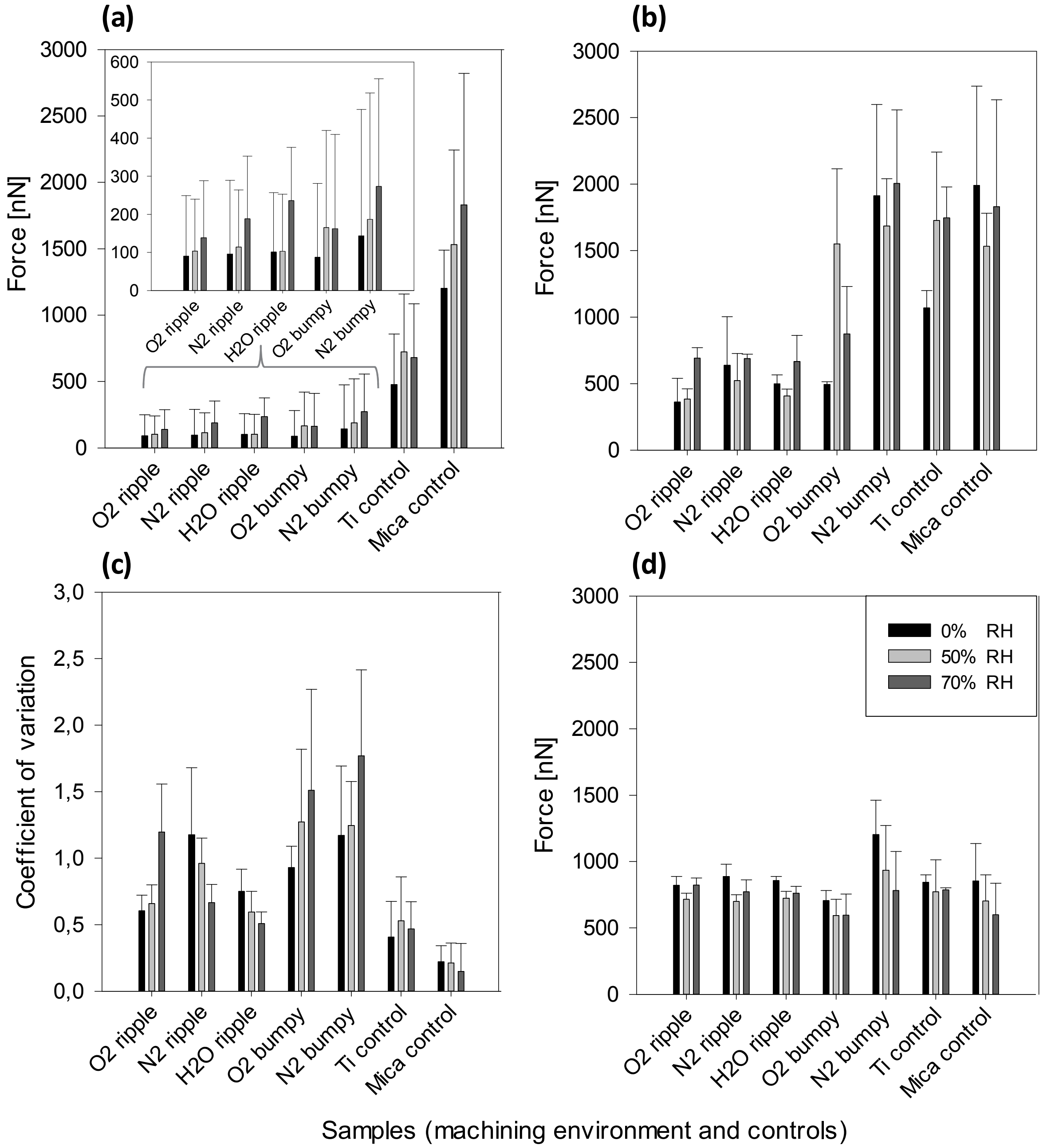

Figure 5.4: Average (a) and maximum (b) force during retraction (or pull-off) from the surface, coefficient of variation (c), and the average force during dwell (d). All machining environments are significantly ($P < 0.05$) different regarding average and maximum force from all other environments and the controls.

The sensitivities S_{50} (50 % RH) and S_{70} (70 % RH) were calculated from the average force data (Figure 5.5a) and the maximum force data (Figure 5.5b) with (Eq. (5.3)) for all machining environments and the control samples. S_{50} is smallest for O_2 ripple samples compared to all other samples machined in gas environments, whereas the H_2O ripple sample shows even lower sensitivity at 50% RH (Figure 5.5a). However, this is only true for the sensitivity calculated from the average force. For the sensitivity calculated from the maximum force only bumpy structures show significantly higher sensitivity than O_2 ripple samples (Figure 5.5b).

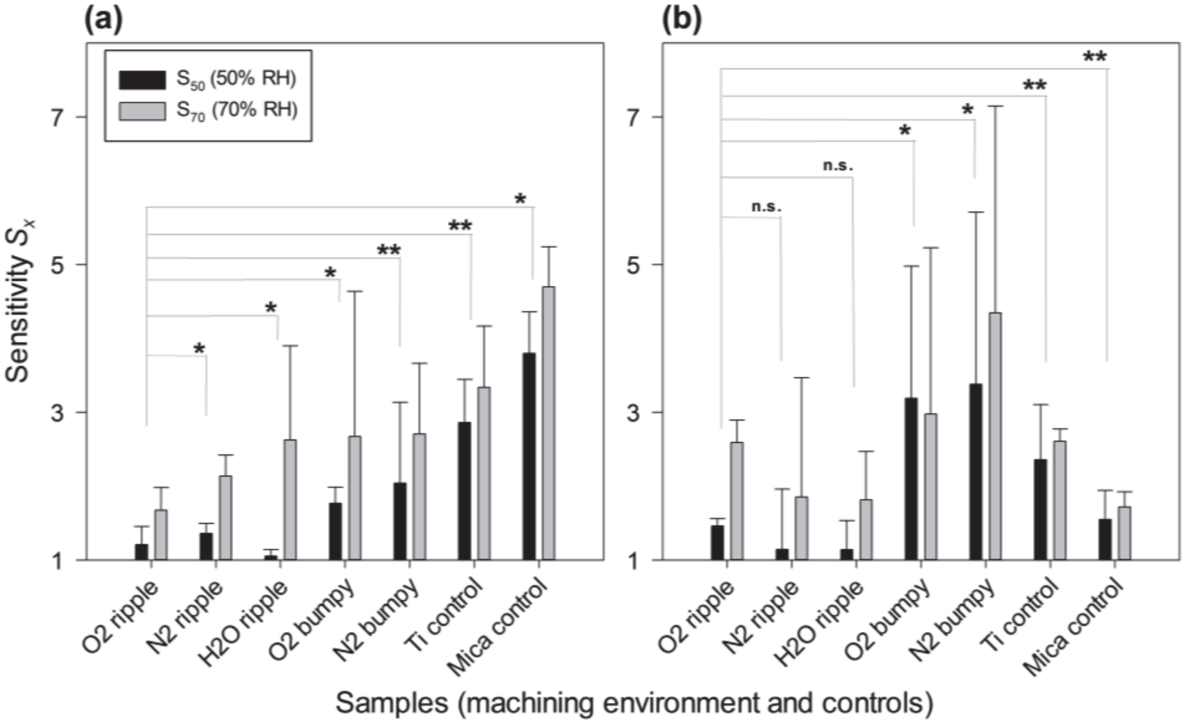

Figure 5.5: Humidity sensitivity for average (a) and maximum (b) force measured on all samples. S_x is smaller for O_2 ripple compared to all other samples: *=$P < 0.05$; **=$P < 0.05$ only for 50 % RH; n.s. = not significant. S_x=1: No influence of relative humidity.

5.5 Discussion

In the following, the wetting behavior, the total extent of the capillary force, its variation (statistical error) and the sensitivity (S_x) will be linked to the topological and chemical properties of the micromachined surfaces. Thereby, we will first address the matter from a nanoscopic perspective, at which nucleation and growth of capillary bridges take place (Butt and Kappl 2009). After, the difference between ripple and bumpy structures will be explained from a microscopic perspective.

5.5.1 Nanoscopic perspective

It is expected that one (Figure 5.6a1) or more (Figure 5.6a2) capillary bridges arise between the colloidal AFM probe and the sample's nanoscale surface features (4th column in Figure 5.1), which are of the order of l_{cap} (Ando 2004, Ando 2008).

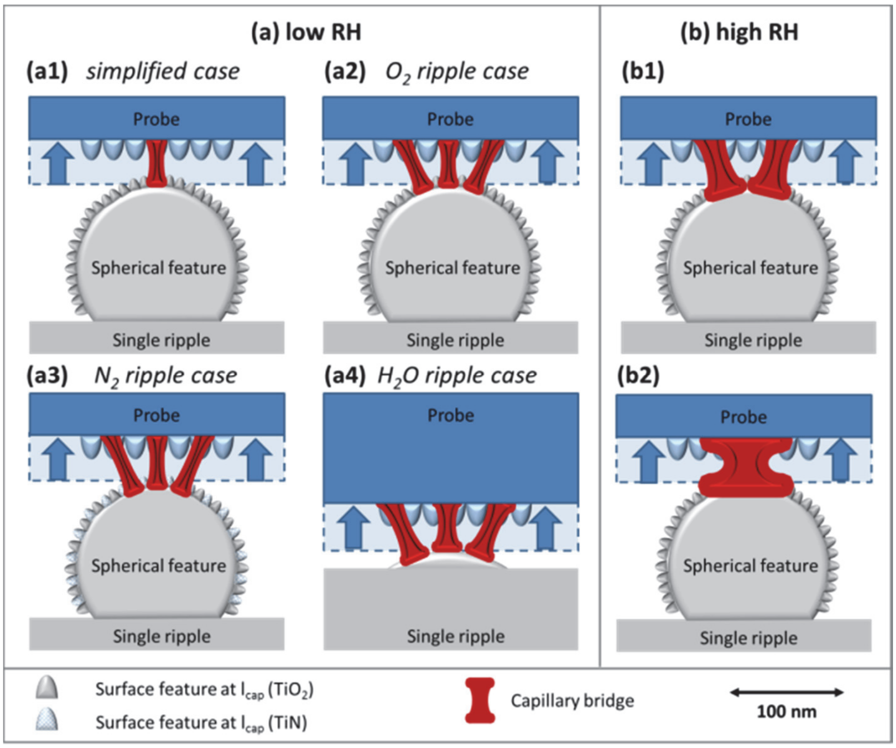

Figure 5.6: Nanoscopic interaction regimes between AFM probe and surface at low (a) and high (b) RH. The height of the capillary bridges is exaggerated to improve clarity of the figure.

If we exemplarily consider the force resulting from a single capillary bridge under extreme experimental conditions (see Appendix C for details), we find it to be below 10 nN. Now considering the magnitude of the capillary forces measured in this study (Figure 5.4a and Figure 5.4b), we conclude that these forces have to originate from multiple capillary bridges. The scenarios in Figure 5.6a2 to Figure 5.6a4 aim to illustrate the extent of capillary forces on the three ripple type samples and the similar nanoscopic topology of O_2 bumpy and N_2 bumpy structures (4th column Figure 5.1).

O_2 ripple type samples provide the best combination of surface chemistry and topology to achieve the lowest capillary force (Figure 5.4) and sensitivity S_x (Figure 5.5) compared to all other samples including the controls: The surface is chemically homogeneous consisting of TiO_2 (Table 5.2), and 42 % of the nanofeature dimensions are of the order of l_{cap} (Figure 5.2), where the roughness reduces the possible number of the capillary bridges formed (Ata, Rabinovich et al. 2002, Butt and Kappl 2009, Wallqvist, Claesson et al. 2009). The interaction between O_2 ripple type samples and the colloidal AFM probe is described by Figure 5.6a2.

Even though the surfaces of H_2O ripple samples are chemically identical to O_2 ripple samples (Table 5.2), these surfaces exhibit more capillary force than O_2 ripple samples. Capillary condensation is not hindered on H_2O ripple samples, since their roughness is not at the required length scale l_{cap}, (Figure 5.2) so that the interaction with the AFM probe corresponds to the scenario in Figure 5.6a4. Hence, the capillary force per single bridge is also larger than on O_2 ripple samples (see calculation in Appendix C and (Butt and Kappl 2009)).

N_2 ripple samples show also larger capillary forces than O_2 ripple samples, particularly at 70 % RH (Figure 5.4a), although N_2 ripple samples have a similar share of l_{acc} as O_2 ripple samples (Figure 5.2). This observation is explained by the higher surface energy of 1.1-5.6 J/m^2 for TiN compared to 0.06-0.08 J/m^2 for TiO_2 (Wypych). Consequently, the nanoscopic contact angle is smaller on the chemically inhomogeneous TiN/TiO_2 surface than on the TiO_2 surface, and therefore capillary forces are larger. Furthermore, the EDX maps and the lacunarity values (Table 5.3) confirm the existence of wetting gradients between spots of TiO_2 and TiN that promote capillary condensation (Gu, Chen et al. 2008). Thereby, EDX maps indicate that TiO_2 and TiN are equally distributed on the surface at the relevant length scale of the order of l_{cap} as illustrated in Figure 5.6a3.

O_2 bumpy and N_2 bumpy samples show a similar surface topology on the microscale (Figure 5.1) as well as at the relevant nanoscale l_{cap} (Figure 5.2). Hence, the presence of TiN (25 %) on the surface of the N_2 bumpy samples (Table 5.2) has to be responsible for the higher maximum force (Figure 5.4b) and the greater sensitivity (Figure 5.5) of N_2 bumpy structures compared to O_2 bumpy structures, like it is the case for the respective ripple structures.

The increase of capillary force with humidity is explained with the appearance of capillary bridges (Figure 5.6b) at RH > 50 %: More water condensates and capillary bridges grow to a larger volume with increasing radii (Figure 5.6b1), which results in larger capillary force (see calculation in Appendix C and (Butt and Kappl 2009)). This is especially true, when the entire volume between the colloidal probe and the nanoscale features on the micromachined surface is completely filled with liquid (Figure 5.6b2). Capillary forces on bumpy structures are particularly affected by increasing RH due to the larger interaction zones, which explains the high sensitivity S_{50} and S_{70} calculated from the maximum force in Figure 5.5b.

5.5.2 Microscopic perspective

The dimensions of the surface features of ripple and bumpy structures are very different on the microscale (1st column in Figure 5.1), which has an immediate impact on the capillary force and the apparent contact angle of ripple and bumpy samples. The relatively high advancing CAs of above 100° on bumpy samples could be explained with the existence of a Cassie wetting state (Table 5.4). The relatively small receding CAs and the large hysteresis in our study indicate that the Cassie state is not the predominant state, and that the surface is intrinsically hydrophilic, as expected considering the surface chemistry (Extrand 2003). Conversely, the microstructure does not determine the wetting state on the nanoscale, where capillary bridges are formed, since we can assume complete wetting analogous to the Wenzel state for a chemically uniform surface (Butt and Kappl 2009). Therefore, the high capillary force on bumpy structures must be explained with the additional available area for the formation of capillary bridges that is provided by the microscopic roughness. Thus, the microscopic and the nanoscopic perspectives have to be combined to explain the results for bumpy samples, since nanoscopic features are found on top of the microscopic bumps (2nd column in Figure 5.1).

Figure 5.7a1 and Figure 5.7a2 show the microscopic situation (magnified from Figure 5.6) for the interaction between the colloidal AFM probe and a sample covered with ripple structures. Due to the different length scales of the colloidal probe and the ripples, only one contact zone has to be considered, which is the fundamental difference to bumpy structures. The actual number of capillary bridges formed in the contact zone then depends on the nanoscopic conditions (Figure 5.6).

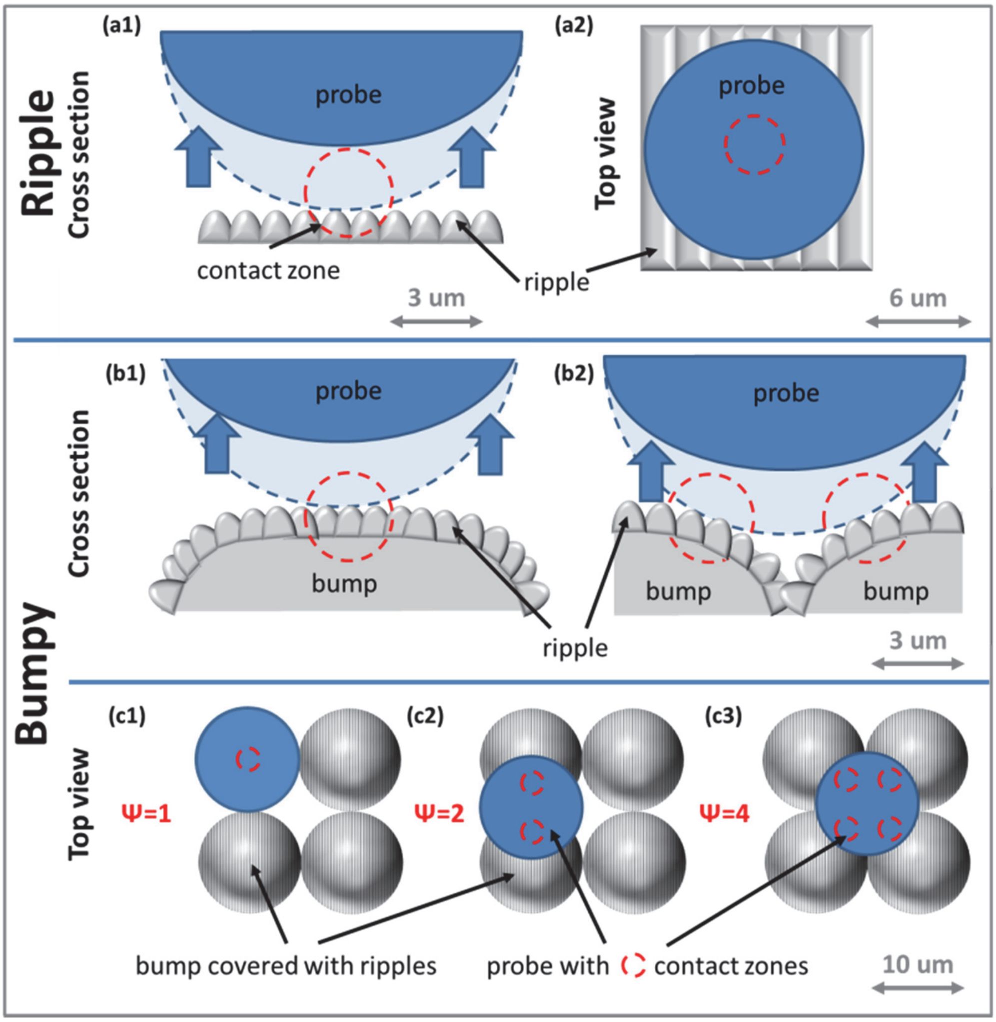

Figure 5.7: Microscopic interaction regimes and factor ψ between the AFM probe and the surface for ripple and bumpy structures.

Figure 5.7b and Figure 5.7c illustrate that the difference between ripple and bumpy structures originates only from the possible number of contact zones. The similarity in the diameter of the colloidal probe and a single bump leads to the geometric situations in Figure 5.7c1 - c3. The number of contact zones results in a geometric factor ψ that can be multiplied with the number of capillary bridges per contact zone that arise on the nanoscale (Figure 5.6). The factor ψ serves to explain the difference between ripple and bumpy structures of the same surface chemistry and nanoscopic roughness. Indeed, the force data in Figure 5.4b indicate that for O_2 and N_2 bumpy samples the capillary force is four times larger than on the respective ripple samples with respect to the maximum force. The scenario in Figure 5.7c3 with $\psi = 4$ explains the data in Figure 5.4b. However, since the average force values in Figure 5.4a are only twice as large for bumpy samples compared to the respective ripple samples, we can assume that the scenario in Figure 5.7c2 with $\psi = 2$ represents a typical geometric situation that led to the average forces measured in this study. Hence, the scenario depicted in Figure 5.7c3 has to be considered as a rare event.

The sensitivity S_x (Figure 5.5a) serves to determine the geometric scenario and the factor ψ more precisely: The sensitivity S_{50} on bumpy samples was 1.5 times larger than on the respective ripple samples, and likewise was S_{70} 1.6/1.27 times (O_2 bumpy/N_2 bumpy samples, respectively) larger. Consequently, we can assume that ψ is actually rather around 1.5 and independent of the RH level. Furthermore, the force F_0 is similar for ripple and bumpy samples (Figure 5.4a) so that there is no purely numerical influence of the reference force value at F_0 on the S_{50} and S_{70} values. Hence, ψ can be assumed to be characteristic for the additionally available area for the formation of capillary bridges on bumpy samples compared to ripple samples.

5.5.3 Correlation between contact angles and capillary force

In the previous sections we showed that the extent of capillary forces and the sensitivity of micromachined samples can be explained with the nanoscopic and microscopic surface topology of the samples as well as with the different surface chemistry, which all depend on the machining environment. However, the influence of the exposure environment on the formation of capillary bridges has still to be discussed particularly in context of the apparent CA. Figure 5.8 displays the advancing and receding CA data together with the force data for each combination of machining environment and exposure environment from the same measurements as used in Table 5.4. No correlation between the type of exposure environment and the extent of the force or between the advancing CA and the force could be observed (Figure 5.8a). However, it can be seen that the receding CA and the capillary force at 50 % RH correlate for the N_2 and H_2O ripple and the O_2 bumpy samples (Figure 5.8b). Interestingly, the contact angles were measured in the laboratory at 40 to 50 % RH. This correlation is in agreement with earlier reports highlighting the relation between capillary force and wettability (Truong and Wayner 1987, Quon, Ulman et al. 2000).

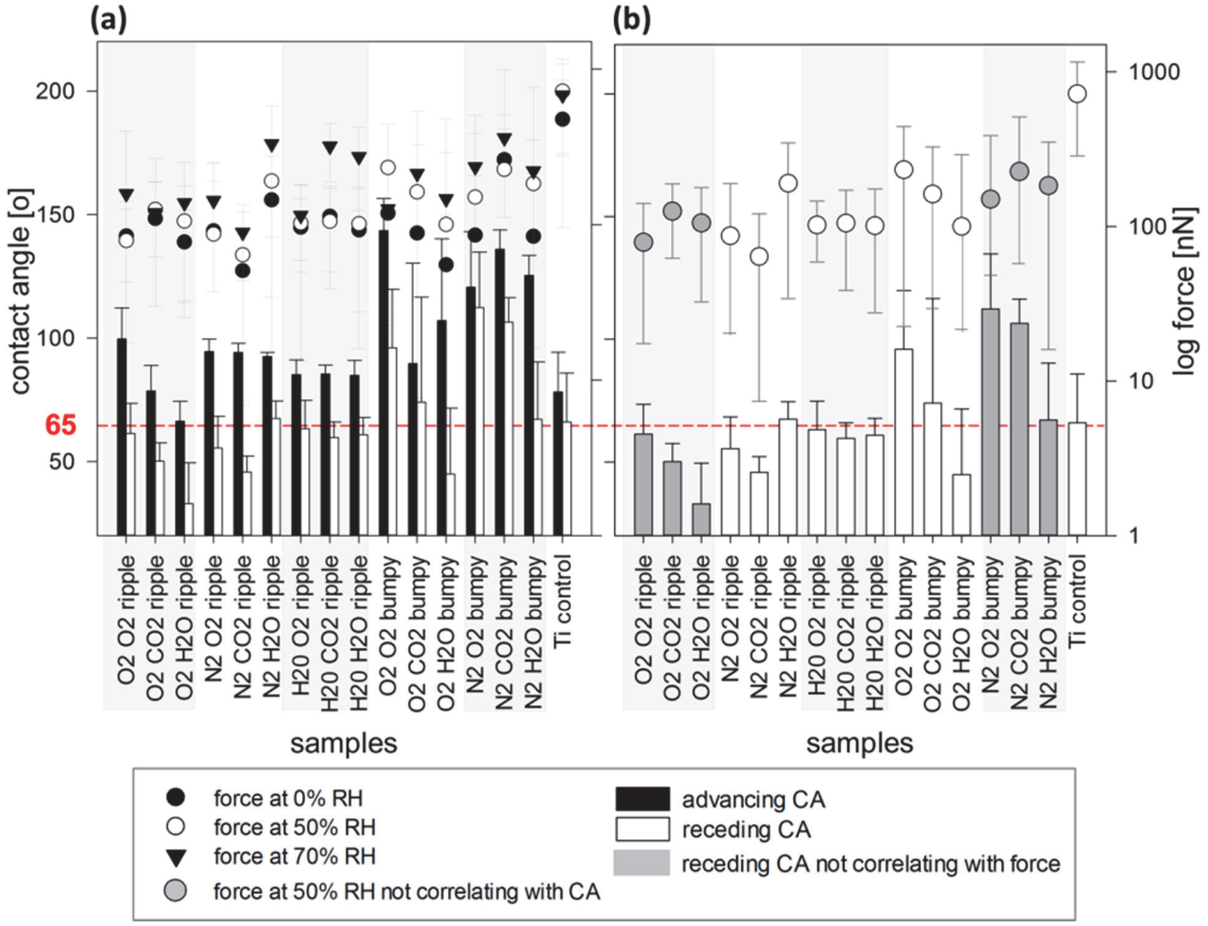

Figure 5.8: ARCA and force data for all samples grouped by the machining environment (a). Receding CA and force data at 50 % RH for all samples grouped by the machining environment (b). All treatments (exposure) within one machining environment have significantly different force levels ($P < 0.05$). Mica is not displayed since no ARCA could be obtained due to mica’s strong hydrophilic behavior.

Furthermore, the variations of contact angle and force within a group of samples from the same machining environment indicate an alteration of the surface chemistry caused by the exposure step. After many researchers have tried unsuccessfully to link the surface chemistry to the wetting behavior of micromachined metals after exposure to air (Jagdheesh, Pathiraj et al. 2011, Kruse, Anderson et al. 2013, Anderson, Wilson et al. 2014, Gökhan Demir, Furlan et al. 2014), the observed correlation provides some evidence for an influence of the exposure environment on the surface chemistry. Due to the fact that EDX is a near surface technique it did not serve us to deliver any information about the difference between samples from the same machining environment that were exposed to O_2, CO_2 or H_2O (see Appendix C). Furthermore, neither XPS nor EDX disclose the origin of the elements. This is of particular importance in the case of oxygen, where it is not known, which share originates from the surface oxide layer that existed before micromachining, and which share originates from the oxygen in the machining environment. This problem must be addressed in future research in order to achieve a complete understanding of the mechanism of contact angle alteration on micromachined surfaces.

5.6 Conclusions

Femtosecond laser micromachining on titanium surfaces in a controlled environment allows the simultaneous modification of the surface topology and the surface chemistry. We have shown that both the wettability and the formation of capillary bridges are altered. The concept of humidity sensitivity was introduced. It permits quantifying the increase of the total surface force with increasing capillary force at higher relative humidity. The data in our study suggests a level > 50 % RH at which the influence of the relative humidity on the formation of capillary bridges becomes relevant. This finding is in good agreement with the threshold at 35 % RH, which was identified in previous studies (Sedin and Rowlen 2000, Rabinovich, Singh et al. 2011).

We conclude that two surface properties have to be adjusted to minimize capillary force and sensitivity. Firstly, the surface chemistry must be uniform. Secondly, the dimensions of features present on the surface features at both the microscale and the nanoscale must be controlled. Micro-roughness must be avoided, and the number of nanoscale features at the length scale between 0.5 and 5 nm has to be maximized. We were able to fulfill these two requirements with ripple structures machined in a pure oxygen environment.

Further, we contribute to the general understanding of the formation of capillary bridges on a rough surface with different degrees of wettability. The surface topology both on the microscale and on the nanoscale ultimately determines the extent of capillary force. The surface chemistry seems to only play a minor role for a rough surface. Interestingly, we see the same dominance of the surface topology over chemistry for the formation of capillary bridges as it is known for the wetting behavior of a rough surface (Marmur 2004). The observed correlation between the receding contact angle and the capillary forces at 50 % RH for several types of samples gives more evidence that the exposure to O_2, CO_2 and H_2O alters the surface wettability.

Acknowledgment

This research has been supported by the National Science and Research Council (NSERC) of Canada through a Discovery Grant to A. Kietzig. We thank Nicolas Brodusch of Prof. Raynald Gauvin's laboratory in the Dep. of Material and Mining at McGill University for the high-resolution SEM images and the EDX maps. We also thank to Fabrizio De Marchi from the Institut National de la Recherche Scientifique (INRS) in Varennes, QC, Canada for the XPS analysis.

References

Please refer to the global bibliography at the end of the thesis.

Chapter 6

6. Conclusions

6.1 Summary

The overall goal of this thesis was to understand how to control two aspects of the interaction between a femtosecond laser with a solid metallic or surface: the formation of an array of homogeneous microstructures, and the resulting chemical composition of the surface after exposure to a specific environment during and after the laser machining process. The experimentally obtained surfaces were then investigated with SEM, XPS/EDX, contact angle geometry and colloidal AFM to link surface topology and chemistry with wetting behavior and capillary adhesion.

The experimental parameters were identified that allow micromachining of a homogeneous array of microstructures as these are required for reproducible contact angle measurements and possible application of micromachined surfaces. The accumulated input intensity on a moving sample $I_{pulse\text{-}accumulated}$ and the line-overlap (φ_{line}) between two subsequently raster scanned lines were chosen as independent variables, while the pulse overlap (φ_{pulse}) was held constant. The experiments were conducted in air at constant pressure on polished titanium sheets. The two independent variables were varied over a large range to identify threshold values for the formation of microstructures and to achieve homogeneity. These experiments were combined with numerical simulations to understand, whether the accumulated intensity profiles have to be flat to obtain homogeneous microstructures. In the course of these experiments, the experimental settings to produce two types of microstructures, pillow-like and bumpy, were identified. In the case of both types of structures, homogeneous arrays were obtained. It was found that the two types of microstructures originate from two different ablation regimes, since only in the case of pillow-like structures a flat intensity profile was required.

Micromachining experiments in different gas environments were conducted to explore, whether the surface chemistry of the samples could be altered to fine tune the surface's wettability while keeping the topology unchanged. Topographical imaging with SEM showed that the surface morphology of samples machined in pure oxygen, nitrogen and helium were significantly different from the samples machined in air while all other experimental parameters were kept constant. The production of nano-particles and their agglomeration during the machining process was found to be ultimately responsible for the dependence of the structure formation on the gas environment. The cloud of particles formed in front of the machining area renders the optical properties of the environment non-isotropic so that the effective intensity I_{eff} was altered.

Contact angle goniometry was combined with colloidal AFM to determine the magnitude of capillary forces on the previously micromachined surfaces, and to investigate wettability on the nanoscale. Ripple structures machined in pure oxygen were successfully identified to provide a minimal extent of capillary forces with limited sensitivity to an increase of the relative humidity in the environment. Nanoscale roughness on the relevant length scale and a homogeneous surface chemistry hinder the formation of capillary bridges on such a surface. Furthermore, the observed correlation between the receding contact angle and the capillary forces at 50 % RH provides some evidence that the exposure environment does have an influence of the surface chemistry.

All objectives of this thesis have been successfully achieved: The relevant parameters to produce homogeneous micro- and nanostructures on titanium surfaces were identified. The role of the gas environment during femtosecond laser micromachining was quantified. Finally, the relationship between surface topology, surface chemistry, wettability and capillary forces on femtosecond laser micromachined metallic surfaces was determined.

6.2 Statements of contribution

The research throughout this dissertation has resulted in the following contributions to the field of femtosecond laser micromachining on metallic surfaces:

1. The successful identification of the relevant experimental parameters allows producing homogeneous arrays of microstructures with femtosecond laser irradiation in a raster line scanning process.
    - $I_{pulse\text{-}accumulated}$ and φ_{line} are the key parameters to control homogeneity of micromachined arrays of structures.
    - An even intensity distribution across the sample is not required to achieve homogeneity since the particular ablation regime governs the formation of microstructures.
    - Controlling φ_{line} allows using the intensity accumulation effect in the material to achieve homogeneity.

2. The exploration of the role of the surface chemistry on the formation of surface microstructures during femtosecond laser micromachining permits predicting the outcome of the machining process in different environments as well as to choose the gas environment according to their experiment goals.
    - Titanium nitride is deposited on a metallic surface when machined in a pure nitrogen environment.
    - The optical properties of the chemically altered surface and particles immediately change the level of the effective intensity on the target surface.

- The interactions between the femtosecond laser beam with the particle cloud was shown for the first time to be crucial for the magnitude of the effective intensity.

3. Femtosecond micromachined titanium surfaces covered with nanoscale ripple roughness and uniform surface chemistry serve well to minimize the magnitude of capillary adhesion and surfaces' sensitivity towards changes of the relative humidity in the environment. Hence, these surfaces qualify to be used by researchers and engineers in applications with uncontrolled environmental conditions, where adhesion originating from capillary forces has to be limited.
    - The relevance of the nanoscopic length scale l_{cap} of the roughness for the formation of capillary bridges has been confirmed. Furthermore, it was shown that l_{cap} applies also for the spatial distribution of chemical gradients on the surface.
    - The contribution of the macroscopic roughness to the adhesion force has successfully been described and quantified by a single geometric factor ψ.
    - The concept of humidity sensitivity has been successfully introduced and proven to expose the contribution of the capillary forces to the total surface force measured with AFM.

6.3 Recommendations for future work

The research on femtosecond laser micromachining and capillary forces measured with AFM presented in this thesis sets the foundation for different strings of future research.

6.3.1 Femtosecond laser micromachining

- The results on the influence of a nitrogen machining environment have to be used to understand the situation for a mixture of nitrogen and oxygen. In particular, it should be investigated which is the critical share of TiN that alters the effective intensity on the surface and the formation of capillary bridges. Gas mixtures with CO_2 present should also be studied to understand the situation in an uncontrolled environment of air and the phenomenon of contact angle evolution.

- The formation of TiN on the surface during micromachining in nitrogen showed that the chemical composition of the target surface can be modified via micromachining. This phenomenon should be further explored with other reactive gases containing species like sulfur. The incorporation of other chemical species would not only alter the wetting behavior but might also serve to develop catalytically active surfaces from femtosecond laser micromaching.
- Similarly, the incorporation of nitrogen into the surface and the resulting physical properties should be studied for other metals and alloys like copper or steel as well as for porous metallic and polymeric substrates.
- The chemical and physical aspects of the mechanism of contact angle evolution should be further investigated. The exposure to CO_2 for instance has to be quantitatively studied with gas absorption measurements and further measurements with high resolution XPS.

6.3.2 *Atomic force microscopy (AFM)*

- In this study the colloidal probe AFM measurements were obtained with constant material properties of the probe. However, to further understand the formation of capillary bridges in metallic surfaces, the type of probe should be varied. Changing the colloidal probe’s diameter would allow to verify the results from chapter 5 about the role of the microscopic roughness on the magnitude of the capillary adhesion. The preparation and use of a hydrophobic AFM probes would allow studying hydrophobic-hydrophobic interactions between two surfaces (Knapp and Stemmer 1999).

- Advanced AFM models like *freeze fracture* atomic force microscopy and in situ synchrotron SAXS could be used to investigate the micro- and nano-wettability (Wu, Cho et al. 2010) in detail. The contact angle evolution phenomenon could be further investigated with chemical force AFM and techniques like pulse-force mode or nanoindentation (Frisbie, Rozsnyai et al. 1994, Green, McDermott et al. 1995, Noy, Frisbie et al. 1995, van der Vegte and Hadziioannou 1997, Krotil, Stifter et al. 1999, Okabe, Furugori et al. 2000, Smith, Connell et al. 2003, Rodríguez and García 2004, Schönherr, Feng et al. 2005, Heyde, Kulawik et al. 2006, Sugimoto, Pou et al. 2007, Tokumoto, Ide et al. 2007). The results in chapter 6 already provided an outlook about the ability of AFM to detect chemical gradients on the nanoscale.
- Dynamic AM/FM-AFM measurements should be considered to explore the capillary force volume in a 3D scenario above the surface (Oyabu, Pou et al. 2006). Dynamic modes provide much better force resolution than contact mode AFM, which would allow obtaining detailed data about the variation of the surface properties across a wider area of the sample surface.
- Last but not least the application of lateral friction force AFM should be considered to determine the tribological properties of femtosecond laser micromachined surfaces on the nanoscale (Jinesh and Frenken 2006). Furthermore, the mechanical properties of the micromachined surfaces could be explored with AFM.

Appendix A: Supporting information for manuscript in Chapter 3

1. Examples for overexposed titanium surfaces

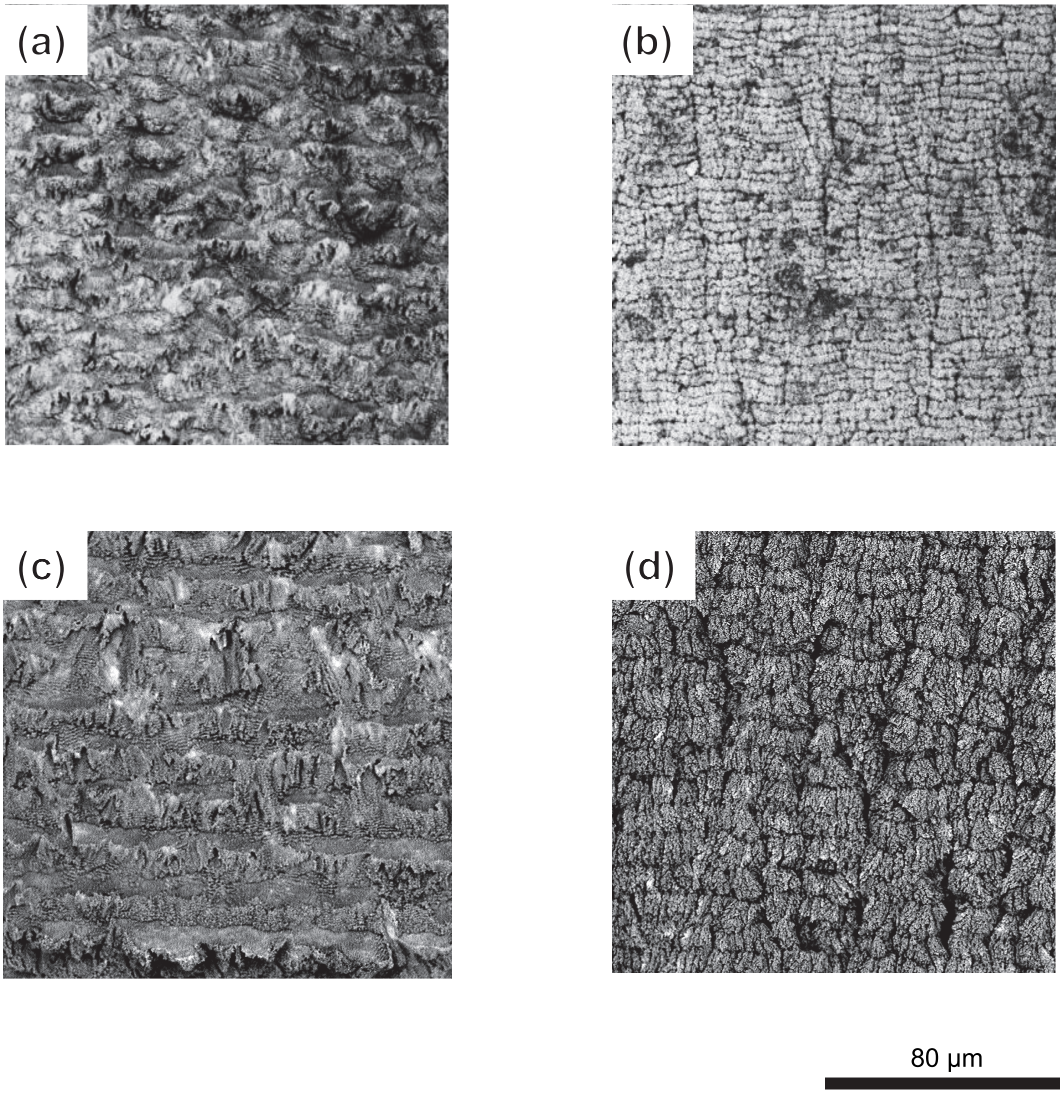

Figure A1: Examples for "overshooting" pillow like (a-b) and bumpy structures (c-d). (a): $\varphi_{line} = 90$ %, $I_{pulse\text{-}accumulated} = 1.2$ GW/m^2; (b): $\varphi_{line} = 90$ %, $I_{pulse\text{-}accumulated} = 2.4$ GW/m^2; (c): $\varphi_{line} = 70$ %, $I_{pulse\text{-}accumulated} = 4.8$ GW/m^2; (d): $\varphi_{line} = 80$ %, $I_{pulse\text{-}accumulated} = 4.8$ GW/m^2.

2. Examples for development of homogeneous arrays of pillow-like structures

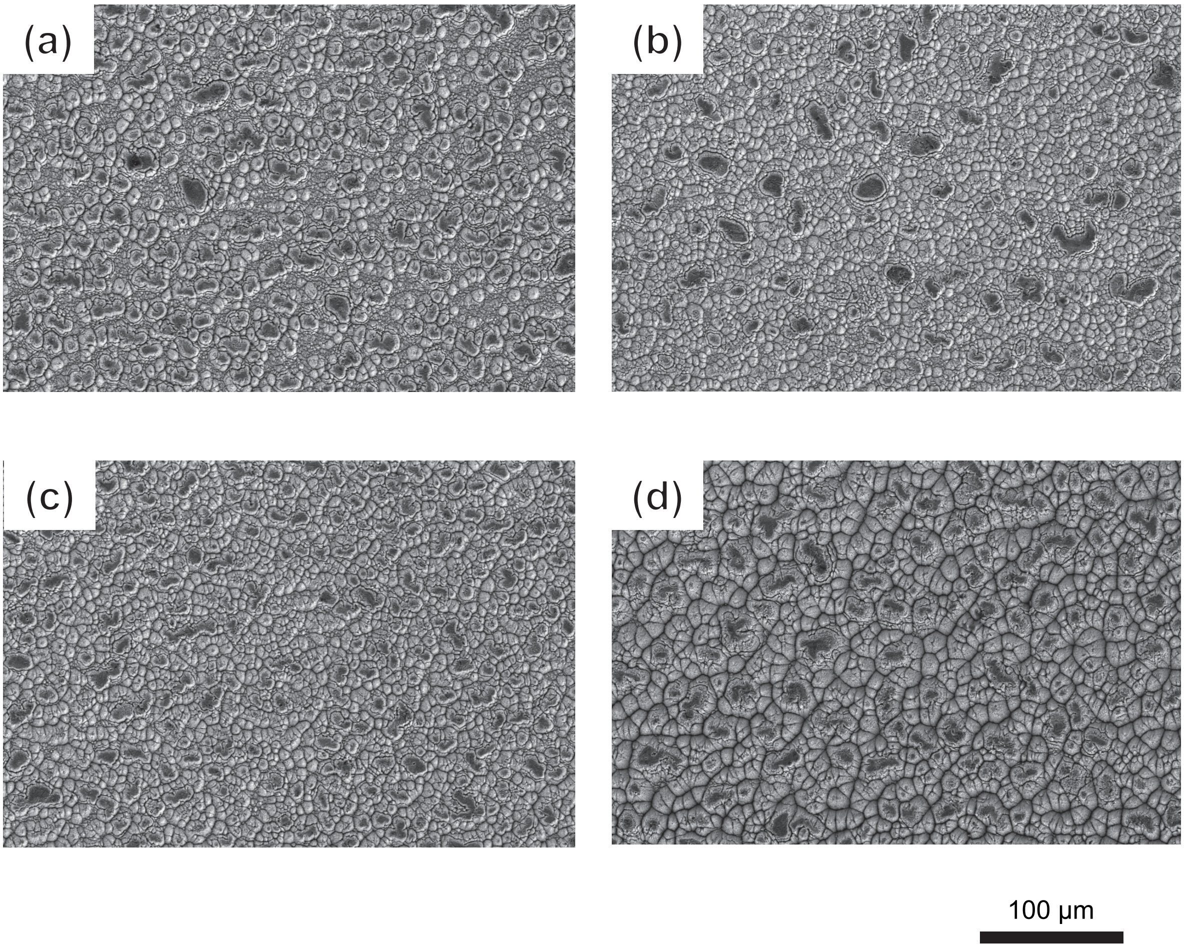

Figure A2: Formation of homogeneous patch for pillow-like structures at $I_{pulse\text{-}accumulated} = 1.2$ GW/m^2. (a): $\varphi_{line} = 76$ %; (b): $\varphi_{line} = 80$ %; (c): $\varphi_{line} = 84$ %; (d): $\varphi_{line} = 88$ %.

Appendix B: Supporting information for manuscript in Chapter 4

1. Intensity calculation: Accumulated pulse and line intensity

Intensity (I_0) (Eq. (A1)) is calculated as peak energy (in this case power (P)) over the beam area, which is determined from the beam diameter (ω). Eq. (A1) expresses the average intensity but not the intensity variation across a patch that constitutes of overlapping lines machined with a Gaussian beam.

$$\boldsymbol{I_0 = \frac{P}{\pi\left(\frac{\omega}{2}\right)^2}} \tag{A1}$$

Eq. (A2) quantifies the accumulated intensity ($I_{line\text{-}accumulated}$) at an arbitrary spot on a patch, depending on its position defined by the x, z coordinates.

$$\boldsymbol{I_{line-accumulated}\,(x, z, i_x, j_z) = I_0 exp\left(-2\left(\frac{\left(x+\frac{v_0}{f_p}i_x\right)^2+\left(z+\frac{v_0}{f_p}j_z\right)^2}{\left(\frac{\omega}{2}\right)^2}\right)\right)} \tag{A2}$$

The parameters i_x and j_z indicate the respective location and respective intensity level on the Gaussian distribution for the coordinates x and z. The repetition rate is stated by f_p and the scanning velocity by v_0. In the case of our experiments, Eq. (A2) has been modified to Eq. (A3) to allow distinguishing between the intensity input along a single machined line in x-direction and the total intensity exposure when lines overlap to form a patch.

$$\boldsymbol{I_{pulse-accumulated}(x, i_x) = I_0 exp\left(-2\left(\frac{\left(x+\frac{v_0}{f_p}i_x\right)^2}{\left(\frac{\omega}{2}\right)^2}\right)\right)} \tag{A3}$$

Throughout the experiments the intensity profile in *x*-direction was basically flat due to the high pulse overlap so that $I_{pulse\text{-}accumulated}$ can be substituted as a constant into Eq. (A2) to give Eq. (A4), which allows the calculation the total accumulated intensity $I_{line\text{-}accumulated}$ for overlapping lines on a patch.

$$\boldsymbol{I_{line-accumulated}(z, j_z) = I_{pulse-accumulated} exp\left(-2\left(\frac{\left(z+\frac{v_0}{f_p}j_z\right)^2}{\left(\frac{\omega}{2}\right)^2}\right)\right)} \tag{A4}$$

$I_{pulse\text{-}accumulated}$ and $I_{line\text{-}accumulated}$ are calculated numerically with a Matlab code. The code considers the number of overlapping pulses in *x*-direction for $I_{pulse\text{-}accumulated}$ and the number of lines (pulses) overlapping in *z*-direction. The intensities of every pulse are summed up respectively to their level at the portion of the Gaussian distribution that overlaps.

2. Particle size distribution of solutions shown in Figure 4.6 of main document

A ZetaSizer was used to determine the particle distribution of the three solutions of particles that were collected on the surface after machining shown in Fig. 4.6. The O_2He and the N_2He sample show a polydispersity index (PdI) below 0.5, while the HeHe sample has considered being polydisperse with a PdI above 0.5. Table A1 shows the average radius in nm for the particles by intensity, volume and number.

Table A1: Particle size distribution data for O2He, N2He and HeHe sample. The laser wavelength was 611 nm. The standard was polystyrene beads in deionized water.

	PdI	Intensity Mean (nm)	Volume Mean (nm)	Number Mean (nm)
O_2He	0.346	324	951	55
N_2He	0.408	343	1508	100
HeHe	0.688	286	299	272

Figure A3 shows the relative portions of the particles by number. In the case of O_2He and N_2He the dominating fraction is around 50 nm, while for HeHe larger radius around 300 nm dominates.

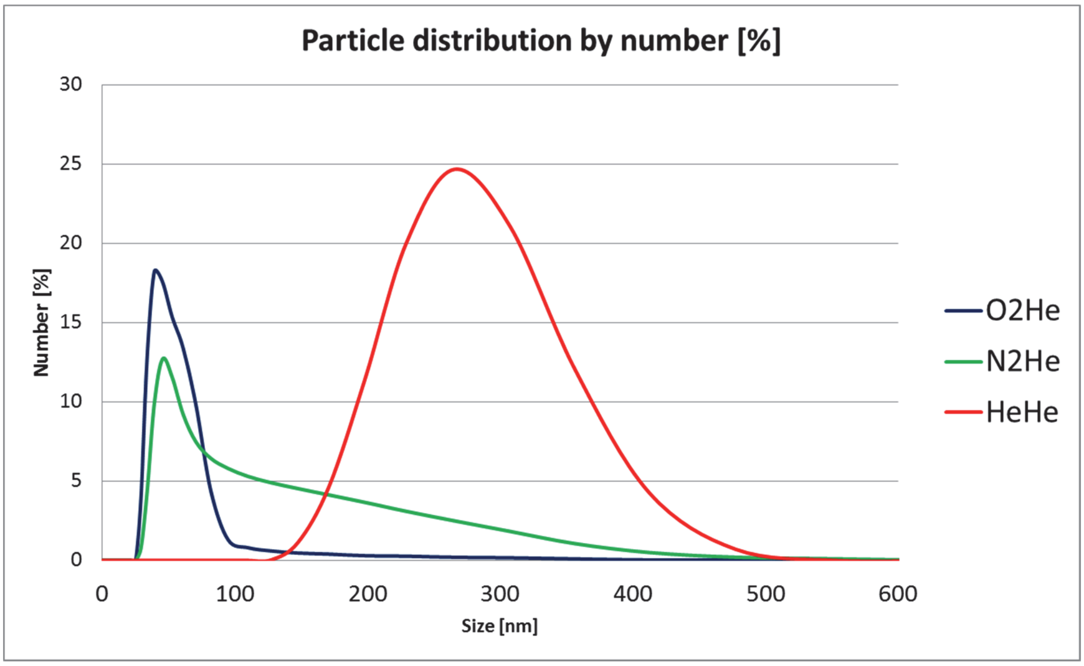

Figure. A3: Particle distribution by number for samples O2He, N2He and HeHe.

3. Detailed XPS spectra and data

XPS experiments were carried out in an ultrahigh vacuum (UHV) chamber with a base pressure of 10^{-10} mbar. A monochromatic Al source was used for all the analysis shown in this work. Before the analysis, the samples were rinsed in a ultrasonic bath of acetone to remove any particles left from the micromachining. Each of the spectra was calibrated by defining the position of the adventitious carbon peak to the known value of 284.6 eV. For each of the sample, a preliminary survey spectrum was obtained before high resolution spectra of the C 1s, O 1s, Ti2p and N 1s regions. All the spectra are reported in Figures SC 1-8. The spectra were acquired utilizing Avantage software, while data processing and peak fitting were achieved using CasaXPS software.

The particles removed by the micromachining process were suspended in the acetone solution used for rinsing, and were deposited on copper grids after evaporating the solvent.

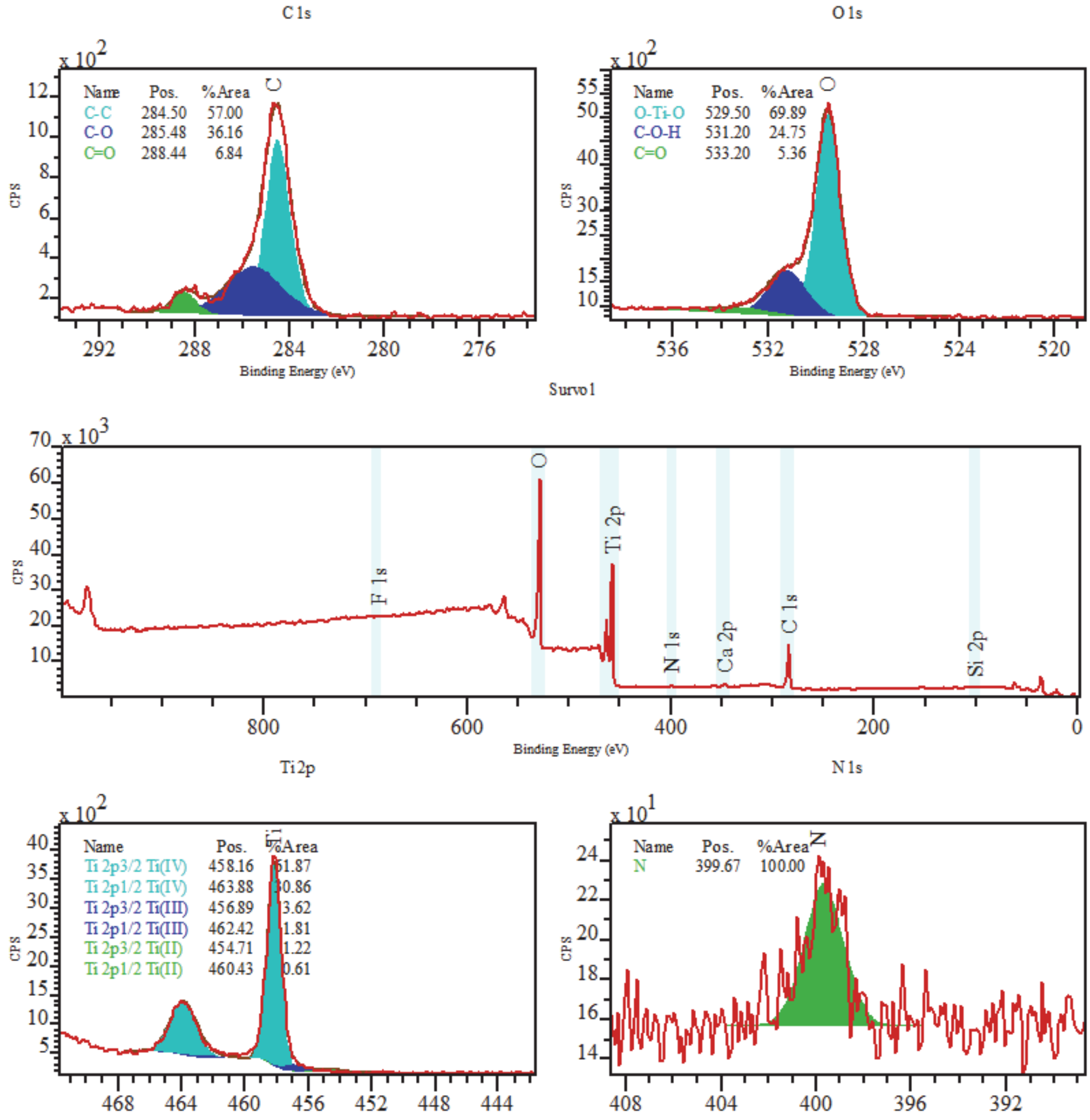

Figure A4: XPS spectra for O_2-He sample

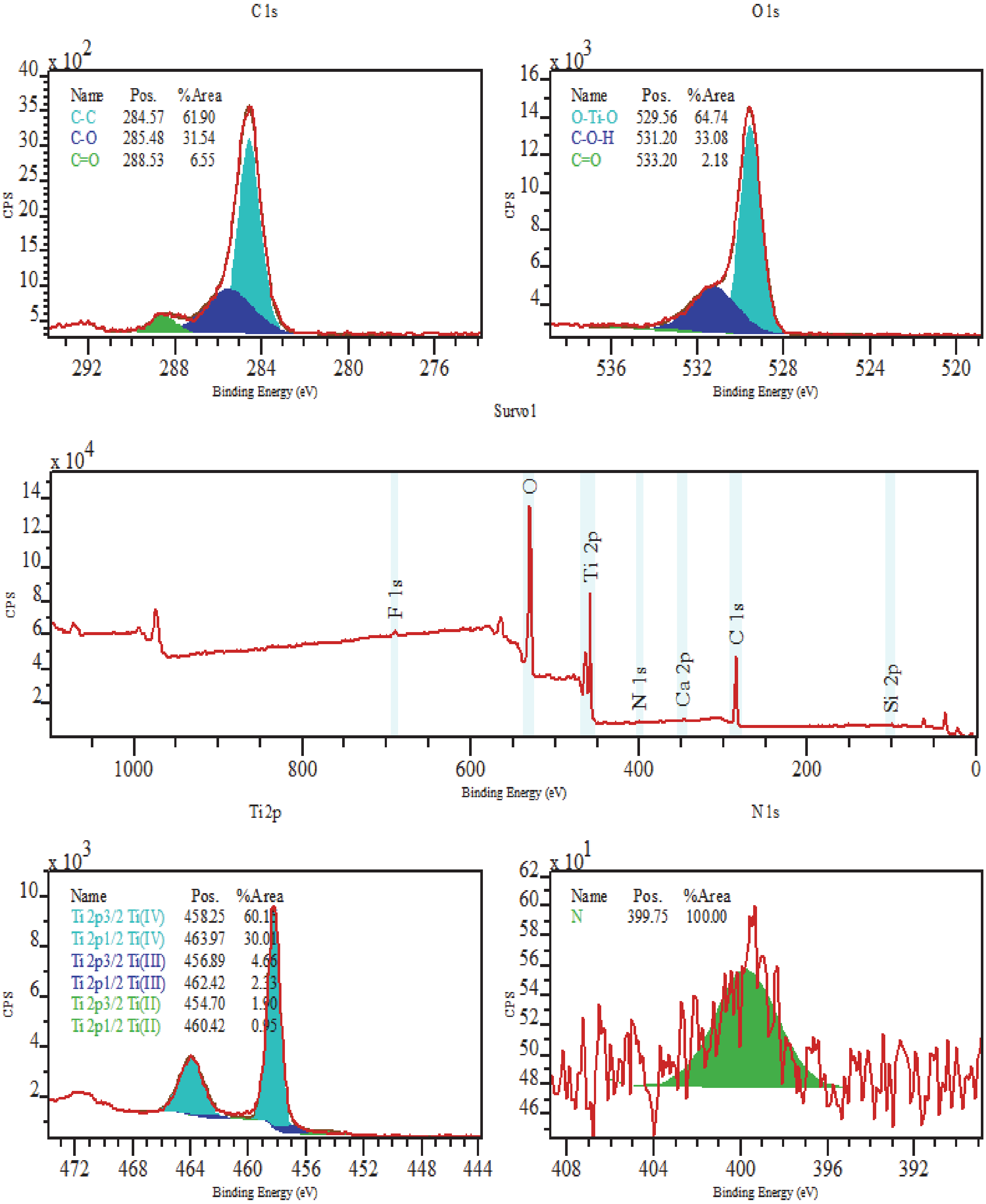

Figure A5: XPS spectra for O_2-N_2 sample

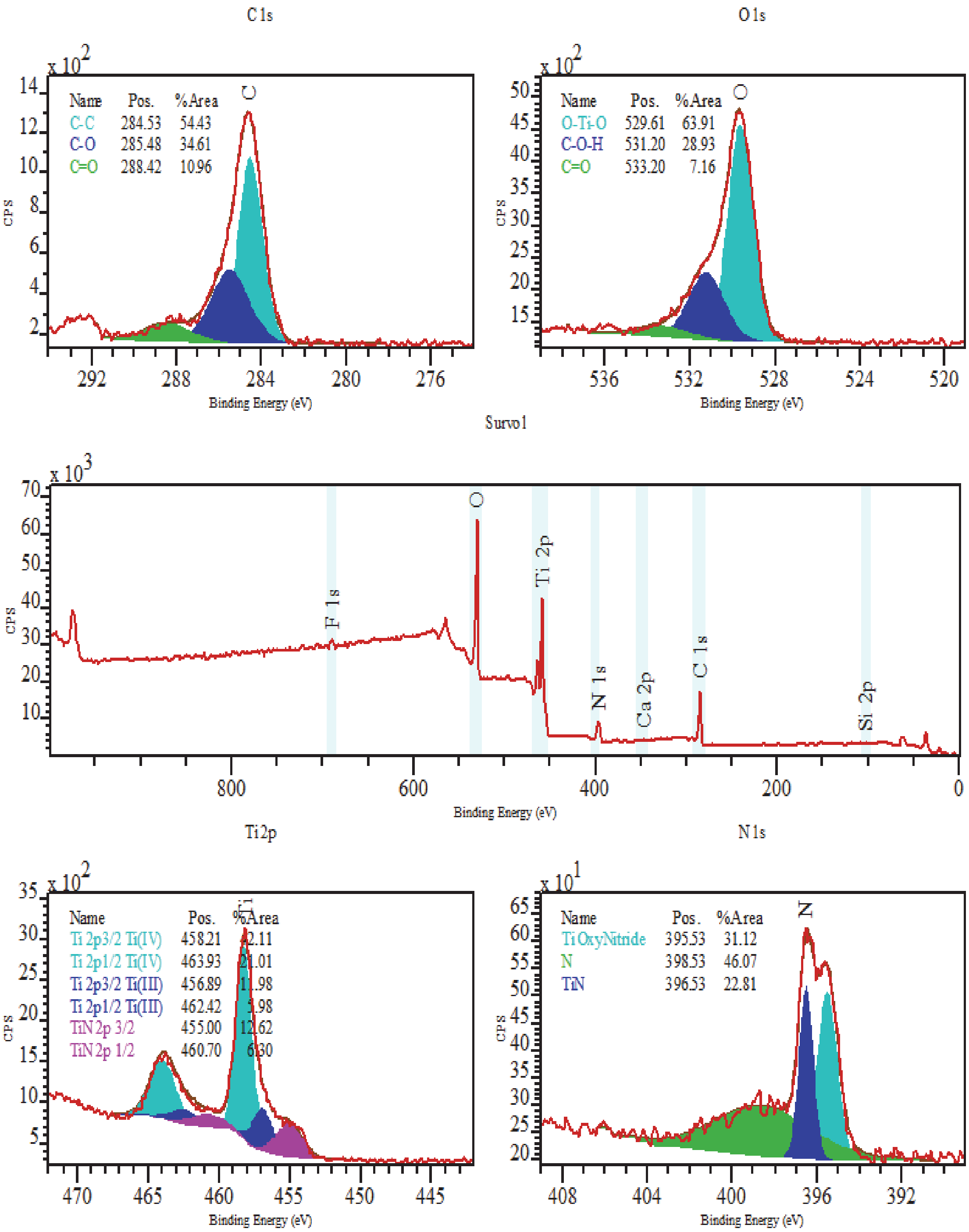

Figure A6: XPS spectra for N_2-O_2 sample

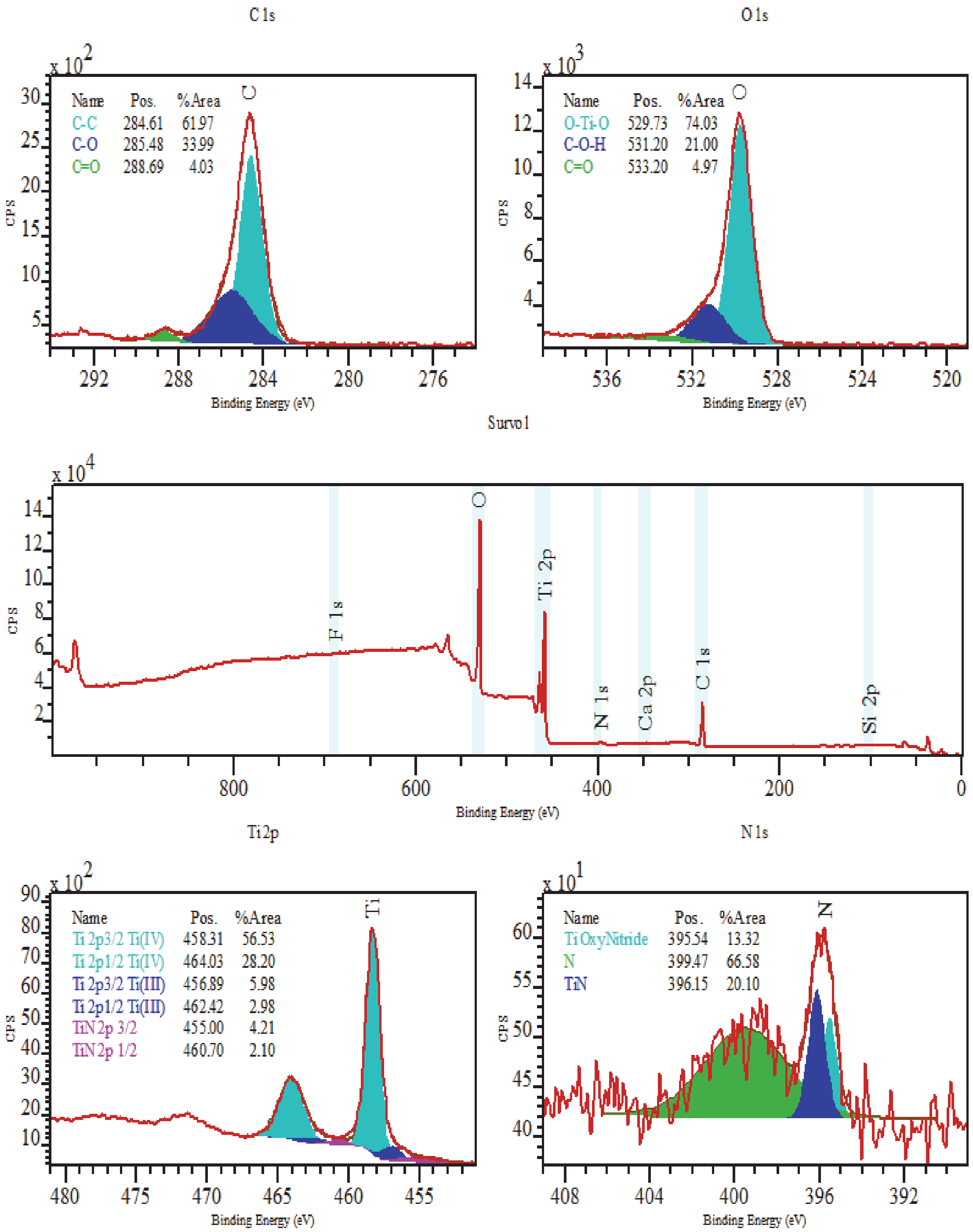

Name	Pos.	%Area
C-C	284.61	61.97
C-O	285.48	33.99
C=O	288.69	4.03

Name	Pos.	%Area
O-Ti-O	529.73	74.03
C-O-H	531.20	21.00
C=O	533.20	4.97

Name	Pos.	%Area
Ti 2p3/2 Ti(IV)	458.31	56.53
Ti 2p1/2 Ti(IV)	464.03	28.20
Ti 2p3/2 Ti(III)	456.89	5.98
Ti 2p1/2 Ti(III)	462.42	2.98
TiN 2p 3/2	455.00	4.21
TiN 2p 1/2	460.70	2.10

Name	Pos.	%Area
Ti OxyNitride	395.54	13.32
N	399.47	66.58
TiN	396.15	20.10

Figure A7: XPS spectra for N_2-He sample

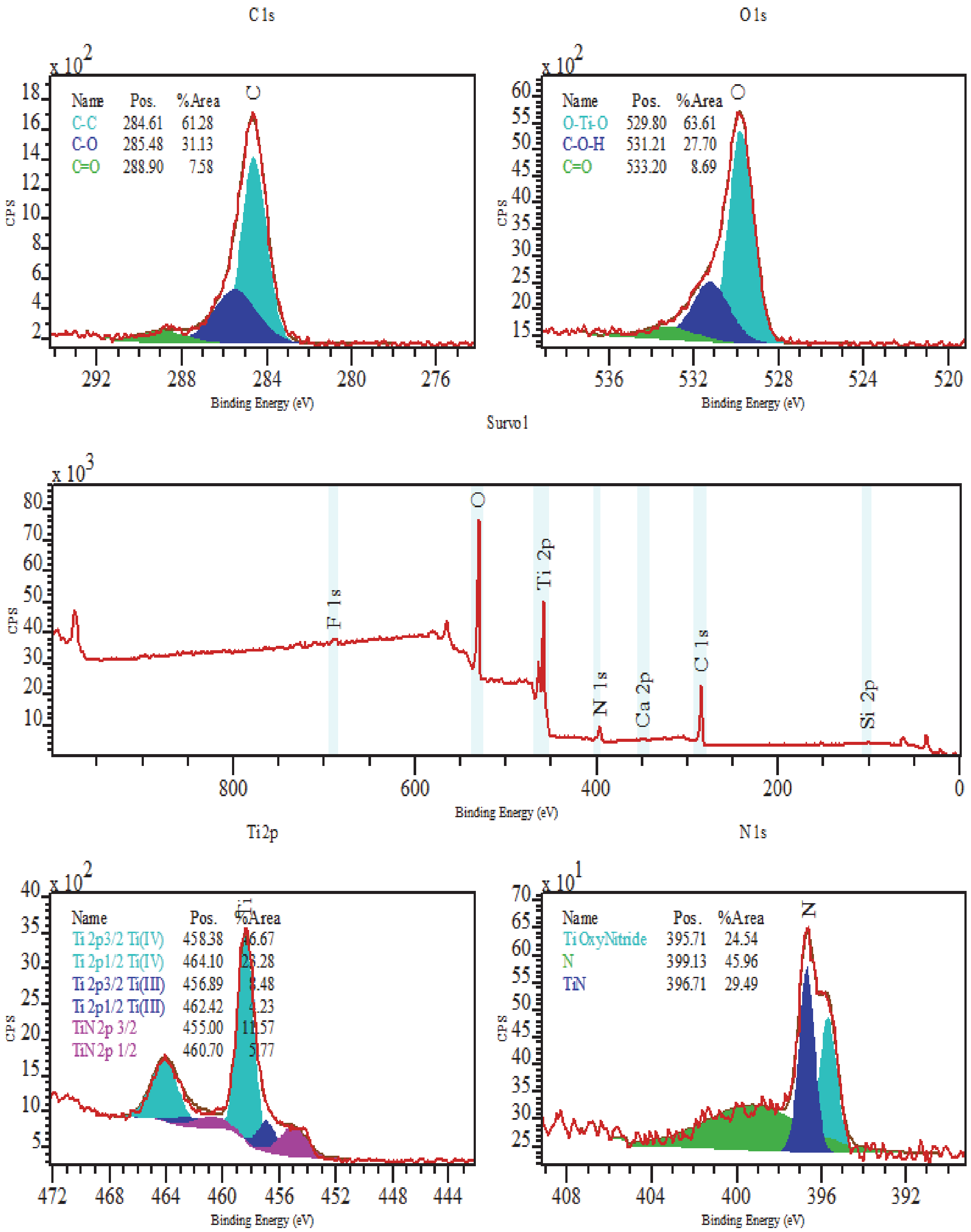

Figure A8: XPS spectra for N_2-N_2 sample

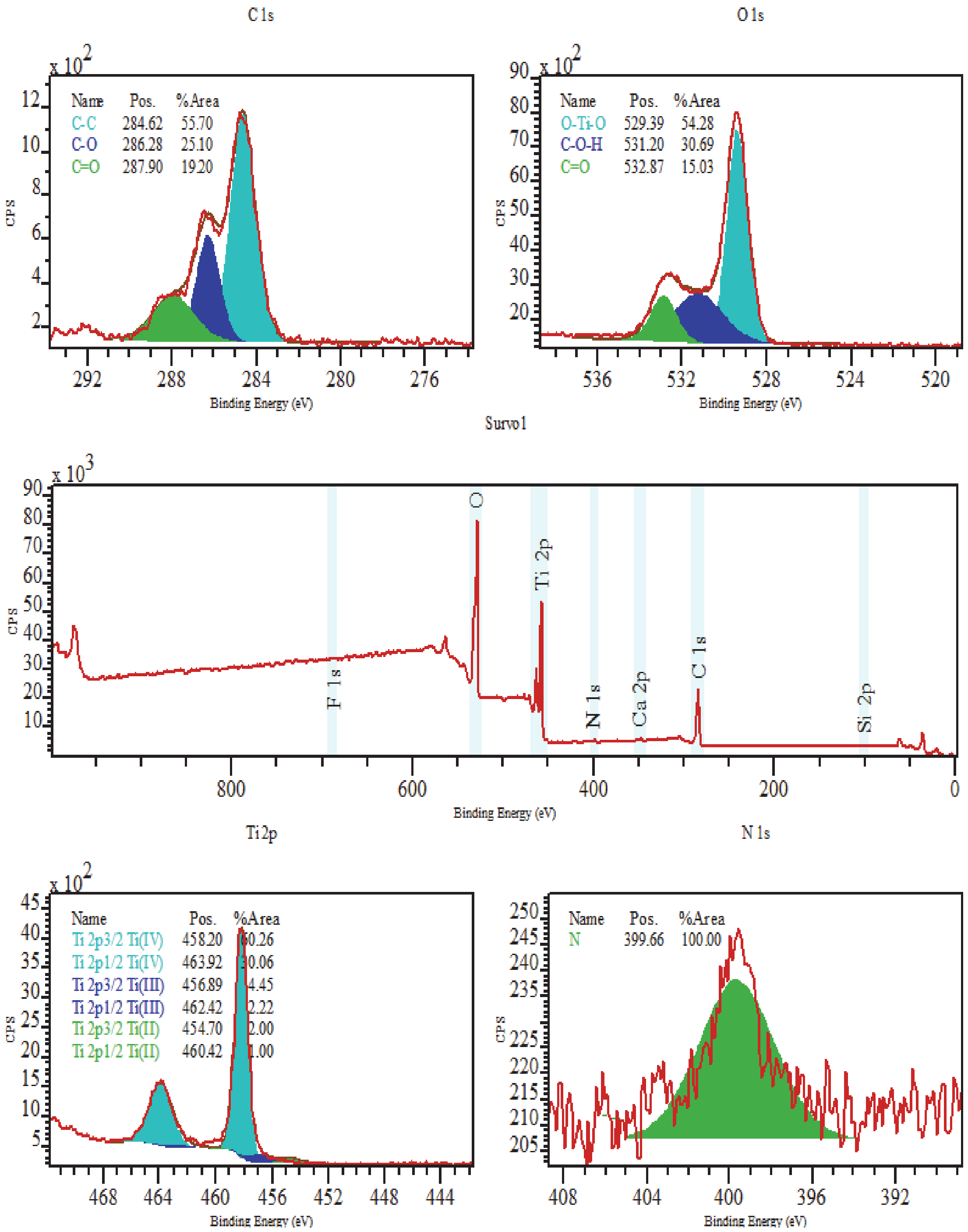

C 1s

Name	Pos.	%Area
C-C	284.62	55.70
C-O	286.28	25.10
C=O	287.90	19.20

O 1s

Name	Pos.	%Area
O-Ti-O	529.39	54.28
C-O-H	531.20	30.69
C=O	532.87	15.03

Ti2p

Name	Pos.	%Area
Ti 2p3/2 Ti(IV)	458.20	60.26
Ti 2p1/2 Ti(IV)	463.92	30.06
Ti 2p3/2 Ti(III)	456.89	4.45
Ti 2p1/2 Ti(III)	462.42	2.22
Ti 2p3/2 Ti(II)	454.70	2.00
Ti 2p1/2 Ti(II)	460.42	1.00

N 1s

Name	Pos.	%Area
N	399.66	100.00

Figure A9: XPS spectra for He-O_2 sample

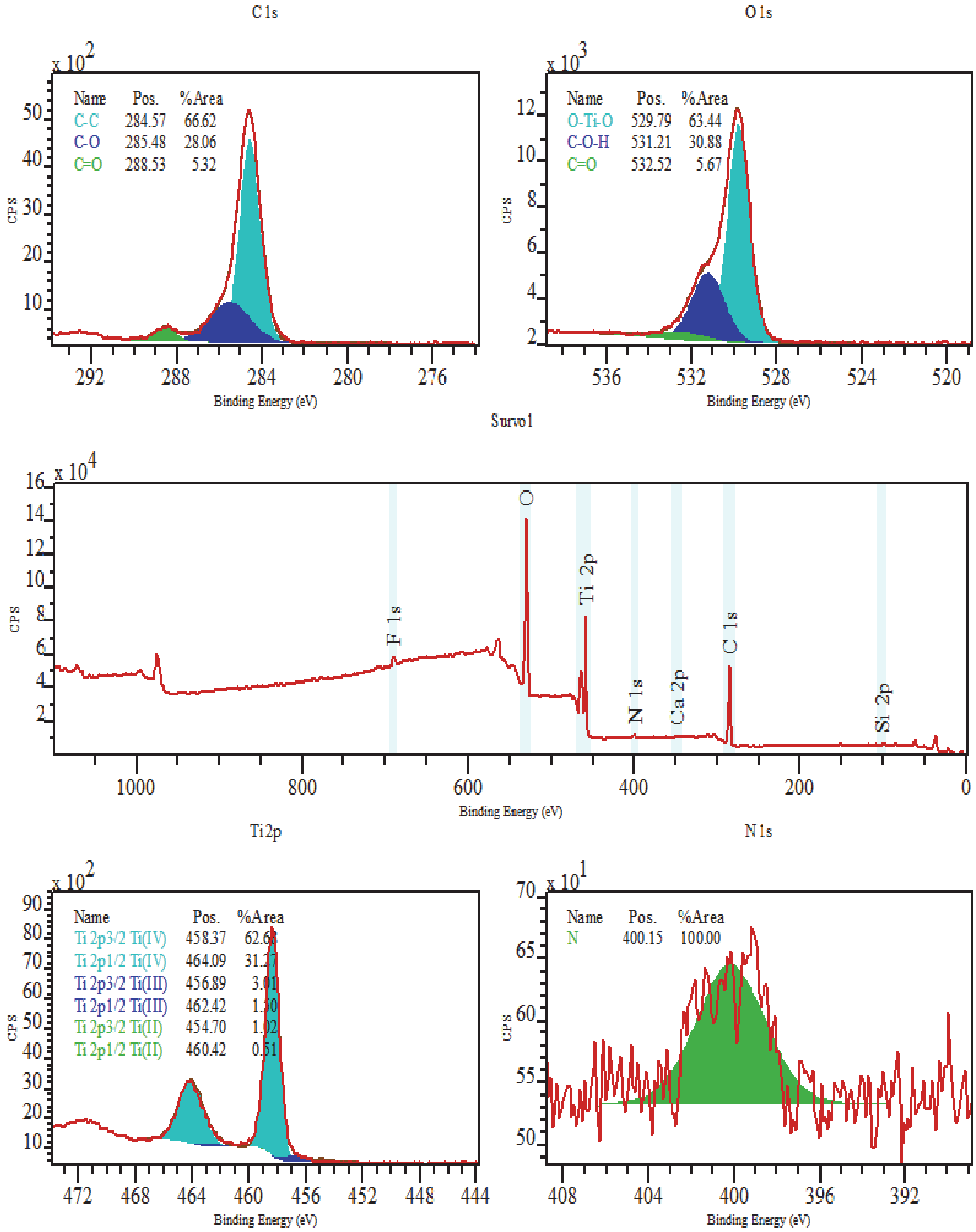

Figure A10: XPS spectra for He-He sample

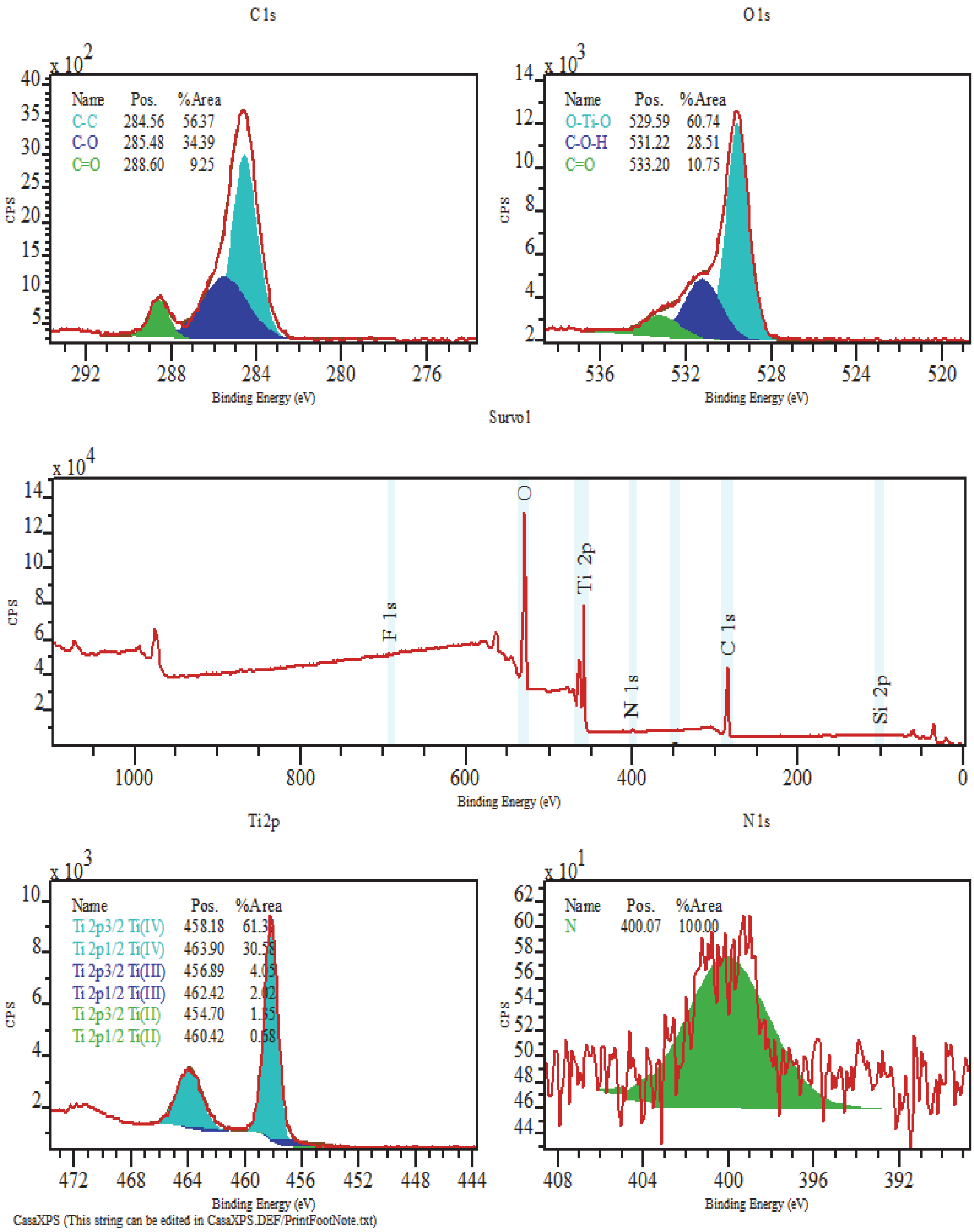

Figure A11: XPS spectra for He-N_2 sample

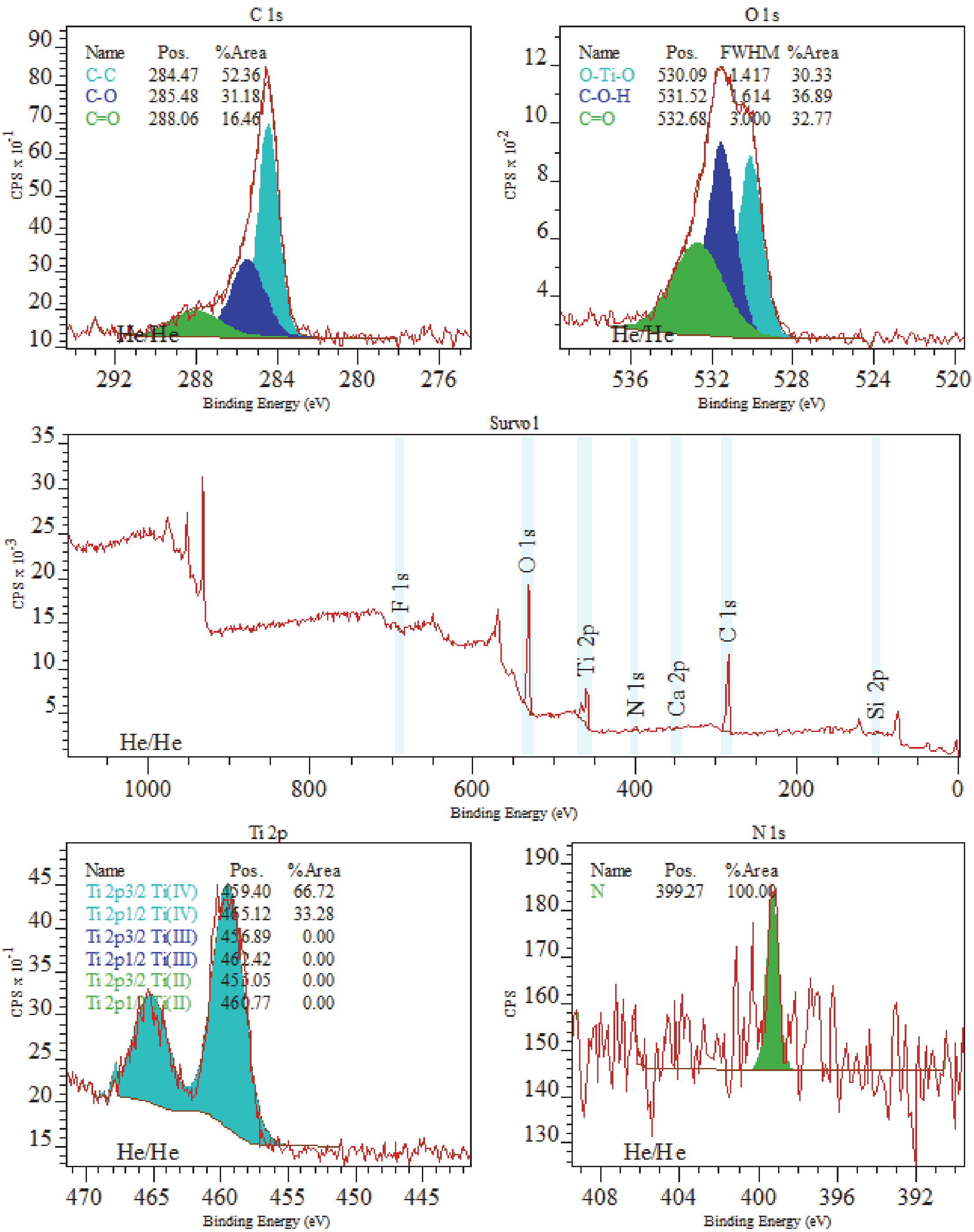

Figure A12: XPS spectra for particles of sample He-He

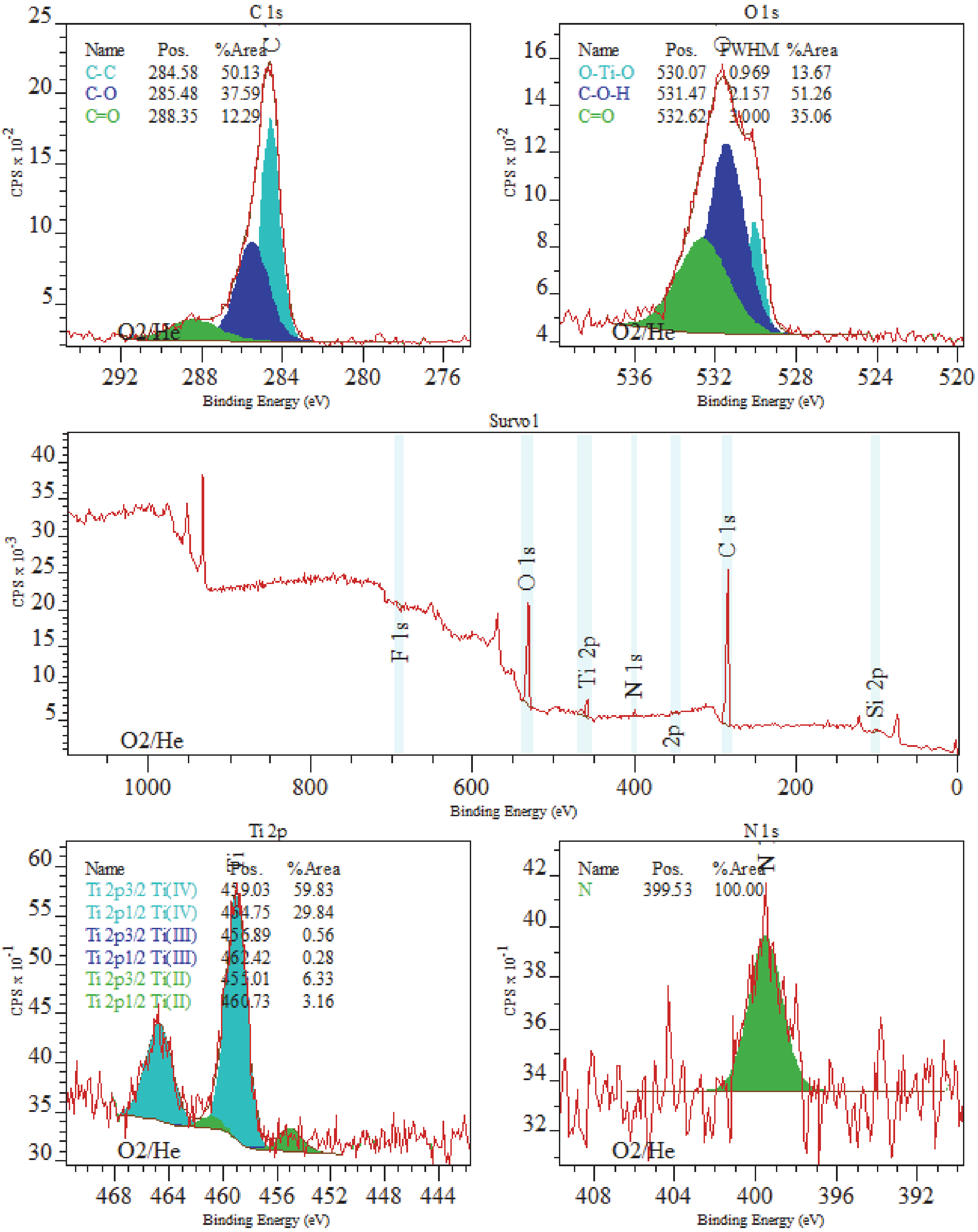

Figure A13: XPS spectra for particles of sample O_2-He

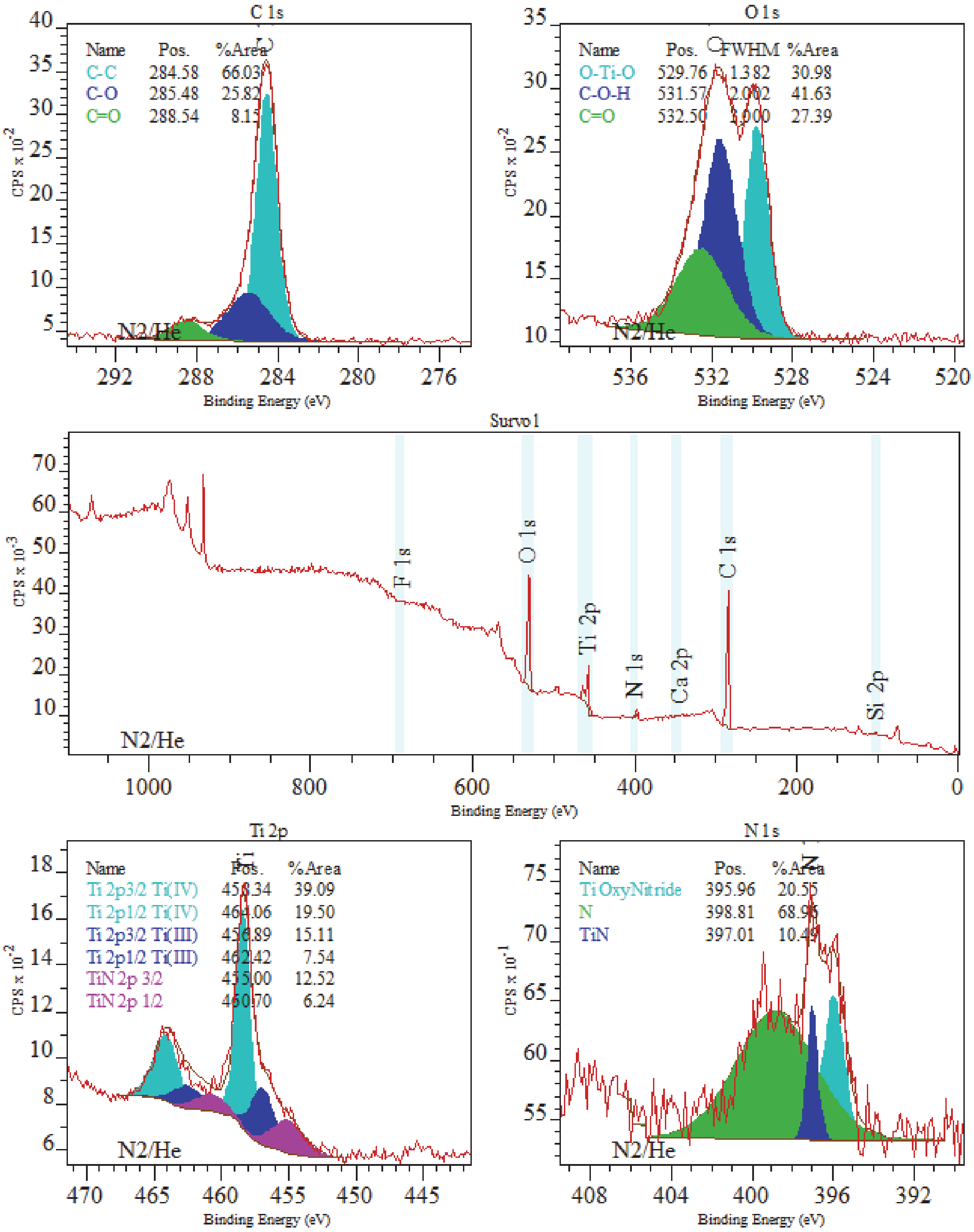

Figure A14: XPS spectra for particles from sample N_2-He

Appendix C: Supporting information for manuscript in Chapter 5

1. Relevant parameters and extreme values

Table A2 lists extreme values for the parameters as they occur in the course of the colloidal AFM measurements in humid air within his study. Note: The value for r_{a_1} was provided by the supplier of the colloidal particles. The values for r_{a_2} (smallest feature radius on target surface) and l (minimal distance between AFM probe and target surface) were assumed by the author of this study.

Table A2: Parameter values for the extreme conditions during force measurements

parameter	γ_{LV} [N/m]	V_M [m^3/mol]	R [N m / mol K]	T [K]	p_v [N/m^2]	$p_s(T)$ [N/m^2]	r_{a_1} [nm]	r_{a_2} [nm]	l [nm]
comment	water	water	gas constant	max. temp.	at 90% RH	water in air	rough. AFM probe	min. surface rough.	min. dist.
value	0.072	1.8×10^{-5}	8.314	303	2.8×10^{-6}	3.2×10^{-6}	10	1	1

2. Calculation of relevant length scale l_{cap}

The formation of capillary bridges is hindered on a rough surface when ra_1 and/or ra_2 are of the same length scale as the Kelvin-length (Eq. (A5)) λ_k and the curvature of the meniscus r_{curv} (Eq. (A6)). Both r_{curv} and λ_k are functions of the liquid's surface tension γ_{LA}, the molar volume V_M, the ideal gas constant R, the temperature T, the vapor pressure p_v and the saturation vapor pressure $p_{s(T)}$ (Butt and Kappl 2009).

$$\lambda_k = \frac{\gamma_{LA} V_M}{RT} \tag{A5}$$

$$r_{curv} = \frac{r_1 r_2}{r_1 + r_2} = \frac{V_M \gamma_{LA}}{RT ln\left(\frac{p_v}{p_s(T)}\right)} \tag{A6}$$

Inserting the thermodynamic parameters T, p and $p_s(T)$ and water's material properties γ_{LA} and V_m in Eq. (A5) and Eq. (A6) results in λ_k at 0.5 nm and r_{curv} on the order of 0.5 to 5 nm (Eq. (A7) – (A9)). Thus, the combined topological length scale that determines the formation of capillary bridges, denoted by l_{cap} in this study, has the range from 0.5 to 5 nm. Note: The negative sign of r_{curv} indicates the concave shape of the meniscus.

$$\lambda_k = \frac{\gamma_{LA} V_M}{RT} = \frac{0.072 \times 1.8 \times 10^{-5}}{8.314 \times 303} m = 0.5\, nm \tag{A7}$$

$$r_{curv} = \frac{r_1 r_2}{r_1 + r_2} = \frac{V_M \gamma_{LA}}{RT ln\left(\frac{p_v}{p_s(T)}\right)} = \frac{0.072 \times 1.8 \times 10^{-5}}{8.314 \times 303 \times (-4.61)} m = (-)0.1\, nm \tag{A8}$$

$$r_{curv} = \frac{r_1 r_2}{r_1 + r_2} = \frac{V_M \gamma_{LA}}{RT ln\left(\frac{p_v}{p_s(T)}\right)} = \frac{0.072 \times 1.8 \times 10^{-5}}{8.314 \times 303 \times (-0.11)} m = (-)4.6\, nm \tag{A9}$$

3. Calculation of capillary force

The geometric interaction scheme between a colloidal AFM probe and an arbitrary surface of interest is described either by a curved-with-flat surface (Eq. (A10)) scenario or a curved-with-curved surface (Eq. (A11)) scenario (Ando 2000, Riedo, Levy et al. 2002, Butt and Kappl 2009, Crassous, Ciccotti et al. 2011). The capillary force F_{cap} arising from a single capillary bridge depends on γ_{LV} and the distance l between the AFM probe and the surface. The radius r_a of the interacting surface features (r_{a_1} = probe, r_{a_2} = sample surface) reflects the topological properties of the surface (roughness), while the meniscus's curvature r_{curv} describes the geometry of the meniscus and the capillary bridge.

The capillary force originating from a single bridge has according to Eq. 1a and Eq. 1b a maximum around 10 nN for two interacting superhydrophilic or superhydrophobic surfaces (c = 1) under the extreme experimental parameters under the extreme experimental parameters: The AFM probe is at the closest distance to the surface (l = 1 nm), the vapor pressure has its maximum at 70% RH and the feature radii are given by the colloidal probe's roughness (r_{a_1} = 20/2 nm) and the sample's nanoscale surface features ($r_{a_2} \sim l_{cap} \sim 5$ nm).

$$F_{cap} = 2\pi\gamma_{LV}\left(2c - \frac{l}{r_{curv}}\right) r_{a_1} \tag{A9}$$

$$F_{cap} = 2\pi\gamma_{LV}\left(2c - \frac{l}{r_{curv}}\right)\left(\frac{r_{a_1} r_{a_2}}{r_{a_1}+r_{a_2}}\right) \tag{A10}$$

The wettability factor c (Eq. A11) depends on the surface chemistry of the two interacting surfaces. θ_{E_1} and θ_{E_2} stand for the nanoscopic contact angles (CA) of the AFM probe and the target surface, respectively. Since θ_{E_1} and θ_{E_2} are practically impossible to determine, the macroscopic CAs is typically used instead. β denotes the filling angle, which is geometrically derived and represents the position of the three phase contact line (Butt and Kappl 2009)). Eq. (A11) has its maximum at $c = 1$ for two interacting surfaces with a contact angle of zero.

$$c = \frac{cos(\theta_{E1} + \beta) + cos(\theta_{E2})}{2} = \frac{1+1}{2} = 1 \tag{A11}$$

Eq. (A9) and Eq. (A10) reach their maximum for the values of the experimental parameters at the extreme experimental conditions listed in Table A2. Eq. (A12) delivers the result for the curved-with-flat interaction regime and Eq. (A13) for the curved-with-curved interaction regime.

$$F_{cap} = 2\pi \times 0.072 \frac{nN}{nm} \times \left(2 - \frac{1\ nm}{1.4\ nm}\right) \times 10\ nm = 0.58\ \frac{nN}{nm} \times 10\ nm = 5.8\ nN \tag{A12}$$

$$F_{cap} = 2\pi \times 0.072 \frac{nN}{nm} \times \left(2 - \frac{1\ nm}{1.4\ nm}\right) \times \left(\frac{10\ nm \times 1\ nm}{10\ nm + 1\ nm}\right) = 0.5\ nN \tag{A13}$$

Consequently, it can be assumed that under no circumstances the capillary force that originates from a single capillary bridge is larger than 10 nN.

.

4. EDX maps for selected samples

Ti **O** **N**

O_2CO_2 ripple

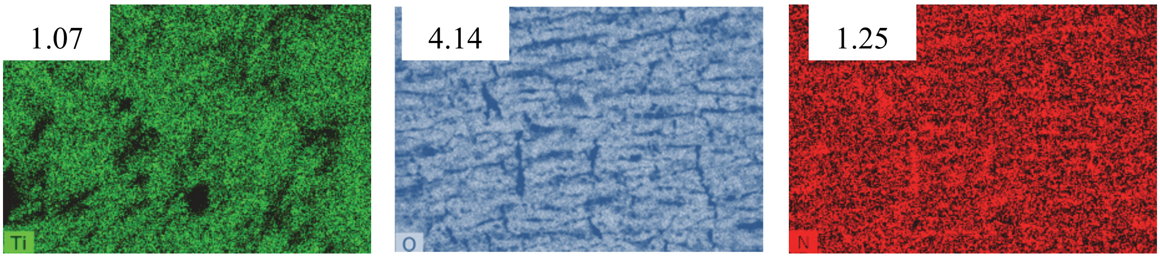

N_2CO_2 ripple

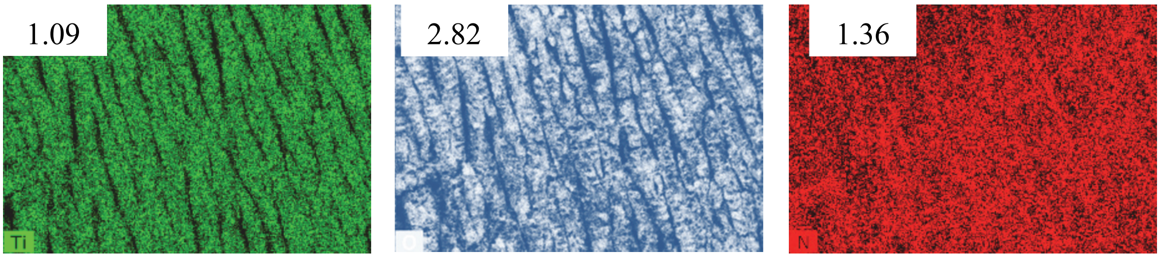

N_2O_2 ripple

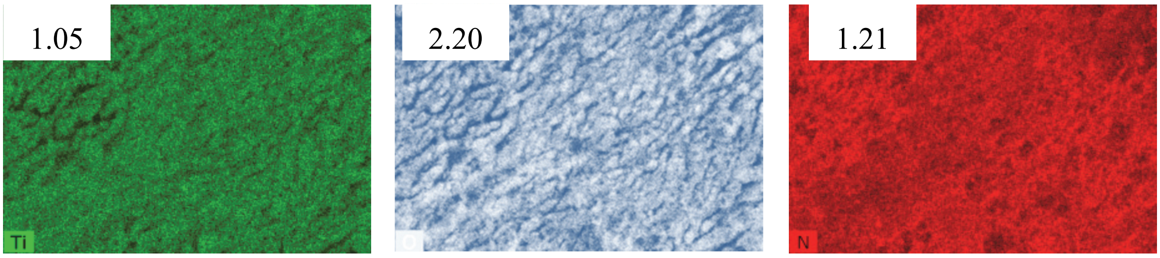

H_2H_2 ripple

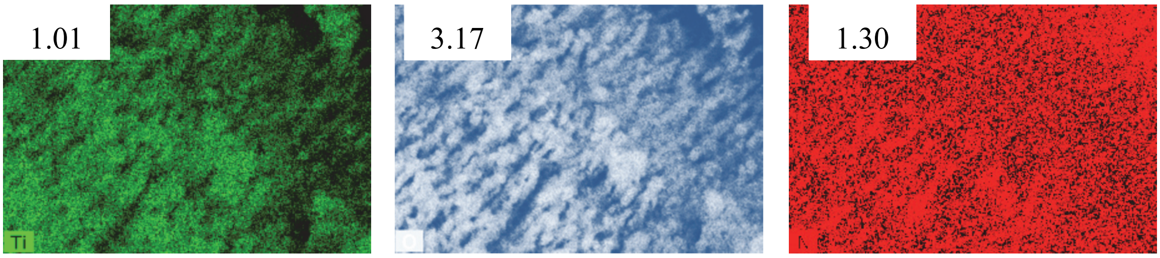

Figure A15: Selected EDX maps on different ripple samples with lacunarity value (resolution 5 nm).

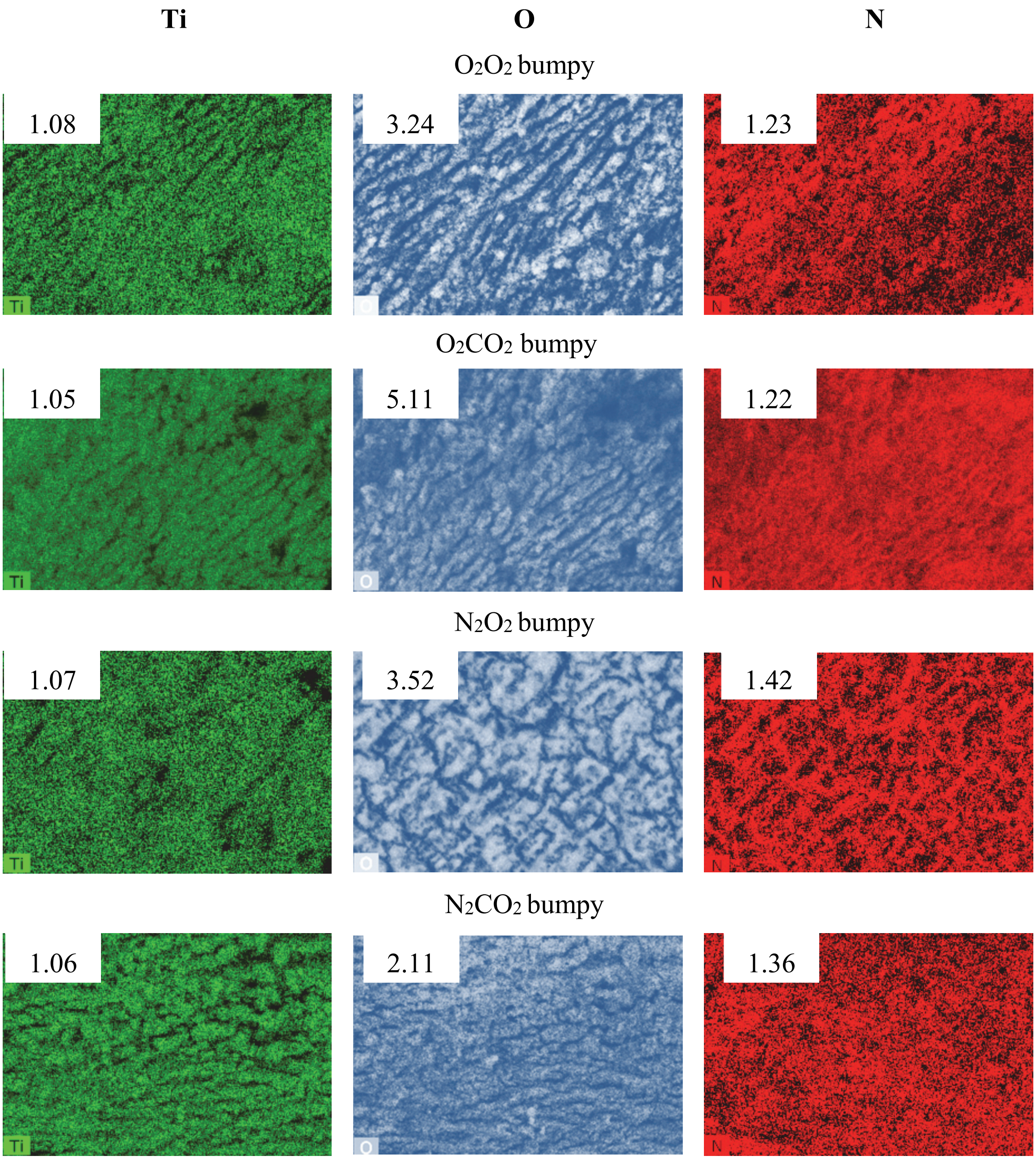

Figure A16: Selected EDX maps on different bumpy samples (resolution 5 nm).

References

Acharya, H., S. Vembanur, S. N. Jamadagni and S. Garde (2010). "Mapping hydrophobicity at the nanoscale: Applications to heterogeneous surfaces and proteins." Faraday Discussions **146**: 353-365.

Adam, N. K. (1930). The physics and chemistry of surfaces. Oxford, Clarendon Press.

Ahmmed, K. M. T., C. Grambow and A.-M. Kietzig (2014). "Fabrication of Micro/Nano Structures on Metals by Femtosecond Laser Micromachining." micromachines **5**(4): 1219-1253.

Ahmmed, K. M. T., E. J. Y. Ling, P. Servio and A.-M. Kietzig (2015). "Introducing a new optimization tool for femtosecond laser-induced surface texturing on titanium, stainless steel, aluminum and copper." Optics and Lasers in Engineering **66**(0): 258-268.

Ahsan, M. S., F. Ahmed, Y. G. Kim, M. S. Lee and M. B. G. Jun (2011). "Colorizing stainless steel surface by femtosecond laser induced micro/nano-structures." Applied Surface Science **257**(17): 7771-7777.

Anderson, T. P., C. Wilson, C. A. Zuhlke, C. Kruse, A. Hassebrook, I. Somanas, S. Ndao, G. Gogos and D. Alexander (2014). "Tailoring liquid/solid interfacial energy transfer: fabrication and application of multiscale metallic surfaces with engineered heat transfer and electrolysis properties via femtosecond laser surface processing techniques." Laser-based Micro- and Nanoprocessing VIII **8968**: 89680-89687.

Ando, Y. (2000). "The effect of relative humidity on friction and pull-off forces measured on submicron-size asperity arrays." Wear **238**(1): 12-19.

Ando, Y. (2004). "Friction and pull-off forces on submicron-size asperities measured in high-vacuum and in both dry and humid nitrogen at atmospheric pressure." Japanese Journal of Applied Physics **43**(78): 4506-4510.

Ando, Y. (2008). "Effect of contact geometry on the pull-off force evaluated under high-vacuum and humid atmospheric conditions." Langmuir **24**(4): 1418-1424.

Andrews, H., E. Eccles, W. Schofield and J. Badyal (2011). "Three-dimensional hierarchical structures for fog harvesting." Langmuir **27**(7): 3798-3802.

Anisimov, S. I., B. L. Kapeliovich and T. L. Perel'man (1974). "Electron emission from metal surfaces exposed to ultrashort laser pulses." Soviet Physics Journal of Experimental and Theoretical Physics **39**(2): 375-377.

Anisimov, S. I., B. L. Kapeliovich and T. L. Perelman (1974). "Emission of electrons from the surface of metals induced by ultrashort laser pulses." Zhurnal Eksperimental'noi i Teoreticheskoi Fiziki **66**(2): 776-781.

Arlt, J. and K. Dholakia (2000). "Generation of high-order Bessel beams by use of an axicon." Optics Communications **177**(1–6): 297-301.

Ashkenasi, D., M. Lorenz, R. Stoian and A. Rosenfeld (1999). "Surface damage threshold and structuring of dielectrics using femtosecond laser pulses: the role of incubation." Applied Surface Science **150**(1-4): 101-106.

Assad, O., A. M. Leshansky, B. Wang, T. Stelzner, S. Christiansen and H. Haick (2012). "Spray-coating route for highly aligned and large-scale arrays of nanowires." ACS Nano **6**(6): 4702-4712.

Ata, A., Y. I. Rabinovich and R. K. Singh (2002). "Role of surface roughness in capillary adhesion." Journal of Adhesion Science and Technology **16**(4): 337-346.

Banerjee, S., P. Mulder, J. M. Kleijn and M. A. Cohen Stuart (2012). "Effect of surface roughness and softness on water capillary adhesion in apolar media." Journal of Physical Chemistry A **116**(25): 6481-6488.

Baojia, L., Z. Ming, Y. Run and C. Lan (2008). "Fabrication of titanium-based microstructured surfaces and study on their superhydrophobic stability." Journal of Materials Research **23**(9): 2491-2499.

Barthélemy, O., J. Margot, M. Chaker, M. Sabsabi, F. Vidal, T. W. Johnston, S. Laville and B. Le Drogoff (2005). "Influence of the laser parameters on the space and time characteristics of an aluminum laser-induced plasma." Spectrochimica Acta Part B: Atomic Spectroscopy **60**(7–8): 905-914.

Barthelemy, O., J. Margot, S. La Ville, F. Vidal, M. Chaker, B. Le Drogoff, T. W. Johnston and M. Sabsabi (2005). "Investigation of the state of local thermodynamic equilibrium of a laser-produced aluminum plasma." Applied Spectroscopy **59**(4): 529-536.

Batani, D. (2010). "Short-pulse laser ablation of materials at high intensities: Influence of plasma effects." Laser and Particle Beams: pulse power & high energy densities **28**(2): 235-244.

Batani, D., R. Jafer, M. Veltcheva, R. Dezulian, O. Lundh, F. Lindau, A. Persson, K. Osvay, C. G. Wahlström, D. C. Carroll, P. McKenna, A. Flacco and V. Malka (2010). "Effects of laser prepulses on laser-induced proton generation." New Journal of Physics **12**(4): 045018.

Beach, E. and J. Drelich (2011). "Atomic Force Microscope Pull-off Force Measurements for Insulin in Contact with AcrylonitrileButadieneStyrene and Polypropylene Surfaces at Various Humidities." Journal of Adhesion Science and Technology, 25 **4**(5): 435-449.

Bhushan, B. (2009). "Biomimetics: lessons from nature–an overview." **367**(1893): 1445-1486.

Bhushan, B. and Y. C. Jung (2010). "Natural and biomimetic artificial surfaces for superhydrophobicity, self-cleaning, low adhesion, and drag reduction." Progress in Materials Science **56**(1): 1-108.

Bhushan, B., Y. Wang and A. Maali (2009). "Boundary slip study on hydrophilic, hydrophobic, and superhydrophobic surfaces with dynamic atomic force microscopy." Langmuir **25**(14): 8117-8121.

Bizi-Bandoki, P., S. Benayoun, S. Valette, B. Beaugiraud and E. Audouard (2011). "Modifications of roughness and wettability properties of metals induced by femtosecond laser treatment." Applied Surface Science **257**(12): 5213-5218.

Bizi-Bandoki, P., S. Valette, E. Audouard and S. Benayoun (2013). "Effect of stationary femtosecond laser irradiation on substructures' formation on a mold stainless steel surface." Applied Surface Science **270**: 197-204.

Bizi-bandoki, P., S. Valette, E. Audouard and S. Benayoun (2013). "Time dependency of the hydrophilicity and hydrophobicity of metallic alloys subjected to femtosecond laser irradiations." Applied Surface Science **273**(0): 399-407.

Bonse, J., S. Baudach, J. Kruger, W. Kautek and M. Lenzner (2002). "Femtosecond laser ablation of silicon-modification thresholds and morphology." Applied Physics A (Materials Science Processing) **74**(1): 19-25.

Booth, H. J. (2004). "Recent applications of pulsed lasers in advanced materials processing." Thin Solid Films **453–454**(0): 450-457.

Bormashenko, E. (2009). "Wetting of Flat and Rough Curved Surfaces." The Journal of Physical Chemistry C **113**(40): 17275-17277.

Bormashenko, E. (2010). "Wetting transitions on biomimetic surfaces." Philosophical Transactions of the Royal Society A: Mathematical, Physical and Engineering Sciences **368**(1929): 4695-4711.

Bormashenko, E. (2011). "General equation describing wetting of rough surfaces." Journal of Colloid and Interface Science **360**(1): 317-319.

Borowiec, A. and H. K. Haugen (2003). "Subwavelength ripple formation on the surfaces of compound semiconductors irradiated with femtosecond laser pulses." Applied Physics Letters **82**(25): 4462-4464.

Breitling, D., A. Ruf and F. Dausinger (2004). Fundamental aspects in machining of metals with short and ultrashort laser pulses. Photon Processing in Microelectronics and Photonics III, San Jose, International Society for Optics and Photonics.

Burghardt, B., S. Scheede, R. Senczuk and H. J. Kahlert (1999). "Ablation plume effects on high precision excimer laser-based micromachining." Applied Physics A (Materials Science Processing) **A69**(69): 137-140.

Butt, H.-J., M. Farshchi-Tabrizi and M. Kappl (2006). "Using capillary forces to determine the geometry of nanocontacts." Journal of Applied Physics **100**(2): 24312-24317.

Butt, H.-J. and M. Kappl (2010). Capillary Forces. Surface and Interfacial Forces. Weinheim, Wiley-VCH Verlag GmbH & Co. KGaA**:** 127-161.

Butt, H.-J. and M. Kappl (2010). Contact Mechanics and Adhesion. Surface and Interfacial Forces. Weinheim, Wiley-VCH Verlag GmbH & Co. KGaA**:** 219-250.

Butt, H.-J. and M. Kappl (2010). Surface and interfacial forces. Weinheim, Wiley-VCH.

Butt, H. J. (1991). "Electrostatic interaction in atomic force microscopy." Biophysical Journal **60**(4): 777-785.

Butt, H. J. (1991). "Measuring electrostatic, van der Waals, and hydration forces in electrolyte solutions with an atomic force microscope." Biophysical Journal **60**(6): 1438-1444.

Butt, H. J., B. Cappella and M. Kappl (2005). "Force measurements with the atomic force microscope: Technique, interpretation and applications." Surface Science Reports **59**(1-6): 1-152.

Butt, H. J. and M. Kappl (2009). "Normal capillary forces." Advances in colloid and interface science **146**(1-2): 48-60.

Cassie, A. B. D. (1948). "Contact angles." Discussions of the Faraday Society **3**: 11-16.

Cassie, A. B. D. and S. Baxter (1944). "Wettability of porous surfaces." Transactions of the Faraday Society **40**: 546-551.

Chang, J. J., B. E. Warner, E. P. Dragon and M. W. Martinez (1998). "Precision micromachining with pulsed green lasers." Journal of Laser Applications **10**(6): 285-291.

Charlaix, E. and J. Crassous (2005). "Adhesion forces between wetted solid surfaces." The Journal of Chemical Physics **122**: 184701.

Chen, Z., X. Fu, N. Geng and X. Hu (2009). "Effects of parameters in femtosecond laser micromachining on ablation of silicon." Transactions of Tianjin University **15**(3): 225-228.

Chen, Z. and S. S. Mao (2008). "Femtosecond laser-induced electronic plasma at metal surface." Applied Physics Letters **93**(5): 051506.

Cheng, C. and X. Xu (2005). "Mechanisms of decomposition of metal during femtosecond laser ablation." Physical review B **72**(16): 165415.

Cheng, J., W. Perrie, S. P. Edwardson, E. Fearon, G. Dearden and K. G. Watkins (2009). "Effects of laser operating parameters on metals micromachining with ultrafast lasers." Applied Surface Science **256**(5): 1514-1520.

Chengwu, Y., X. Binshi, H. Jian, Z. Peilei and W. Yixiong (2010). "Study on the softening in overlapping zone by laser-overlapping scanning surface hardening for carbon and alloyed steel." Optics and Lasers in Engineering **48**(1): 20-26.

Chien, C. Y. and M. C. Gupta (2005). "Pulse width effect in ultrafast laser processing of materials." Applied Physics A: Materials Science and Processing **81**(6): 1257-1263.

Chiron, A., B. Lamouroux, R. Lange, J. F. Ripoche, M. Franco, B. Prade, G. Bonnaud, G. Riazuelo and A. Mysyrowicz (1999). "Numerical simulations of the nonlinear propagation of femtosecond optical pulses in gases." The European Physical Journal D - Atomic, Molecular, Optical and Plasma Physics **6**(3): 383-396.

Corkum, P. B., F. Brunel, N. K. Sherman and T. Srinivasan-Rao (1988). "Thermal Response of Metals to Ultrashort-Pulse Laser Excitation." Physical Review Letters **61**(25): 2886-2889.

Craig, B. (1998). "Ultrafast pulses promise better processing of fine structures." Laser Focus World **34**(9): 79-84.

Crassous, J., M. Ciccotti and E. Charlaix (2011). "Capillary force between wetted nanometric contacts and its application to atomic force microscopy." Langmuir **27**(7): 3468-3473.

Czarnowska, E., T. Wierzchoń and A. Maranda-Niedbała (1999). "Properties of the surface layers on titanium alloy and their biocompatibility in in vitro tests." Journal of Materials Processing Technology **92–93**(0): 190-194.

Daniello, R. J., N. E. Waterhouse and J. P. Rothstein (2009). "Drag reduction in turbulent flows over superhydrophobic surfaces." Physics of Fluids **21**: 085103.

de Gennes, P.-G. d., F. Brochard-Wyard and D. Quere (2003). Capillarity and Wetting Phenomena: Drops, Bubbles, Pearls, Waves. New York, Springer.

de Gennes, P. (1985). "Wetting: statics and dynamics." Reviews of Modern Physics **57**(3): 827-863.

Delaigue, M., C. Honninger, R. Torres, A. Lidolff, C. Loumena, J. Lopez, R. Kling and E. Mottay (2012). Comparative ultrafast laser source study for advanced materials processing. 2012 Conference on Lasers and Electro-Optics, CLEO 2012, May 6, 2012 - May 11, 2012, San Jose, CA, United states, IEEE Computer Society.

Demir, A. G. (2013). Development of Processing and Monitoring Strategies for

Laser Surface Texturing of TiN coatings. PhD, POLITECNICO DI MILANO.

Demir, A. G., V. Furlan, N. Lecis and B. Previtali (2014). "Laser surface structuring of AZ31 Mg alloy for controlled wettability." Biointerphases **9**(2): 029009.

Demir, A. G., B. Previtali and C. A. Biffi (2013). "Fibre Laser Cutting and Chemical Etching of AZ31 for Manufacturing Biodegradable Stents." Advances in Materials Science and Engineering **2013**: 11.

Derjaguin, B. V. (1934). "Molecular theory of friction and sliding." KolloidZ.(69): 155-156.

Drechsler, M. (1983). ON THE DIFFERENT DRIVING FORCES FOR THE MATTER TRANSPORT ALONG SURFACES. Surface Mobilities on Solid Materials: Fundamental Concepts and Applications (Proceedings of a NATO Advanced Study Institute). New York, NY, USA, Plenum Press.

Drouet, M. G. and J. L. Meunier (1985). "Influence of the Background Gas Pressure on the Expansion of the Arc-Cathode Plasma." Plasma Science, IEEE Transactions on **13**(5): 285-287.

Du, D., X. Liu, G. Korn, J. Squier and G. Mourou (1994). Optical breakdown with femtosecond laser pulses. Proceedings of the Conference on Lasers and Electro-Optics, May 8, 1994 - May 13, 1994, Anaheim, CA, USA, Publ by IEEE.

Ducker, W. A., T. J. Senden and R. M. Pashley (1991). "Direct measurement of colloidal forces using an atomic force microscope." Nature **353**(6341): 239-241.

Dupre, A. (1869). Theorie Mécanique la Chaleur. Paris, Gauthier-Villars.

Eichstädt, J., G. R. B. E. Römer and A. J. Huis in ‘t Veld (2013). "Determination of irradiation parameters for laser-induced periodic surface structures." Applied Surface Science **264**(0): 79-87.

Extrand, C. W. (2003). "Contact angles and hysteresis on surfaces with chemically heterogeneous islands." Langmuir **19**(9): 3793-3796.

Extrand, C. W. (2005). "Erratum: Contact angles and hysteresis on surfaces with chemically heterogeneous islands (Langmuir (2003) 19 (3793-3796))." Langmuir **21**(24): 11546-11546.

Feiler, A. A., P. Jenkins and M. W. Rutland (2005). "Effect of relative humidity on adhesion and frictional properties of micro- And nano-scopic contacts." Journal of Adhesion Science and Technology **19**(3-5): 165-179.

Feiler, A. A., J. Stiernstedt, K. Theander, P. Jenkins and M. W. Rutland (2007). "Effect of capillary condensation on friction force and adhesion." Langmuir **23**(2): 517-522.

Fisher, L. R. and J. N. Israelachvili (1981). "Direct measurement of the effect of meniscus forces on adhesion: a study of the applicability of macroscopic thermodynamics to microscopic liquid interfaces." Colloids and Surfaces **3**(4): 303-319.

Frisbie, C. D., L. F. Rozsnyai, A. Noy, M. S. Wrighton and C. M. Lieber (1994). "Functional group imaging by chemical force microscopy." Science **265**(5181): 2071-2074.

Gamaly, E. G. (2011). Femtosecond Laser - Matter Interactions: Theory, Experiments and Applications. Singapore, Pan Stanford Publishing Pte. Ltd.

Gamaly, E. G., N. R. Madsen, M. Duering, A. V. Rode, V. Z. Kolev and B. Luther-Davies (2005). "Ablation of metals with picosecond laser pulses: Evidence of long-lived nonequilibrium conditions at the surface." Physical Review B **71**(17): 174405.

Gamaly, E. G., A. V. Rode, V. T. Tikhonchuk and B. Luther-Davies (2001). "Ablation of solids by femtosecond lasers:

ablation mechanism and ablation thresholds for metals and dielectrics." Phys. Rev. A.

Gang, C. and T. Yiliu (2012). "The threshold intensity measurement in the femtosecond laser ablation by defocusing." Optics and Lasers in Engineering **50**(5): 767-771.

Garnier, F., R. Hajlaoui, A. Yassar and P. Srivastava (1994). "All-Polymer Field-Effect Transistor Realized by Printing Techniques." Science **265**(5179): 1684-1686.

Gattass, R. R., L. R. Cerami and E. Mazur (2006). "Micromachining of bulk glass with bursts of femtosecond laser pulses at variable repetition rates." Optics Express **14**(12): 5279-5284.

Geng, N., X. Fu, H. X. Li, X. C. Ni and X. T. Hu (2007). "Effect of laser parameters in the micromachining of silicon by femtosecond pulse laser." Key Engineering Materials **339**: 136-140.

Glover, T. E. (2003). "Hydrodynamics of particle formation following femtosecond laser ablation." Journal of the Optical Society of America B **20**(1): 125-131.

Gnecco, E., E. Riedo, R. Bennewitz, E. Meyer and H. Brune (2003). Thermally activated phenomena observed by atomic force microscopy. Dynamics in Small Confining Systems - 2003, December 1, 2003 - December 4, 2003, Boston, MA, United states, Materials Research Society.

Gökhan Demir, A., V. Furlan, N. Lecis and B. Previtali (2014). "Laser surface structuring of AZ31 Mg alloy for controlled wettability." Biointerphases **9**(2): 29009-29020.

Gomez, D., I. Goenaga, I. Lizuain and M. Ozaita (2005). "Femtosecond laser ablation for microfluidics." Optical Engineering **44**(5): 51105-51101.

González-Cardel, M., P. Arguijo and R. Díaz-Uribe (2013). "Gaussian beam radius measurement with a knife-edge: a polynomial approximation to the inverse error function." Appl. Opt. **52**(16): 3849-3855.

Good, R. J. (1976). "On the Definition of Adhesion." The Journal of Adhesion **8**(1): 1-9.

Gould, S., B. Drake, C. Prater, A. Weisenhorn, S. Manne, G. Kelderman, H. J. Butt, H. Hansma, P. Hansma and S. Magonov (1990). "The atomic force microscope: a tool for science and industry." Ultramicroscopy **33**(2): 93-98.

Green, J.-B. D., M. T. McDermott, M. D. Porter and L. M. Siperko (1995). "Nanometer-Scale Mapping of Chemically Distinct Domains at Well-Defined Organic Interfaces Using Frictional Force Microscopy." The Journal of Physical Chemistry **99**(27): 10960-10965.

Groenendijk, M. and J. Meijer (2006). "Microstructuring using femtosecond pulsed laser ablation." Journal of Laser Applications **18**(3): 227-235.

Groenendijk, M. and J. Meijer (2006). "Surface microstructures obtained by femtosecond laser pulses." CIRP Annals - Manufacturing Technology **55**(1): 183-186.

Grojo, D., J. Hermann and A. Perrone (2005). "Plasma analyses during femtosecond laser ablation of Ti, Zr, and Hf." Journal of Applied Physics **97**(6): 063306-063309.

Gu, X., L. Chen, C. Xu, D. Julthongpiput, M. Fasolka and T. Nguyen (2008). Effect of relative humidity on chemical heterogeneity imaging with atomic force microscopy. Nanoscale Phenomena in Functional Materials by Scanning Probe Microscopy, November 26, 2007 - November 30, 2007, Boston, MA, United states, Materials Research Society.

Gu, Z.-Z., H. Uetsuka, K. Takahashi, R. Nakajima, H. Onishi, A. Fujishima and O. Sato (2003). "Structural Color and the Lotus Effect." Angewandte Chemie International Edition **42**(8): 894-897.

Güdde, J., J. Hohlfeld, J. G. Müller and E. Matthias (1998). "Damage threshold dependence on electron–phonon coupling in Au and Ni films." Applied Surface Science **127–129**(0): 40-45.

Guo, C., M. Li, J. P. Nibarger and G. N. Gibson (1998). "Single and double ionization of diatomic molecules in strong laser fields." Physical Review A **58**(6): R4271-R4274.

Guoqiang, L., L. Jiawen, Y. Liang, L. Xiaohong, H. Yanlei, C. Jiaru and H. Wenhao (2013). "Evolution of aluminum surface irradiated by femtosecond laser pulses with different pulse overlaps." Applied Surface Science **276**: 203-209.

Guosheng, Z., P. M. Fauchet and A. E. Siegman (1982). "Growth of spontaneous periodic surface structures on solids during laser illumination." Physical Review B **26**(10): 5366-5381.

Hancock, M. J., K. Sekeroglu and M. C. Demirel (2012). "Bioinspired Directional Surfaces for Adhesion, Wetting, and Transport." Advanced Functional Materials: n/a-n/a.

Hayden, C. J. (2010). "A simple three-dimensional computer simulation tool for predicting femtosecond laser micromachined structures." Journal of Micromechanics and Microengineering **20**(2): 025010 (025011 pp.).

Hecht, U., C. M. Schilz and M. Stratmann (1998). "Influence of relative humidity during film formation processes on the structure of ultrathin polymeric films." Langmuir **14**(23): 6743-6748.

Hencˇ-Bartolic´, Z. A., D. Gracin, H.J. Kunze, and M. Stubicˇar (1995). "Nitrogen laser beam interaction with titanium surface." Fizika **A 4(2)**: 449-456.

Henley, S. J., J. D. Carey, S. R. P. Silva, G. M. Fuge, M. N. R. Ashfold and D. Anglos (2005). "Dynamics of confined plumes during short and ultrashort pulsed laser ablation of graphite." Physical Review B **72**(20): 205413.

Hermann, J., C. Boulmer-Leborgne, B. Dubreuil and I. N. Mihailescu (1993). "Influence of irradiation conditions on plasma evolution in laser-surface interaction." Journal of Applied Physics **74**(5): 3071-3079.

Heuberger, M., C. Drummond and J. Israelachvili (1998). "Coupling of normal and transverse motions during frictional sliding." The Journal of Physical Chemistry B **102**(26): 5038-5041.

Heyde, M., M. Kulawik, H. P. Rust and H. J. Freund (2006). "Frequency-modulated atomic force spectroscopy on NiAl(110) partially covered with a thin alumina film." Physical Review B **73**(12): 125320.

Hoh, J. H., J. P. Cleveland, C. B. Prater, J. P. Revel and P. K. Hansma (1992). "Quantized adhesion detected with the atomic force microscope." Journal of the American Chemical Society **114**(12): 4917-4918.

Huot, N., N. Sanner, E. Audouard, C. Larat and J. P. Huignard (2007). "Direct ultrafast laser micro-structuring of materials using programmable beam shaping." Optics and Lasers in Engineering **45**(6): 737-741.

Hwang, D. J., C. P. Grigoropoulos and T. Y. Choi (2006). "Efficiency of silicon micromachining by femtosecond laser pulses in ambient air." Journal of Applied Physics **99**(8): 83101-83101.

ISO (2005). ISO 11146-2:2005. ISO/TC 172/SC 9 - Electro-optical systems, ISO - Internation Organization for Standardization.

Israelachvili, J. (2010). Intermolecular and Surface Forces. San Diego, Academic Press.

Israelachvili, J. N. (1972). "The Calculation of Van Der Waals Dispersion Forces between Macroscopic Bodies." Proceedings of the Royal Society of London. A. Mathematical and Physical Sciences **331**(1584): 39-55.

Ivanov, D. S. and L. V. Zhigilei (2003). "Combined atomistic-continuum modeling of short-pulse laser melting and disintegration of metal films." Physical Review B **68**(6): 064114.

Jagdheesh, R., B. Pathiraj, E. Karatay, G. R. B. E. Römer and A. J. Huis in‘t Veld (2011). "Laser-Induced Nanoscale Superhydrophobic Structures on Metal Surfaces." Langmuir **27**(13): 8464-8469.

Jang, J., G. C. Schatz and M. A. Ratner (2004). "Capillary force in atomic force microscopy." The Journal of Chemical Physics **120**(3): 1157-1160.

Jarn, M., F. J. Brieler, M. Kuemmel, D. Grosso and M. Linden (2008). "Wetting of heterogeneous nanopatterned inorganic surfaces." Chemistry of Materials **20**(4): 1476-1483.

Jee, Y., M. F. Becker and R. M. Walser (1988). "Laser-induced damage on single-crystal metal surfaces." J. Opt. Soc. Am. B **5**(3): 648-659.

Jinesh, K. B. and J. W. M. Frenken (2006). "Capillary Condensation in Atomic Scale Friction: How Water Acts like a Glue." Physical Review Letters **96**(16): 166103.

Jiwhan, N., L. Jae-Hoon, L. Sang-Yup and N. Suckjoo (2010). "Fabrication of Random Microspikes on Mold Metal by Ultrashort Laser Ablation for Hydrophilic Surface." Japanese Journal of Applied Physics **49**(10): 106503 (106507 pp.).

Jiwhan, N., L. Jae-Hoon, N. Suckjoo, L. Hyuneui and J. Dae-Hwan (2010). "Fabrication of hierarchically micro- and nano-structured mold surfaces using laser ablation for mass production of superhydrophobic surfaces." Japanese Journal of Applied Physics **49**(10): 106502-106508.

Jiwhan, N., S. Jeong and N. Suckjoo (2010). "Fabrication of Microgrooves on Roll Surfaces Using a Scanner and a Telecentric Lens." Japanese Journal of Applied Physics **49**(5): 05EC01 (06 pp.).

Johnson Jr., R. E. and R. H. Dettre (1964). "Contact angle hysteresis. III. Study of an idealized heterogeneous surface." The Journal of Physical Chemistry **68**(7): 1744-1750.

Ju, S. and J. P. Longtin (2004). "Effects of a gas medium on ultrafast laser beam delivery and materials processing." Journal of the Optical Society of America B (Optical Physics) **21**(5): 1081-1088.

Jung, Y. C. and B. Bhushan (2008). "Technique to measure contact angle of micro/nanodroplets using atomic force microscopy." Journal of Vacuum Science & Technology A **26**(4): 777-782.

Kam, D. H., S. Bhattacharya and J. Mazumder (2012). "Control of the wetting properties of an AISI 316L stainless steel surface by femtosecond laser-induced surface modification." Journal of Micromechanics and Microengineering **22**(10): 105019.

Kara, V. and H. Kizil (2012). "Titanium micromachining by femtosecond laser." Optics and Lasers in Engineering **50**(2): 140-147.

Kargl, R., T. Mohan, S. Kostler, S. Spirk, A. Doliska, K. Stana-Kleinschek and V. Ribitsch (2013). "Functional Patterning of Biopolymer Thin Films Using Enzymes and Lithographic Methods." Advanced Functional Materials **23**(3): 308-315.

Kelly, R. and A. Miotello (1996). "Comments on explosive mechanisms of laser sputtering." Applied Surface Science **96**: 205-215.

Kenar, H., E. Akman, E. Kacar, A. Demir, H. Park, H. Abdul-Khaliq, C. Aktas and E. Karaoz (2013). "Femtosecond laser treatment of 316L improves its surface nanoroughness and carbon content and promotes osseointegration: An in vitro evaluation." Colloids and Surfaces B: Biointerfaces **108**(0): 305-312.

Kietzig, A.-M. (2011). "Comments on “An Essay on Contact Angle Measurements” – An Illustration of the Respective Influence of Droplet Deposition and Measurement Parameters." Plasma Processes and Polymers **8**(11): 1003-1009.

Kietzig, A.-M., S. G. Hatzikiriakos and P. Englezos (2009). "Ice friction: The effects of surface roughness, structure, and hydrophobicity." Journal of Applied Physics **106**(2).

Kietzig, A.-M., S. G. Hatzikiriakos and P. Englezos (2009). "Patterned superhydrophobic metallic surfaces." Langmuir **25**(8): 4821-4827.

Kietzig, A.-M., J. Lehr, L. Matus and F. Liang (2014). "Laser-induced patterns on metals and polymers for biomimetic surface engineering." Laser Applications in Microelectronic and Optoelectronic Manufacturing (LAMOM) XIX **8967**: 896705-896713.

Kietzig, A.-M., M. N. Mirvakili, S. Kamal, P. Englezos and S. G. Hatzikiriakos (2012). "Laser-patterned super-hydrophobic pure metallic substrates: Cassie to Wenzel wetting transitions." Journal of Adhesion Science and Technology **25**(20): 2789-2809.

Kietzig, A. M., S. G. Hatzikiriakos and P. Englezos (2010). "Physics of ice friction." Journal of Applied Physics **107**(8): 81101-81116.

Knapp, H. F. and A. Stemmer (1999). Preparation, comparison and performance of hydrophobic AFM tips. Proceedings of the 3rd Conference on Development and Industrial Application of Scanning Probe Methods (SXM-3), 16-19 Sept. 1998, UK, Wiley.

Kohonen, M. M., N. Maeda and H. K. Christenson (1999). "Kinetics of Capillary Condensation in a Nanoscale Pore." Physical Review Letters **82**(23): 4667.

König, J., S. Nolte and A. Tünnermann (2005). "Plasma evolution during metal ablation with ultrashort laser pulses." Opt. Express **13**(26): 10597-10607.

Krotil, H.-U., T. Stifter, H. Waschipky, K. Weishaupt, S. Hild and O. Marti (1999). "Pulsed force mode: a new method for the investigation of surface properties." Surface and Interface Analysis **27**(5-6): 336-340.

Kruse, C., T. Anderson, C. Wilson, C. Zuhlke, D. Alexander, G. Gogos and S. Ndao (2013). "Extraordinary Shifts of the Leidenfrost Temperature from Multiscale Micro/Nanostructured Surfaces." Langmuir **29**(31): 9798-9806.

Laitinen, O., K. Bauer, J. Niinimäki and U. A. Peuker (2013). "Validity of the Rumpf and the Rabinovich adhesion force models for alumina substrates with nanoscale roughness." Powder Technology **246**(0): 545-552.

Langmuir, I. (1918). "The Evaporation of Small Spheres." Physical Review **12**(5): 368.

Larson, I., C. J. Drummond, D. Y. C. Chan and F. Grieser (1993). "Direct force measurements between titanium dioxide surfaces." Journal of the American Chemical Society **115**(25): 11885-11890.

Le Drogoff, B., F. Vidal, S. Laville, M. Chaker, T. Johnston, O. Barthelemy, J. Margot and M. Sabsabi (2005). "Laser-ablated volume and depth as a function of pulse duration in aluminum targets." Applied Optics **44**(2): 278-281.

Le Harzic, R., D. Breitling, M. Weikert, S. Sommer, C. Fohl, S. Valette, C. Donnet, E. Audouard and F. Dausinger (2005). "Pulse width and energy influence on laser micromachining of metals in a range of 100 fs to 5 ps." Applied Surface Science **249**(1-4): 322-331.

Le Harzic, R., N. Huot, E. Audouard, C. Jonin, P. Laporte, S. Valette, A. Fraczkiewicz and R. Fortunier (2002). "Comparison of heat-affected zones due to nanosecond and femtosecond laser pulses using transmission electronic microscopy." Applied Physics Letters **80**(21): 3886-3888.

Least, B. T. and D. A. Willis (2013). "Modification of polyimide wetting properties by laser ablated conical microstructures." Applied Surface Science **273**: 1-11.

Lee, H. and B. Bhushan (2011). "Role of surface roughness and lubricant film thickness in nanolubrication of sliding components in adaptive optics." Journal of Colloid and Interface Science **353**(2): 574-581.

Lee, M. H., J. Y. Lin and T. W. Odom (2010). "Large-area nanocontact printing with metallic nanostencil masks." Angewandte Chemie - International Edition **49**(17): 3057-3060.

Lehr, J., F. de Marchi, L. Matus, J. MacLeod, F. Rosei and A.-M. Kietzig (2014). "The influence of the gas environment on morphology and chemical composition of surfaces micro-machined with a femtosecond laser." Applied Surface Science **320**(0): 455-465.

Lehr, J. and A.-M. Kietzig (2014). "Production of homogenous micro-structures by femtosecond laser micro-machining." Optics and Lasers in Engineering **57**(0): 121-129.

Leitz, K.-H., B. Redlingshöfer, Y. Reg, A. Otto and M. Schmidt (2011). "Metal Ablation with Short and Ultrashort Laser Pulses." Physics Procedia **12, Part B**(0): 230-238.

Liang, C., H. Wang, J. Yang, Y. Yang and X. Yang (2008). "Surface modification of cp-Ti using femtosecond laser micromachining and the deposition of Ca/P layer." Materials Letters **62**(23): 3783-3786.

Lima, M. S. F., F. Folio and S. Mischler (2005). "Microstructure and surface properties of laser-remelted titanium nitride coatings on titanium." Surface and Coatings Technology **199**(1): 83-91.

Liu, J. M. (1982). "Simple technique for measurements of pulsed Gaussian-beam spot sizes." Opt. Lett. **7**(5): 196-198.

Liu, P. L., R. Yen, N. Bloembergen and R. T. Hodgson (1979). "Picosecond laser-induced melting and resolidification morphology on Si." Applied Physics Letters **34**(12): 864-866.

Liu, X., D. Du and G. Mourou (1997). "Laser ablation and micromachining with ultrashort laser pulses." IEEE Journal of Quantum Electronics **33**(10): 1706-1716.

Lopez, J., R. Torres, Y. Zaouter, P. Georges, M. Hanna, E. Mottay and R. Kling (2013). Study on the influence of repetition rate and pulse duration on ablation efficiency using a new generation of high power ytterbium doped fiber ultrafast laser. Frontiers in Ultrafast Optics: Biomedical, Scientific, and Industrial Applications XIII, February 3, 2013 - February 5, 2013, San Francisco, CA, United states, SPIE.

Lorazo, P., L. J. Lewis and M. Meunier (2006). "Thermodynamic pathways to melting, ablation, and solidification in absorbing solids under pulsed laser irradiation." Physical Review B **73**(13): 134108.

Luft, A., U. Franz, A. Emsermann and J. Kaspar (1996). "A study of thermal and mechanical effects on materials induced by pulsed laser drilling." Applied Physics A (Materials Science Processing) **63**(2): 93-101.

Luo, B. H., P. W. Shum, Z. F. Zhou and K. Y. Li (2010). "Preparation of hydrophobic surface on steel by patterning using laser ablation process." Surface and Coatings Technology **204**(8): 1180-1185.

Luo, L., C. Li, D. Wang, H. Yang, H. Jiang and Q. Gong (2002). "Pulse-parameter dependence of the configuration characteristics of a micro-structure in fused SiO2 induced by femtosecond laser pulses." Applied Physics A (Materials Science Processing) **A74**(4): 497-501.

Maeda, N. and J. N. Israelachvili (2002). "Nanoscale mechanisms of evaporation, condensation and nucleation in confined geometries." Journal of Physical Chemistry B **106**(14): 3534-3537.

Malotky, D. L. and M. K. Chaudhury (2001). "Investigation of capillary forces using atomic force microscopy." Langmuir **17**(25): 7823-7829.

Mandelbrot, B. B. (1983). The fractal geometry of nature. New York, W.H.Freeman and Company.

Mannion, P., J. Magee, E. Coyne and G. M. O'Connor (2003). Ablation thresholds in ultrafast laser micromachining of common metals in air. Opto-Ireland 2002: Optice and Photonics Technologies and Applications, Dublin, SPIE.

Mannion, P. T., J. Magee, E. Coyne, G. M. O'Connor and T. J. Glynn (2004). "The effect of damage accumulation behaviour on ablation thresholds and damage morphology in ultrafast laser micro-machining of common metals in air." Applied Surface Science **233**(1-4): 275-287.

Mao, X. L., W. T. Chan, M. A. Shannon and R. E. Russo (1993). "Plasma shielding during picosecond laser sampling of solid materials by ablation in He versus Ar atmosphere." Journal of Applied Physics **74**(8): 4915-4922.

Marble, F. E. (1963). Dynamics of a gas containing small solid particles. Combustion and Propulsion (5th AGARDograph Colloquium). New York, Pergamon Press**:** pp. 175-213.

Margetic, V., T. Ban, F. Leis, K. Niemax and R. Hergenröder (2003). "Hydrodynamic expansion of a femtosecond laser produced plasma." Spectrochimica Acta Part B: Atomic Spectroscopy **58**(3): 415-425.

Marmur, A. (1992). "Contact angle equilibrium: the intrinsic contact angle." Journal of Adhesion Science and Technology **6**(6): 689-701.

Marmur, A. (2004). "The lotus effect: superhydrophobicity and metastability." Langmuir **20**(9): 3517-3519.

Marmur, A. (2009). "Solid-Surface Characterization b yWetting." Annual Review of Materials Research: 473-490.

Marshall, W. J. (2010). "Two methods for measuring laser beam diameter." Journal of Laser Applications **22**(4): 132-136.

Martirosyan, A. E., C. Altucci, A. Bruno, C. De Lisio, A. Porzio and S. Solimeno (2004). "Time evolution of plasma afterglow produced by femtosecond laser pulses." Journal of Applied Physics **96**(10): 5450-5455.

Martsinovskii, G. A., G. D. Shandybina, D. S. Smirnov, S. V. Zabotnov, L. A. Golovan, V. Y. Timoshenko and P. K. Kashkarov (2008). "Ultrashort excitations of surface polaritons and waveguide modes in semiconductors." Optics and Spectroscopy (English translation of Optika i Spektroskopiya) **105**(1): 67-72.

Masheder, B., C. Urata, D. F. Cheng and A. Hozumi (2014). "Hard coating for polymer substrates through lamination and peeling of porous anodized zirconia." Journal of Nanoscience and Nanotechnology **14**(4): 3006-3010.

Matschegewski, C., S. Staehlke, R. Loeffler, R. Lange, F. Chai, D. P. Kern, U. Beck and B. J. Nebe (2010). "Cell architecture–cell function dependencies on titanium arrays with regular geometry." Biomaterials **31**(22): 5729-5740.

McHale, G. (2007). "Cassie and Wenzel: Were They Really So Wrong?" Langmuir **23**(15): 8200-8205.

Mendonca, C. R., L. R. Cerami, T. Shih, R. W. Tilghman, T. Baldacchini and E. Mazur (2008). "Femtosecond laser waveguide micromachining of PMMA films with azoaromatic chromophores." Optics Express **16**(1): 200-206.

Mengqi, Y. and C. P. Grigoropoulos (2001). "Time-of-flight and emission spectroscopy study of femtosecond laser ablation of titanium." Journal of Applied Physics **89**(9): 5183-5190.

Meyer, E., R. Luthi, L. Howald, W. Gutmannsbauer, H. Haefke and H. J. Guntherodt (1996). "Friction force microscopy on well defined surfaces." Nanotechnology **7**(4): 340-344.

Mhetre, S., W. Carr and P. Radhakrishnaiah (2010). "On the relationship between ink-jet printing quality of pigment ink and the spreading behavior of ink drops." Journal of the Textile Institute **101**(5): 423-430.

Miles, R. E. H., A. E. Carruthers and J. P. Reid (2011). "Novel optical techniques for measurements of light extinction, scattering and absorption by single aerosol particles." Laser and Photonics Reviews **5**(4): 534-552.

Miloshevsky, A., S. S. Harilal, G. Miloshevsky and A. Hassanein (2014). "Dynamics of plasma expansion and shockwave formation in femtosecond laser-ablated aluminum plumes in argon gas at atmospheric pressures." Physics of Plasmas (1994-present) **21**(4): 043111.

Miotello, A. and R. Kelly (1999). "Laser-induced phase explosion: new physical problems when a condensed phase approaches the thermodynamic critical temperature." Applied Physics A **69**(1): S67-S73.

Mittal, J. and G. Hummer (2010). "Interfacial thermodynamics of confined water near molecularly rough surfaces." Faraday Discussions **146**(0): 341-352.

Mittal, K. L. (2008). Contact Angle, Wettability and Adhesion, Volume 5. Leiden, Netherlands, VSP - An imprint of BRILL.

Moore, N. W. (2011). "Adhesion hysteresis from interdependent capillary and electrostatic forces." Langmuir **27**(7): 3678-3684.

Morales, B. A., O. Novaro, T. López, E. Sánchez and R. Gómez (1995). "Effect of hydrolysis catalyst on the Ti deficiency and crystallite size of sol-gel-TiO2 crystalline phases." Journal of Materials Research **10**(11): 2788-2796.

MSE_Handbook (1994). CRC Materials Science and Engineering Handbook. Boca Raton, CRS Press.

Nayak, B. K., M. C. Gupta and K. W. Kolasinski (2008). "Formation of nano-textured conical microstructures in titanium metal surface by femtosecond laser irradiation." Applied Physics A: Materials Science & Processing **90**(3): 399-402.

Nedialkov, N. N., P. A. Atanasov, S. Amoruso, R. Bruzzese and X. Wang (2007). "Laser ablation of metals by femtosecond pulses: theoretical and experimental study." Applied Surface Science **253**(19): 7761-7766.

Nelson, J. S., B. W. Dodson and P. A. Taylor (1992). "Adhesive avalanche in covalently bonded materials." Physical Review B **45**(8): 4439.

Ngoi, B. K. A., K. Venkatakrishnan, E. N. L. Lim, B. Tan and L. H. K. Koh (2001). "Effect of energy above laser-induced damage thresholds in the micromachining of silicon by femtosecond pulse laser." Optics and Lasers in Engineering **35**(6): 361-369.

Nguyen, A. V., J. Nalaskowski, J. D. Miller and H.-J. Butt (2003). "Attraction between hydrophobic surfaces studied by atomic force microscopy." International Journal of Mineral Processing **72**(1-4): 215-225.

Nicholls, R. W. and H. I. S. Ferguson (1964). "Laboratory astrophysics and space science." Canadian Aeronautics and Space Journal **10**(6): 163-168.

Niyomsoan, S., W. Grant, D. L. Olson and B. Mishra (2002). "Variation of color in titanium and zirconium nitride decorative thin films." Thin Solid Films **415**(1–2): 187-194.

Nolte, S., C. Momma, H. Jacobs, A. Tünnermann, B. N. Chichkov, B. Wellegehausen and H. Welling (1997). "Ablation of metals by ultrashort laser pulses." J. Opt. Soc. Am. B **14**(10): 2716-2722.

Nosonovsky, M. and B. Bhushan (2011). Capillary Adhesion and Nanoscale Properties of Water. Scanning Probe Microscopy in Nanoscience and Nanotechnology 2. B. Bhushan. Heidelberg, Springer Berlin Heidelberg**:** 551-571.

Noy, A., C. D. Frisbie, L. F. Rozsnyai, M. S. Wrighton and C. M. Lieber (1995). "Chemical Force Microscopy: Exploiting Chemically-Modified Tips To Quantify Adhesion, Friction, and

Functional Group Distributions in Molecular Assemblies." Journal of the American Chemical Society **117**(30): 7943-7951.

O'Shea, S. J., M. A. Lantz and M. E. Welland (1997). AFM at Liquid-Solid Interfaces. Micro/Nanotribology and Its Applications. B. Bhushan, Springer Netherlands. **330:** 101-119.

Okabe, Y., M. Furugori, Y. Tani, U. Akiba and M. Fujihira (2000). "Chemical force microscopy of microcontact-printed self-assembled monolayers by pulsed-force-mode atomic force microscopy." Ultramicroscopy **82**(1–4): 203-212.

Olivares-Navarrete, R., S. L. Hyzy, R. A. Gittens, J. M. Schneider, D. A. Haithcock, P. F. Ullrich, P. J. Slosar, Z. Schwartz and B. D. Boyan (2013). "Rough titanium alloys regulate osteoblast production of angiogenic factors." The spine journal : official journal of the North American Spine Society **13**(11): 1563-1570.

Oliveira, V., S. Ausset and R. Vilar (2009). "Surface micro/nanostructuring of titanium under stationary and non-stationary femtosecond laser irradiation." Applied Surface Science **255**(17): 7556-7560.

Ostendorf, F., C. Schmitz, S. Hirth, A. Kühnle, J. J. Kolodziej and M. Reichling (2008). "How flat is an air-cleaved mica surface?" Nanotechnology **19**(30): 305705-305711.

Oyabu, N., P. Pou, Y. Sugimoto, P. Jelinek, M. Abe, S. Morita, R. Pérez and O. Custance (2006). "Single atomic contact adhesion and dissipation in dynamic force microscopy." Physical Review Letters **96**(10): 106101.

Paatsch, W., W. Kautek and J. Krueger (1999). "Structuring plating of materials with ultrashort laser pulses." Proceedings of the AESF Annual Technical Conference: 349-354.

Paolasini, S. and A. Kietzig (2014). Synchronized videography of plasma plume expansion during femtosecond laser ablation. Laser Applications in Microelectronic and Optoelectronic Manufacturing (LAMOM) XIX, San Francisco, SPIE.

Park, C. I., H. E. Jeong, S. H. Lee, H. S. Cho and K. Y. Suh (2009). "Wetting transition and optimal design for microstructured surfaces with hydrophobic and hydrophilic materials." Journal of Colloid and Interface Science **336**(1): 298-303.

Park, J. W., H. K. Kim, Y. J. Kim, C. H. An and T. Hanawa (2009). "Enhanced osteoconductivity of micro-structured titanium implants (XiVE S CELLplus™) by addition of surface calcium chemistry: a histomorphometric study in the rabbit femur." Clinical oral implants research **20**(7): 684-690.

Paschotta, R. (2008). Encyclopedia of laser physics and technology. Berlin, Wiley-VCH Berlin.

Perrie, W., M. Gill, G. Robinson, P. Fox and W. O'Neill (2004). "Femtosecond laser micro-structuring of aluminium under helium." Applied Surface Science **230**(1-4): 50-59.

Perry, M. D., B. C. Stuart, P. S. Banks, M. D. Feit, V. Yanovsky and A. M. Rubenchik (1999). "Ultrashort-pulse laser machining of dielectric materials." Journal of Applied Physics **85**(9): 6803-6810.

Petkov, P. V., S. S. Dimov, R. M. Minev and D. T. Pham (2008). "Laser milling: Pulse duration effects on surface integrity." Proceedings of the Institution of Mechanical Engineers, Part B: Journal of Engineering Manufacture **222**(1): 35-45.

Preuss, M. and H.-J. Butt (1998). "Measuring the Contact Angle of Individual Colloidal Particles." Journal of Colloid and Interface Science **208**(2): 468-477.

Prieto, P. and R. E. Kirby (1995). "X-ray photoelectron spectroscopy study of the difference between reactively evaporated and direct sputter-deposited TiN films and their oxidation properties." Journal of Vacuum Science & Technology A **13**(6): 2819-2826.

Quon, R., A. Ulman and T. Vanderlick (2000). "Impact of Humidity on Adhesion between Rough Surfaces†." Langmuir **16**(23): 8912-8916.

Rabinovich, Y. I., A. Singh, M. Hahn, S. Brown and B. Moudgil (2011). "Kinetics of liquid annulus formation and capillary forces." Langmuir **27**(22): 13514-13523.

Rae, S. C. (1994). "Spectral blueshifting and spatial defocusing of intense laser pulses in dense gases." Optics Communications **104**(4–6): 330-335.

Restagno, F., L. Bocquet, T. Biben and É. Charlaix (2000). "Thermally activated dynamics of capillary condensation." Journal of Physics: Condensed Matter **12**: A419.

Riedo, E. and E. Gnecco (2004). Thermally activated effects in nanofriction. Selected Papers from TNT2003, Trends in Nanotechnology International Conference, Salamanca, Institute of Physics Publishing.

Riedo, E., F. Levy and H. Brune (2002). "Kinetics of capillary condensation in nanoscopic sliding friction." Physical Review Letters **88**(18): 1855051-1855054.

Riedo, E., I. Pallaci, C. Boragno and H. Brune (2004). "The 2/3 power law dependence of capillary force on normal load in nanoscopic friction." Journal of Physical Chemistry B **108**(17): 5324-5328.

Robinson, G. M. and M. J. Jackson (2006). "Femtosecond laser micromachining of aluminum surfaces under controlled gas atmospheres." Journal of Materials Engineering and Performance **15**(2): 155-160.

Rodríguez, T. R. and R. García (2004). "Compositional mapping of surfaces in atomic force microscopy by excitation of the second normal mode of the microcantilever." Applied Physics Letters **84**: 449.

Romer, G. R. B. E., A. J. Huis in't Veld, J. Meijer and M. Groenendijk (2009). "On the formation of laser induced self-organizing nanostructures." CIRP Annals - Manufacturing Technology **58**(1): 201-204.

Rutland, M. W. and T. J. Senden (1993). "Adsorption of the poly(oxyethylene) nonionic surfactant C12E5 to silica: a study using atomic force microscopy." Langmuir **9**(2): 412-418.

Scherge, M., S. Gorb and S. N. Gorb (2001). Biological micro-and nanotribology: nature's solutions. Heidelberg, Springer Verlag.

Scherge, M., X. Li and J. A. Schaefer (1999). "The effect of water on friction of MEMS." Tribology Letters **6**(3): 215-220.

Schirmer, N. C., C. Kullmann, M. S. Schmid, B. R. Burg, T. Schwamb and D. Poulikakos (2010). "On ejecting colloids against capillarity from sub-micrometer openings: On-demand dielectrophoretic nanoprinting." Advanced Materials **22**(42): 4701-4705.

Schmidt, D. L., C. E. Coburn, B. M. DeKoven, G. E. Potter, G. F. Meyers and D. A. Fischer (1994). "Water-based non-stick hydrophobic coatings." Nature **368**(6466): 39-41.

Schönherr, H., C. L. Feng, N. Tomczak and G. J. Vancso (2005). "Compositional Mapping of Polymer Surfaces by Chemical Force Microscopy Down to the Nanometer Scale: Reactions in Block Copolymer Microdomains." Macromolecular Symposia **230**(1): 149-157.

Scuderi, D., O. Albert, D. Moreau, P. P. Pronko and J. Etchepare (2005). "Interaction of a laser-produced plume with a second time delayed femtosecond pulse." Applied Physics Letters **86**(7): 071502-071503.

Sears, F. W. Z. M. W. (1955). University physics. Reading, Mass., Addison-Wesley Pub. Co.

Sedin, D. L. and K. L. Rowlen (2000). "Adhesion Forces Measured by Atomic Force Microscopy in Humid Air." Analytical Chemistry **72**(10): 2183-2189.

Semmar, N., M. Tebib, J. Tesar, N. N. Puscas and E. Amin-Chalhoub (2009). "Direct observation of phase transitions by time-resolved pyro/reflectometry of KrF laser-irradiated metal oxides and metals." Applied Surface Science **255**(10): 5549-5552.

Shanahan, M. E. R. (1987). "The influence of solid micro-deformation on contact angle equilibrium." Journal of Physics D: Applied Physics **20**(7): 945-950.

Shanahan, M. E. R. (1995). "Simple Theory of "Stick-Slip" Wetting Hysteresis." Langmuir **11**(3): 1041-1043.

Sheehy, M. A., L. Winston, J. E. Carey, C. M. Friend and E. Mazur (2005). "Role of the Background Gas in the Morphology and Optical Properties of Laser-Microstructured Silicon." Chemistry of Materials **17**(14): 3582-3586.

Sheng Chao, C. and L. Jen Fin (2008). The capillary force between an AFM tip and a surface at different humidity. 2nd International Conference on Integration and Commercialization of Micro and Nanosystems 2008, 3-5 June 2008, New York, NY, USA, ASME.

Sherman, N. K., F. Brunel, P. B. Corkum and F. A. Hegmann (1989). "Transient response of metals to ultrashort pulse excitation." Optical Engineering **28**(10): 1114-1121.

Shield, T. W., D. B. Bogy and F. E. Talke (1986). "A numerical comparison of one-dimensional fluid jet models applied to drop-on-demand printing." Journal of Computational Physics **67**(2): 327-347.

Sipe, J., J. F. Young, J. Preston and H. Van Driel (1983). "Laser-induced periodic surface structure. I. Theory." Physical Review B **27**(2): 1141.

Sirghi, L., R. Szoszkiewicz and E. Riedo (2006). "Volume of a nanoscale water bridge." Langmuir **22**(3): 1093-1098.

Smith, D. A., S. D. Connell, C. Robinson and J. Kirkham (2003). "Chemical force microscopy: applications in surface characterisation of natural hydroxyapatite." Analytica Chimica Acta **479**(1): 39-57.

Stifter, T., O. Marti and B. Bhushan (2000). "Theoretical investigation of the distance dependence of capillary and van der Waals forces in scanning force microscopy." Physical Review B **62**(20): 13667-13673.

Stoian, R., D. Ashkenasi, A. Rosenfeld and E. Campbell (2000). "Coulomb explosion in ultrashort pulsed laser ablation of Al 2 O 3." Physical Review B **62**(19): 13167.

Sugimoto, Y., P. Pou, M. Abe, P. Jelinek, R. Perez, S. Morita and O. Custance (2007). "Chemical identification of individual surface atoms by atomic force microscopy." Nature **446**(7131): 64-67.

Sun, J. and J. P. Longtin (2001). "Inert gas beam delivery for ultrafast laser micromachining at ambient pressure." Journal of Applied Physics **89**(12): 8219-8224.

Szoszkiewicz, R., B. Bhushan, B. D. Huey, A. J. Kulik and G. Gremaud (2005). "Correlations between adhesion hysteresis and friction at molecular scales." Journal of Chemical Physics **122**(1): 1-6.

Szoszkiewicz, R. and E. Riedo (2005). "Nanoscopic friction as a probe of local phase transitions." Applied Physics Letters **87**(1): 1-3.

Szoszkiewicz, R. and E. Riedo (2005). "Nucleation time of nanoscale water bridges." Physical Review Letters **95**(1): 1-4.

Tadmor, R. (2004). "Line energy and the relation between advancing, receding, and Young contact angles." Langmuir **20**(18): 7659-7664.

Tadmor, R. (2011). "Approaches in wetting phenomena." Soft Matter **7**(5): 1577-1580.

Tan, B., A. Dalili and K. Venkatakrishnan (2009). "High repetition rate femtosecond laser nano-machining of thin films." Applied Physics A (Materials Science Processing) **95**(2): 537-545.

Tan, B. and K. Venkatakrishnan (2006). "A femtosecond laser-induced periodical surface structure on crystalline silicon." Journal of Micromechanics and Microengineering **16**(5): 1080-1085.

Tang, M., M. H. Hong, Y. S. Choo, Z. Tang and D. H. C. Chua (2010). "Super-hydrophobic transparent surface by femtosecond laser micro-patterned catalyst thin film for carbon nanotube cluster growth." Applied Physics A (Materials Science Processing) **101**(3): 503-508.

Tien, N. C., S. Jeong, L. M. Phinney, K. Fushinobu and J. Bokor (1996). "Surface adhesion reduction in silicon microstructures using femtosecond laser pulses." Applied Physics Letters **68**(2): 197-199.

Tokumoto, H., K. Ide, K. Ukita and H. Azehara (2007). Chemical force AFM with CNT tips. Microprocesses and Nanotechnology 2007. 20th International Microprocesses and Nanotechnology Conference, 5-8 Nov. 2007, Piscataway, NJ, USA, IEEE.

Truong, J. G. and P. C. Wayner, Jr. (1987). "Effects of capillary and van der Waals dispersion forces on the equilibrium profile of a wetting liquid: theory and experiment." Journal of Chemical Physics **87**(7): 4180-4188.

Tsukamoto, M., K. Asuka, H. Nakano, M. Hashida, M. Katto, N. Abe and M. Fujita (2006). "Periodic microstructures produced by femtosecond laser irradiation on titanium plate." Vacuum **80**(11-12): 1346-1350.

Uppal, N. and P. S. Shiakolas (2008). "Micromachining Characteristics of NiTi Based Shape Memory Alloy Using Femtosecond Laser." Journal of Manufacturing Science and Engineering **130**(3): 031117-031117.

Uzhegova, N. I., A. L. Svistkov, B. Lauke and G. Heinrich (2014). "The influence of capillary effect on atomic force microscopy measurements." International Journal of Engineering Science **75**(0): 67-78.

Vadakkan, T. (2009). Multifractal spectrum of a binary image. MATLAB Central, Mathworks.

van der Vegte, E. W. and G. Hadziioannou (1997). "Scanning Force Microscopy with Chemical Specificity: An Extensive Study of Chemically Specific Tip−Surface Interactions and the Chemical Imaging of Surface Functional Groups." Langmuir **13**(16): 4357-4368.

Vatsya, S. R. and S. K. Nikumb (2007). "Geometrical profile of material surface ablated with highpower, short-pulse lasers in ambient gas media." Journal of Physics: Conference Series **59**(1): 704-707.

Venkatakrishnan, K., P. Stanley, N. R. Sivakumar, B. Tan and L. E. N. Lim (2003). "Effect of scanning resolution and fluence fluctuation on femtosecond laser ablation of thin films." Applied Physics A (Materials Science Processing) **A77**(5): 655-658.

Vogel, K. and P. Backlund (1965). "Application of electron and optical microscopy in studying laser-irradiated metal surfaces." Journal of Applied Physics **36**(12): 3697-3701.

Vogler, E. A. (1998). "Structure and reactivity of water at biomaterial surfaces." Advances in Colloid and Interface Science **74**(1–3): 69-117.

Vogt, B. D., C. L. Soles, H.-J. Lee, E. K. Lin and W.-l. Wu (2005). "Moisture absorption into ultrathin hydrophilic polymer films on different substrate surfaces." Polymer **46**(5): 1635-1642.

Vorobyev, A. and C. Guo (2008). "Femtosecond laser blackening of platinum." Journal of applied physics **104**(5): 053516.

Vorobyev, A. Y. and C. Guo (2007). "Effects of nanostructure-covered femtosecond laser-induced periodic surface structures on optical absorptance of metals." Applied Physics A (Materials Science Processing) **86**(3): 321-324.

Vorobyev, A. Y. and C. Guo (2007). "Femtosecond laser structuring of titanium implants." Applied Surface Science **253**(17): 7272-7280.

Vorobyev, A. Y. and C. Guo (2008). "Colorizing metals with femtosecond laser pulses." Applied Physics Letters **92**(4): -.

Vujicic, N., H. Skenderovic, T. Ban, D. Aumiler and G. Pichler (2006). "Low-density plasma channels generated by femtosecond pulses." Applied Physics B (Lasers and Optics) **B82**(3): 377-382.

Wallqvist, V., P. M. Claesson, A. Swerin, C. Ostlund, J. Schoelkopf and P. A. C. Gane (2009). "Influence of surface topography on adhesive and long-range capillary forces between hydrophobic surfaces in water." Langmuir **25**(16): 9197-9207.

Weck, A., T. H. R. Crawford, D. S. Wilkinson, H. K. Haugen and J. S. Preston (2007). "Ripple formation during deep hole drilling in copper with ultrashort laser pulses." Applied Physics A: Materials Science and Processing **89**(4): 1001-1003.

Weisenhorn, A., P. Hansma, T. Albrecht and C. Quate (2009). "Forces in atomic force microscopy in air and water." Applied Physics Letters **54**(26): 2651-2653.

Wellershoff, S. S., J. Hohlfeld, J. Güdde and E. Matthias (1999). "The role of electron–phonon coupling in femtosecond laser damage of metals." Applied Physics A **69**(1): S99-S107.

Wen, S.-B., X. Mao, R. Greif and R. E. Russo (2007). "Expansion of the laser ablation vapor plume into a background gas. I. Analysis." Journal of Applied Physics **101**(2): 023114-023113.

Wen, S.-B., X. Mao, R. Greif and R. E. Russo (2007). "Laser ablation induced vapor plume expansion into a background gas. II. Experimental analysis." Journal of Applied Physics **101**(2): 023115-023114.

Wenzel, R. N. (1936). "Resistance of solid surfaces to wetting by water." Industrial & Engineering Chemistry **28**(8): 988-994.

Whyman, G., E. Bormashenko and T. Stein (2008). "The rigorous derivation of Young, Cassie-Baxter and Wenzel equations and the analysis of the contact angle hysteresis phenomenon." Chemical Physics Letters **450**(4-6): 355-359.

Wu, A. H. F., K. L. Cho, I. I. Liaw, G. Moran, N. Kirby and R. N. Lamb (2010). "Hierarchical surfaces: an in situ investigation into nano and micro scale wettability." Faraday Discussions **146**(0): 223-232.

Wypych, G. (2000). Physical Properties of Fillers and Filled Materials. Handbook of Fillers - A Definitive User's Guide and Databook (2nd Edition). G. Wypych. New York, N.Y., ChemTec Publishing**:** 241-302.

Xu, L., T. Junfei, G. Garnier and S. Wei (2010). "Fabrication of paper-based microfluidic sensors by printing." Colloids and Surfaces B: Biointerfaces **76**(2): 564-570.

Xudong, X. and Q. Linmao (2000). "Investigation of humidity-dependent capillary force." Langmuir **16**(21): 8153-8158.

Yahng, J. S., J. R. Nam and S. C. Jeoung (2009). "The influence of substrate temperature on femtosecond laser micro-processing of silicon, stainless steel and glass." Optics and Lasers in Engineering **47**(7-8): 815-820.

Yahyapour, N., C. Eriksson, P. Malmberg and H. Nygren (2004). "Thrombin, kallikrein and complement C5b-9 adsorption on hydrophilic and hydrophobic titanium and glass after short time exposure to whole blood." Biomaterials **25**(16): 3171-3176.

Yamaguchi, S., A. Ueno, Y. Akiyama and K. Morishima (2012). "Cell patterning through inkjet printing of one cell per droplet." Biofabrication **4**(4): 45005-45013.

Yamazaki, K., T. Yakushiji and K. Sakai (2012). "Nanoscale analysis of hydrophilicity-hydrophobicity distribution on inner surfaces of wet dialysis membranes by atomic force microscopy." Journal of Membrane Science **396**: 38-42.

Yang, J., Y. Zhao and X. Zhu (2007). "Theoretical studies of ultrafast ablation of metal targets dominated by phase explosion." Applied Physics A (Materials Science Processing) **89**(2): 571-578.

Yang, Y., J. Yang, C. Liang, H. Wang, X. Zhu and N. Zhang (2009). "Surface microstructuring of Ti plates by femtosecond lasers in liquid ambiences: a new approach to improving biocompatibility." Opt Express **17**(23): 21124-21133.

Yao, C., B. Xu, J. Huang, P. Zhang and Y. Wu (2010). "Study on the softening in overlapping zone by laser-overlapping scanning surface hardening for carbon and alloyed steel." Optics and Lasers in Engineering **48**(1): 20-26.

Yong, J., F. Chen, Q. Yang, D. Zhang, G. Du, J. Si, F. Yun and X. Hou (2013). "Femtosecond laser weaving superhydrophobic patterned PDMS surfaces with tunable adhesion." Journal of Physical Chemistry C **117**(47): 24907-24912.

Yoon, E.-S., S. H. Yang, H.-G. Han and H. Kong (2003). "An experimental study on the adhesion at a nano-contact." Wear **254**(10): 974-980.

Young, J. F., J. Preston, H. Van Driel and J. Sipe (1983). "Laser-induced periodic surface structure. II. Experiments on Ge, Si, Al, and brass." Physical Review B **27**(2): 1155.

Young, T. (1805). "An Essay on the Cohesion of Fluids." Philosophical Transactions of the Royal Society of London **95**: 65-87.

Zhang, H., R. N. Lamb and D. J. Cookson (2007). "Nanowetting of rough superhydrophobic surfaces." Applied Physics Letters **91**(25): 254106-254109.

Zhang, Y., O. Andrukhov, S. Berner, M. Matejka, M. Wieland, X. Rausch-Fan and A. Schedle (2010). "Osteogenic properties of hydrophilic and hydrophobic titanium surfaces evaluated with osteoblast-like cells (MG63) in coculture with human umbilical vein endothelial cells (HUVEC)." Dental Materials **26**(11): 1043-1051.

Zhao, J. X., B. Huttner and A. Menschig (1999). Micromachining with ultrashort laser pulses. Laser Applications in Microelectronic and Optoelectronic Manufacturing IV, 25-27 Jan. 1999, San Francisco, SPIE-Int. Soc. Opt. Eng.

Zhao, Y., S. M. Wong, H. M. Wong, H. Pan, K. W. K. Yeung and P. K. Chu (2013). "Improved in vitro and in vivo biocompatibility of dual plasma modified titanium alloy." Surface and Coatings Technology **229**(0): 130-134.

Zhigilei, L. V. (2003). "Dynamics of the plume formation and parameters of the ejected clusters in short-pulse laser ablation." Applied Physics A (Materials Science Processing) **76**(3): 339-350.

Zuhlke, C. A., T. P. Anderson and D. R. Alexander (2013). "Formation of multiscale surface structures on nickel via above surface growth and below surface growth mechanisms using femtosecond laser pulses." Optics Express **21**(7): 8460-8473.

Zuhlke, C. A., T. P. Anderson and D. R. Alexander (2013). "Fundamentals of layered nanoparticle covered pyramidal structures formed on nickel during femtosecond laser surface interactions." Applied Surface Science **283**(0): 648-653.